Dynamic Subsidence, Continental Uplift and Sedimentary Deposition to West Africa's Passive Margin

Bhavik Harish Lodhia

A thesis submitted for the degree of
Doctor of Philosophy
Imperial College London

Department of Earth Science & Engineering
February 2019

Declaration

Declaration of originality

This thesis describes my original work except where acknowledgement is made in the text. It does not exceed the word limit and is not substantially the same as any work that has been, or is being submitted to any other university for any degree, diploma or any other qualification.

Bhavik Harish Lodhia
February 2019

Copyright declaration

The copyright of this thesis rests with the author and is made available under a Creative Commons Attribution Non-Commercial No Derivatives licence. Researchers are free to copy, distribute or transmit the thesis on the condition that they attribute it, that they do not use it for commercial purposes and that they do not alter, transform or build upon it. For any reuse or redistribution, researchers must make clear to others the licence terms of this work

Acknowledgements

The decision to pursue a PhD was made at a moment's notice. First and foremost, I thank my supervisors Dr Gareth G. Roberts and Professor Alastair J. Fraser for their support and guidance throughout this PhD. My mother, who taught me how to read and who took me to London's Natural History Museum every year without fail as a child, is responsible for my dream to become a geoscientist. Her never ending supply of dahl bhat and shak rotli undoubtedly helped me to power through this PhD. I thank my entire family for their invaluable contribution and support over the last four years and for ensuring that I reach this point. I thank my father, Harish, and brother, Jatin, for ensuring that I stayed focussed.

The completion of this PhD would not have been possible without the help and support of Tullow Oil Plc., who provided unrestricted access to confidential, industry-owned data that underpins this study, office space in their London headquarters and technichal support throughout the duration of my PhD. In particular, Dr Jerry Jarvis, Robbie Cowan and Richard Newton are thanked for discussions and their efforts in securing access and permission to publish data used in this study from their industry parters. A special mention must also go to Clyde Coleman, who never stopped smiling whenever I required rescuing from IT problems throughout my time working at Tullow Oil Plc. The NERC Centre for Doctoral Training in Oil & Gas is thanked for their invluable support in funding my PhD, and the thoroughly enjoyable experience of being part of a cohort of great people.

Finally, I thank Dr Gaia Stucky De Quay and Victoria Fernandes for their sense of humour and banter whilst working besides me, and thank everyone else who made the last four years the most enjoyable of my life so far. Onwards and upwards!

Abstract

The relationship between offshore subsidence, continental uplift and sedimentary deposition to passive margins is poorly understood. A history of dynamic subsidence, continental uplift and sedimentary deposition to West Africa's passive margin was synthesised to produce a framework for predicting patterns of sedimentary flux to the Mauritanian basin. Stratigraphy was mapped using seismic/well data and Cretaceous–Recent sedimentary flux was calculated. Clastic sedimentary flux to the centre of the basin increased significantly during Neogene times and accelerated across the basin at ~ 5 Ma. The origins of the Mauritanian basin were explored by backstripping wells from the study area to calculate subsidence histories. Seismic, well, gravity, magmatic and tomographic information was used to show that < 0.8 km of rapid Neogene–Recent subsidence occurred due to the initiation of shallow mantle convection. Neogene–Recent mantle draw-down caused the creation of accommodation within the Mauritanian basin that was subsequently filled by clastic sediments delivered by rivers draining West Africa's passive margin. The causes of increased Neogene–Recent sedimentary flux were explored by inverting 14700 African longitudinal river profiles using a calibrated stream–power model to calculate a history of continental uplift and to predict the pattern of sedimentary flux to the Mauritanian basin. Results are consistent with independent stratigraphic observations which indicate that from ~ 30 Ma–Recent, sedimentary flux to Africa's major deltas increased and induced a change from dominantly carbonate to clastic deposition. This pattern of sedimentary flux is consistent with calculations of offshore sedimentary volumes made using seismic and well data. I suggest Neogene clastic flux to the Mauritanian margin was generated by denudation of the uplifting Fouta-Djallon topographic swell and Mauritinides fold-belt, which appears to have accelerated during the last ~ 5 Ma. Results suggest that mantle-driven convective continental uplift exerts an important control on the sedimentary budget to Africa's passive margins.

Research output

The work of this thesis is based on the following publications:

- **Lodhia, B.H.**, Roberts, G.G., Fraser, A.J., Goes, S., Fishwick, S., Jarvis, J., 2018. Continental margin subsidence form shallow mantle convection: Example from West Africa, Earth Planet. Sci. Let., 481, 350–361, doi:10.1016/j.epsl.2017.10.024.
- Roberts, G.G., White, N., **Lodhia, B.H.**, 2019. The generation and scaling of longitudinal river profiles. Journal of Geophysical Research: Earth Surface, 124. https://doi.org/10.1029/2018JF004796.
- **Lodhia, B.H.**, Roberts, G.G., Fraser, A.J., Jarvis, J., Cowan, R., Newton, R. Observation and simulation of solid sedimentary flux with African examples (*submitted*). This manuscript has been submitted to a leading scientific journal and is under review at the time of submission of this thesis.

Contents

1 Introduction **17**
1.1 Motivation of study 17
1.2 Thesis structure 32

2 Stratigraphy and sedimentary flux history of the Mauritanian basin **35**
2.1 Northwest Africa 35
2.2 Data 39
2.2.1 Well data 39
2.2.2 Seismic & check-shot data 45
2.3 Methodology to calculate solid sedimentary flux 46
2.4 Ages of acoustic basement and salt 50
2.5 Solid sedimentary flux of the Mauritanian basin 51
2.5.1 5.6 – 23.8 Ma 54
2.6 Distribution of sedimentary rock in the Mauritanian basin 56
2.7 Conclusions 56
2.8 Prelude to next chapter 61

3 Shallow mantle convection beneath the Mauritanian basin 63
3.1 Introduction 63
3.2 Data Processing and Methodology 65
3.2.1 Shear wave velocities 65
3.2.2 Tomography model 66
3.2.3 Temperature from shear wave velocities 70
3.2.4 Temperature from shear wave velocities and isostasy . . 73
3.2.5 Ocean age-depth residuals 73
3.3 Subsidence history 75
3.3.1 Extrapolations of seismic horizons 75
3.3.2 Backstripping for subsidence histories 75
3.3.3 Theoretical thermal subsidence 77
3.4 Results 77
3.4.1 Tomography 77
3.4.2 Temperature from shear wave velocities 78
3.4.3 Ocean age-depth 78

3.4.4 Stratigraphy and subsidence . . . 79
3.5 Discussion . . . 81
3.6 Conclusion . . . 85
3.7 Prelude to next chapter . . . 86

4 African uplift and sedimentary flux from continental drainage inversion 89
4.1 Introduction . . . 89
4.2 Data & Methodology . . . 91
4.2.1 Continental drainage and dynamic topography . . . 91
4.2.2 Uplift as a function of time and space . . . 91
4.3 Independent geological constraints for African uplift . . . 105
4.3.1 Southern Africa . . . 106
4.3.2 Western Africa . . . 110
4.3.3 North Africa . . . 112
4.3.4 East Africa . . . 114
4.4 Results . . . 114
4.5 Discussion . . . 123
4.6 Conclusion . . . 130

5 Future work & conclusions 133
5.1 Summary . . . 133
5.2 Implications of results & future work . . . 136
5.2.1 How far back can we go? . . . 136
5.2.2 Implications for industry . . . 137
5.2.3 Localised studies & environmental applications . . . 138
5.3 Conclusions . . . 140

6 Appendices 143
6.1 Appendix 1 . . . 143
6.1.1 Generating continuous surfaces . . . 143
6.1.2 Depth conversion and sediment thickness calculation . . . 145

List of Figures

1 Global continental topography and offshore sediment thickness . 24
2 Major African rivers, continental topography, offshore sediment thickness, residual and dynamic topography 31

3 African topography, drainage and sedimentary rock offshore . . . 37
4 Mauritanian margin and surroundings 38
5 Mauritanian stratigraphy 42
6 Seismic data 43
7 Seismic data 44
8 Check shot data for Mauritanian wells 45
9 Compaction parametrisation 49
10 Mauritanian chrono- and biostratigraphy 58
11 Solid sedimentary thickness of the Mauritanian basin 60
12 Mauritanian sedimentary flux 60

13 Bathymetry and residual topography of West African margin . . 66
14 Shear wave tomography model 68
15 Path coverage & checkerboard tests 69
16 Shear wave tomography to temperature conversion 74
17 Age–depth curves of Mauritanian wells 76
18 Water-loaded subsidence results of Mauritanian wells 80
19 Flexure due to Cape Verde crustal load 82
20 Summary of results along cross-section X—X′ 84
21 Cartoon summarising results 86

22 Sub-plate support and drainage patterns of Africa and the Mauritanian margin 92
23 Continental drainage extreacted from SRTM DEM 93
24 Longitudinal river profiles of major African drainage systems . . 94
25 Distribution of vertices in inverse model for African rivers 102
26 Distribution of vertices in inverse model for Mauritania & Senegal 103
27 Model regularisation 105
28 Independent constraints of continental uplift 116
29 Inverse modelling of African river profiles arranged by catchment. 118
30 Cumulative African uplift from 30 Ma to Recent 119
31 Cumulative uplift histories for Mauritania & Senegal from 30 Ma to Recent 120

32 Observed versus calculated uplift rates for Africa 121
33 Prediction of Neogene sedimentary flux from drainage inversion 122
34 Sedimentary flux to Africa's passive continental margins 131

35 Seismic horizons mapped in two-way time 144
36 Depth converted seismic horizons 146
37 Uncorrected sediment thickness 148

List of Tables

1 Summary of wells used in this study 40
2 Biostratigraphy of seismic horizons identified at wells in this study 41
3 Solid sedimentary flux of the Mauritanian basin 56
4 Observed African uplift used to calibrate stream power erosional model 116

Chapter 1

Introduction

1.1 Motivation of study

The 'source to sink' problem

Balancing the amount of rock produced from sedimentary 'sources' (e.g. erosion of continental topography) with that deposited in sedimentary 'sinks' (e.g. offshore basins) is known as the 'source to sink' problem. To evaluate the link between sedimentary 'sources' and 'sinks' for a continental source–offshore basin system, two processes must be considered. Firstly, what processes onshore are responsible for controlling continental erosion and depositing clastic sediments offshore? Secondly, what processes are responsible for creating accommodation required to capture sediments delivered to passive margin basins?

Onshore continental erosion is undoubtedly complex and is controlled by a vast range of processes. Traditional 'source' to 'sink' studies usually focus on relating one or more of three main quantifiable measures to erosion rate and use various modelling approaches to balance sediment flux calculations with offshore observations. These quantifiable measures include lithology, relief and climate. The relative importance of these measures is a matter of intense debate and centres around the spatial and temporal scales of the problems being tackled. At long wavelengths and geological timescales, lithology tends to be averaged over a wide region, thus diminishing its relative importance (Allen, 1997; Hay, 1998; Hay et al., 2002; Macgregor, 2012; Chardon et al., 2016; Grimaud et al., 2018). Many of the world's greatest rivers which are ultimately responsible for transporting continental clastic material to major offshore sedimentary

basin systems extend across multiple climatic bands, lithological boundaries and topographic ranges. In the case of Africa, many of the continent's largest rivers and associated drainage systems have remained stable for substantially long periods of time ($\sim$ 30 Ma, e.g. Macgregor, 2012; Chardon et al., 2016; Grimaud et al., 2018). Recent successes in fitting substantial inventories river profiles by smoothly varying regional uplift rate and using a simple advective model of erosion rate (stream-power) suggests that long wavelength processes play a significant role in forcing and configuring landscapes that deliver sediments to the offshore realm (e.g. Pritchard et al., 2009; Roberts and White, 2010; Roberts et al., 2012a,b; Paul et al., 2014; Stephenson et al., 2014; Rudge et al., 2015; Roberts et al., 2019). Spectral analyses of Africa's largest rivers by Roberts et al. (2019) shows that more than $> 90\%$ of spectral power resides at wavelengths > 100 km and that spectra exhibit self-similar behaviour at long wavelengths. At wavelengths $\sim< 100$ km, a crossover transition from red to pink noise appears, suggesting that at shorter wavelengths the effects of different noise (such as climate and lithology that vary on shorter wavelengths) become evident. This observation suggests that long wavelength processes responsible for controlling the evolution of continental-scale drainage networks may ultimately control the supply of clastic sediment delivered by these networks to offshore sedimentary basins.

Other recent studies linking sediment 'sources' and 'sinks' focus on attempting to balance volumes of sedimentary rock deposited in offshore basins with those produced as a result of onshore denudation, and matching the timing of increased offshore sedimentary flux with periods of increased onshore denudation. For example, Tinker et al. (2008) use apatite fission-track thermochronology to link the timing of periods of increased denudation onshore the Southern Cape, South Africa to periods of increased sedimentary flux to the Outeniqua and Southern Outeniqua Basins of South Africa by calculating their Cretaceous–Recent sediment flux histories using seismic and well data. Although Tinker et al. (2008) are unable to balance sediment volumes calculated as a result of denudation to isopach volumes calculated offshore, they do show that the timings of increased sediment accumulation and increased onshore denudation from Cretaceous–Recent times closely match. Grimaud et al. (2018)

quantify patterns of Cenozoic denudation and catchment export using dated and regionally correlated relict lateritic landforms of Sub-Saharan West Africa. In the non-orogenic domain of West Africa, Grimaud et al. (2018) find that whilst overall denudation rates are low, denudation may increase significantly with rock uplift driven by mantle uplift or lithosphere deformation and flexure. Pechlivanidou et al. (2018) account for dynamic channel adjustment by calibrating Howard et al. (1994)'s stream-power erodability model using field data to make a first-order estimate of the volume of sediment produced from the erosion of upland areas in the Sperichos rift basin, central Greece. They show that for a closed system during Holocene times, the mass of sedimentary rock produced due to erosion onshore is balanced with that deposited in the basin.

In the offshore realm, continental passive margin basins preserve a record of sedimentary flux over timescales of millions to tens of millions of years, whereby terriginous sedimentary rock produced from onshore erosion may reach thicknesses of > 10 km of (e.g. Dingle, 1983; Rust and Summerfield, 1990; DuToit et al., 1997; Aal et al., 2000; Hall et al., 2005; Walford et al., 2005; Rouby et al., 2009; Paul et al., 2014; Grimaud et al., 2018, Figure 1). The predominant source of terriginous clastic sediments deposited to the offshore realm is the erosion and denudation of continental hinterland, whose primary conduits for transport to offshore sedimentary basins are continental river channels and their tributaries. At present, the Yellow, Ganges and Bramaputra river systems deliver the highest global average annual sediment yields of between 2.08-0.8×10^6 t a^{-1}. In comparison, the Congo, Nile and Niger river systems deliver 1.55-0.43×10^6 t a^{-1} to their deltas (Holeman, 1968). Long-term (1–10 Ma) clastic sedimentary fluxes to depositional basins provide first-order constraints on the response of continental surfaces to tectonic forcing (e.g. Ebinger et al., 1993; Leeder, 1993; Hardy and Gawthorpe, 2002; Grimaud et al., 2018). Hence, the distribution of sediments and pattern of solid sedimentary flux to continental margin basins may be used to provide clues about processes that control the evolution of continental surfaces.

It is clear that both onshore and offshore processes must be considered when tackling the 'source to sink' problem. Recent studies have succeeded in

correlating the timing of continental denudation with offshore clastic sediment deposition and balancing the amount of sediment produced onshore with that deposited offshore (e.g. Gallagher and Brown, 1999; Syvitski et al., 2003; Van Rompaey et al., 2005; Tinker et al., 2008; Romans et al., 2009; Covault et al., 2011; Grimaud et al., 2018; Pechlivanidou et al., 2018). However, a quantitative link between the processes responsible for uplift and erosion of continental hinterland and those responsible for creating the accommodation necessary to capture sedimentary rock in 'source to sink' systems remains elusive. Hence, to tackle the 'source to sink' problem, the processes responsible for basin subsidence, continental uplift, erosion and sedimentary deposition to continental passive margins must be brought together.

In this study, I evaluate the history of sediment deposition to the Mauritanian basin on northwest Africa's passive continental margin, and investigate the processes responsible for basin formation and clastic sediment production due to continental uplift from Neogene–Recent times.

Geological history and setting of Northwest Africa

The present day position of Northwest Africa is a result of a complex history of continental collision, breakup and drifting. The exploitation and reactivation of Late Proterozoic Pan-African structures and lineaments that formed between 720–550 Ma is generally considered to be responsible for the majority of subsequent Paleozoic tectonism and magmatism within the African plate (Stern, 1994; Unrug, 1996, 1997). These Pan-African structures are related to the initial formation of Gondwana (and Pangaea) by amalgamation of Archean and Proterozoic cratons, voluminous island arc material as accreted terranes and sub-craton sized fragments of Proterozoic continental material (e.g. Jebel-Uweinat) into a coherent super-continental unit (Bumby and Guiraud, 2005). In northwest Africa, these belts include: the Anti-Atlas, Ougarta, Pharusian–Tuareg, Gourma, and Dahomeyan orogenic belts to the east and the Mauritinide, Bassaride and Rokelide belts to the west (Hefferan et al., 2000). The dominant cratonic unit in northwest Africa is the West African Craton (WAC), which is largely surrounded by Pan-African mobile belts that appear to have developed as a result of successive collisions of magmatic arcs, accretionary

melanges and/or previously amalgamated terranes with rifted margins of the WAC (e.g. Saquaque et al., 1989; Black et al., 1994; Thomas et al., 2004; Bumby and Guiraud, 2005).

The drift history of Gondwana (and northwest Africa) during the Paleozoic is a matter of intense debate in the scientific community. Comparisons of palaeopoles and published palaeogeographic models based on palaeoclimatic and biogeographic data show that northwest Africa migrated from polar to sub-tropical latitudes from Late Ordavician–Early Silurian times and southwards towards intermediate ($\sim 50°$) latitudes during the Late Silurian–Early Devonian (Van der voo, 1988). Using the existing palaeomagnetic database alone, two contrasting models for Paleozoic apparent polar wander (APW) paths of Gondwana have been proposed. These models indicate either gradual northward movement of Gondwana from Late Ordovician–Early Carboniferous times, or, alternatively, a much more complex path implying collision of northern Africa with Laurussia during Late Silurian–Early Devonian times and then again during Carboniferous times. However, both of these models agree that during Early Ordovician times, the south pole was situated in northwest Africa. During the Late Devonian, APW paths determined by both models are anchored by a small cluster of high-quality palaeopoles in central Africa. By Late Carboniferous–Permian times, the south pole was clearly located in Antarctica (Tait et al., 2000). This history is reflected by the record concomitant changes in paleoclimate recorded by the sedimentary fill of basins preserved across the continent (e.g. Burke et al., 2003; Bumby and Guiraud, 2005).

Rifting of the Central Atlantic margin associated with Gondwana breakup began in the Late Triassic at the same time as adjacent onshore rifts developed (Davison, 2005). Assuming a constant spreading rate in the Jurassic, a Middle Jurassic age was estimated for southern Central Atlantic spreading based on extrapolation from the earliest magnetic anomaly M25 (Klitgord and Schouten, 1986). Since Africa's separation from the Americas following Gondwana breakup, the presence of plumes beneath the African plate during the Mesozoic and Cenozoic coupled with an absence of slab pull at the margins of the young post-Gondwana oceanic crust, has rendered Africa in a relatively stationary latitudinal position since the Mesozoic. During this time, only a slow

rotation of the plate has occurred as the Central and South Atlantic, Indian Ocean and Red Sea have opened (Bumby and Guiraud, 2005).

As the African continent has remained in a relatively stable sub-equatorial latitudinal range since Mesozoic times, the dominant control on sedimentary depositional environments across the northwestern continental margin has been a history of marine transgressions, regressions, tectonic activity and continental uplift. Following Early Jurassic seafloor spreading, the Central Atlantic domain of Africa had long reached its post-rift stage and had built a stable continental shelf on the West African passive margin (Dillon et al., 1988; Davison, 2005). A major Early Cretaceous regression was followed by the drowning of a long-lived regional carbonate platform that extended across the West African continental margin during the Valanginian, which was also covered by prograding deltaic clastics during this time (Davison, 2005). This was followed by a period of shallow marine deposition that dominated the shelf until Aptian times, as indicated by well and palaeogeographic data (Davison, 2005; Vear, 2005; Ye et al., 2017). A significant Cenomanian–Turonian marine transgression is recorded along the Central and equatorial Atlantic margins (Brownfield and Charpentier, 2003). Seismic stratigraphy mapped by Ye et al. (2017) argues for > 200 m of relative sea-level fall during the Late Cretaceous and the backstripping of wells in the offshore Senegal and Mauritanian basins indicates < 1 km of tectonic subsidence occurred during this time (Janssen et al., 1995). The Senonian marks a period of tectonic inversion onshore and subsidence in sedimentary basins across continental Africa and offshore its passive margins. Considering that this period corresponds to a long-term high in eustatic level, locally observed base-level fall across the northwest African continental margin may only be explained by an uplift of the margin (Ye et al., 2017). The creation of < 1 km accommodation offshore and uplift of the margin should result in the accumulation of clastic sediments in basins along the northwest African passive margin during this time. Detailed calculations of sedimentary flux to the West African continental margin and isopach maps are lacking, and are a central theme of this study. Widespread marine deposits across West and North Africa from Eocene–Oligocene times correspond with a change from clastic to carbonate deposition to the northwest African continental margin thus indicat-

ing a lack of clastic sediment supply from onshore source regions during this interval (Sahagian, 1988; Davison, 2005; Vear, 2005; Paul et al., 2014; Chardon et al., 2016; Grimaud et al., 2018). Palaeogeographic reconstructions indicate that the present day West African drainage system stabilised during Eocene–Oligocene times, following the onset of hot-spot related growth of topographic swells such as Hoggar and Tibesti, which led to the characteristic 'basin and swell' physiography of the African continent (Burke, 1996; Chardon et al., 2016; Grimaud et al., 2018). A period of significant long and short wavelength uplift (e.g. long wavelength uplift across Southern Africa and the East African Rift system and short wavelength uplift at localised domal topographic swells) during the last 30 Ma across the African continent is well documented (e.g. Nyblade and Robinson, 1994; Burke, 1996; Al-Hajri et al., 2009; Paul et al., 2014; Rudge et al., 2015). In the case of northwest Africa, Neogene–Recent uplift of topographic swells onshore must have had a significant impact on the supply of clastic sediments produced and delivered to the margin's offshore sedimentary basins. This raises several important questions: are the processes that generate topography onshore across northwest Africa also responsible for controlling the clastic sedimentary budget delivered to the passive continental margin? What has controlled the evolution of African topography since Neogene times and can this be linked to offshore sediment deposition? Finally, can long wavelength changes in surface topography be used to address the 'source' to 'sink' problem for West and potentially other regions of Africa?

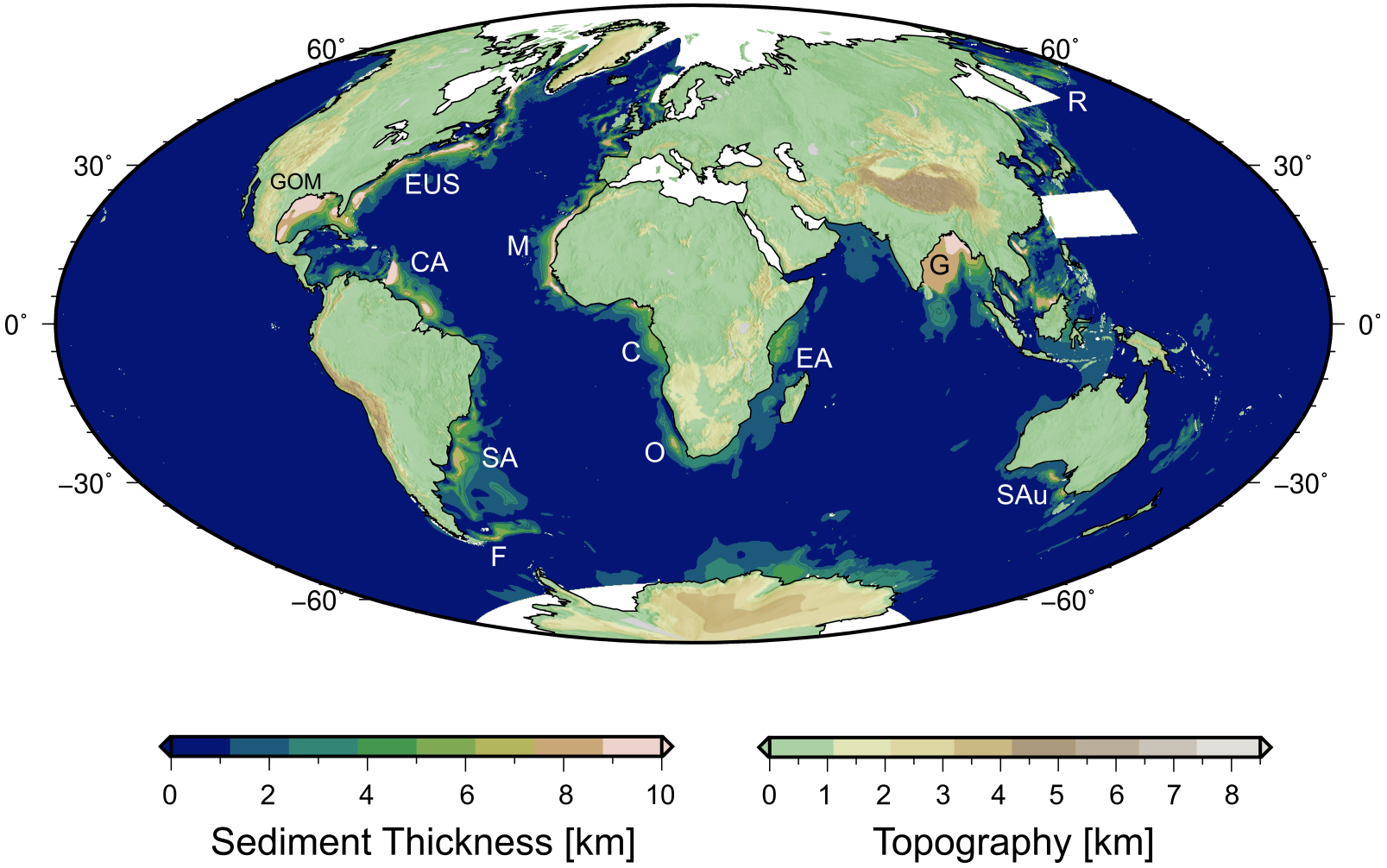


Figure 1: **Global continental topography and offshore sediment thickness.** Global offshore sediment thickness from Whittaker et al. (2013) (updated from Divins, 2003's global sediment compilation) and continental topography plotted using ETOPO1 1 Arc-Minute Global Relief Model from Amante and B.W. (2009). Black/white text labels = major offshore sedimentary basins, GOM = Gulf of Mexico, EUS = Eastern United States, CA = Central America, SA = South America, F = Falklands, M = Mauritania, C = Congo, O = Orange, EA = East Africa, G = Ganges, SAu = South Australia, R = Russia. White polygons = regions where sedimentary thickness data is unavailable.

Dynamic topography and continental uplift in Africa

In the case of Africa, several studies suggest that mantle-driven continental uplift exerts the primary control on the evolution of topography and possibly controls patterns of sediment flux to the continent's passive margin basins. For example, Walford et al. (2005) calculates the solid sedimentary load history of the Zambezi delta, whereby increased sedimentary flux during the Late Cretaceous is consistent with results from apatite fission track work in southwestern Africa, which point to a period of enhanced denudation during this time. Comparison of the palaeo-sediment flux to the Zambezi delta with analysis of the sediment load of modern rivers suggests that the Zambezi may have been elevated from low elevation (< 500 m) to > 1000 m during Cenozoic times (Milliman and Syvitski, 1992; Walford et al., 2005). The change observed by Walford et al. (2005) in the Zambezi Delta may be a response to local or regional uplift. Rouby et al. (2009) determined the long-term (10 Ma) signal of sedimentary supply from 3D mass balance calculations comparing sedimentary volumes deduced from offshore isopach maps and denudation volumes calculated from thermochronology data along the South African and Namibian passive Atlantic continental margins. Their results show that the long-term evolution of preserved sedimentary volume along the Namibian–South African margin is compatible with processes producing uplift and relief variations in the continental hinterland.

The anomalous and bimodal ('basin and swell') physiography of the African continent, whereby $\sim 50\%$ of continental topography lies above 500 m, has been attributed to the presence of a large, dynamically-supported slow velocity anomaly within the lower mantle that is inferred to be a thermochemical superplume beneath the southern half of the continent (Nyblade and Robinson, 1994; Burke, 1996; Gurnis et al., 2000; Al-Hajri et al., 2009; Moucha and Forte, 2011). Beneath East Africa, tomographic images illuminate a broad (c. 500 km wide) low-velocity region in the upper mantle, with possible connection to the African superplume in the lower mantle. Many of Africas secondary topographic features (e.g. Atlas, Hoggar, Bié topographic domal swells) are underlain by slow mantle velocities at depths of 100–150 km and are adjacent to rapid changes in lithospheric thickness (Fishwick and Bastow, 2011). It

is widely accepted that the large-scale extensional features (such as the East African Rift), widespread volcanic activity, anomalously subsided basins and uplifted magmatic and amagmatic domal swells that characterise African topography have developed over the last ~ 30 Ma (e.g. Partridge and Maud, 1987; Burke, 1996; Gurnis et al., 2000; Al-Hajri et al., 2009; Guiraud et al., 2010; Moucha and Forte, 2011). The development of these features was accompanied by a concomitant increase in clastic sedimentary flux to nearly all of the continent's passive margin basins, which suggests that dynamic process may exert a first-order control on the sedimentary budget to Africa's passive margin basins (Dingle, 1983; DuToit et al., 1997; Aal et al., 2000; Hall et al., 2005; Walford et al., 2005; Paul et al., 2014; Grimaud et al., 2018).

There is a general consensus that the anomalous 'basin and swell' physiography of the African continent is a surficial manifestation of convective circulation within the sub-lithospheric mantle (Burke and Gunnell, 2008; Al-Hajri et al., 2009; Paul et al., 2014). Indeed, the petrologic character of intercratonic African volcanics is consistent with the occurrence of a geothermal gradient steep enough to facilitate the formation of lithothermal systems at relatively shallow depths (45–60 km) in the lithosphere (Harris, 1972). Away from the continental interior, mantle flow simulations based on high resolution seismic tomography show that dynamically-supported uplift on the scale of hundreds of metres has occured along the West African passive continental margin (Moucha et al., 2008). This is clearly expressed by the high dynamic topography of the West African continental margin adjacent to the Mauritanian basin and at the Fouta-Djallon topographic swell (Figure 2B). Denudation of localised dynamically-supported magmatic and amagmatic topographic African domal swells (e.g. Hoggar, Tibesti, Darfur, Bié, Angola, Fouta-Djallon) has generated escarpments and extensive erosion surfaces, resulting in the rapid progradation of the deltas of Africa's great rivers which reach the sea (Sykes, 1978; Cox, 1989; Burke, 1996; Ebinger and Sleep, 1998; Furman et al., 2006; Al-Hajri et al., 2009; Fishwick and Bastow, 2011). Hence, the morphology of rivers that cut into regions which are sensitive to changes in dynamic topography may be used to provide constraints on the history past surface elevations. This raises an interesting question which I address in this study: can the morphol-

ogy of drainage patterns in Africa be used constrain the history of continental uplift and predict offshore sedimentary flux to the continent's passive margin basins?

Rivers as recorders of uplift

Constraining the history of vertical plate motions of Africa over the last 30 Ma can be achieved by using the morphologies of longitudinal river profiles as a proxy for regional uplift and erosion (e.g. Hack, 1957; Rosenbloom and Anderson, 1994; Sklar and Dietrich, 1998; Whipple and Tucker, 1999; Tomkin et al., 2003; Crosby and Whipple, 2006; Pritchard et al., 2009; Roberts et al., 2012a,b; Whittaker and Boulton, 2012; Paul et al., 2014; Stephenson et al., 2014; Rudge et al., 2015). Research conducted over the last 15 years builds on the stream-power erosional model by assuming that elevation of points along a river profile is controlled by the history of uplift rate and moderated by the erosional process (Seidl and Dietrich, 1992; Howard et al., 1994; Rosenbloom and Anderson, 1994; Whipple and Tucker, 1999; Whipple et al., 2000; Royden et al., 2000; Whipple, 2002; Clark et al., 2006; Pelletier, 2007; Bishop, 2007). The evolution longitudinal river profiles can be modelled as a function of uplift and erosion, such that

$$\frac{\partial z}{\partial t} = U(x,t) - E(x,t) \tag{1.1}$$

whereby U and E = uplift and erosion as functions of time and space, respectively. The erosive term, E can be parametrised as a function of knickzone retreat, v, upstream drainage area, A and the constants m and n. The terms m and n are positive constants that depend on erosion process, basin hydrology, and channel geometry, such that:

$$E = -vA\,(x)^m \left(\frac{\partial z}{\partial x}\right)^n \tag{1.2}$$

whereby the present-day shapes of longitudinal river profiles, $\partial z/\partial x$, can be extracted from remotely sensed Digital Elevation Model data. The values of the constants v, m and n, must be calculated using independent geologic constraints of uplift. Paul et al. (2014) and Rudge et al. (2015) use this method

to extract ~ 700 longitudinal river profiles from across the African continent and note that whilst short-wavelength (< 10 km) changes in slope (i.e., knickpoints) can be controlled by changes in bedrock lithology, longer-wavelength changes in slope (i.e., knickzones) correlate poorly with lithology. Furthermore, temporal patterns of precipitation rate are generally short compared to the longevity of river profiles (e.g. Cox, 1989). It is likely that the effects of changing precipitation and sedimentary erodibility are subordinate to parameters such as basin area, elevation, and relief (Milliman and Syvitski, 1992; Hovius, 1998; Milliman and Farnsworth, 2011; Paul et al., 2014). This indicates that at long-wavelengths (> 1000 km), changes in dynamic topography and sub-plate support beneath Africa control the evolution of drainage and possibly sediment flux to the continent's passive margins. Stephenson et al. (2014) demonstrates that by not separating solid and solute loads and by assuming that erosion is purely fluvial (i.e. hillslopes are not included), a relatively straightforward prediction of sediment flux can be made by integrating Equation (1.2) along the length of a river.

To invert families of longitudinal river profiles for a best-fitting cumulative uplift rate history of Africa, Rudge et al. (2015) applied a damped non-negative least squared approach by using a limited memory version of the Broyden-Fletcher-Goldfarb-Shanno algorithm (L-BFGS-B), which is suited to problems with large sparse matrices. Other linear least squared algorithms by Goren et al. (2014) and Fox et al. (2014) select a prior model of uplift history by using an estimate of the average uplift rate based upon channel elevation and upstream drainage area observations. Using this method, they calculate a posterior model of uplift history by exploiting an empirical Bayesian approach. However, the posterior model stays close to the prior model and thus inherits some of its attributes (Rudge et al., 2015).

In this study, I build on the advancements made by Paul et al. (2014) and Rudge et al. (2015) by extracting 14700 longitudinal river profiles from across the African continent to invert for a history of uplift rate over the last 30 Ma. I focus on the West Africa's passive continental margin and predict the pattern of offshore sedimentary flux delivered to the margin by continental drainage.

Mauritanian source to sink problem

The link between sediment 'sources' and 'sinks' may be tested quantitatively by comparing the pattern of offshore sedimentary flux calculated by measuring offshore sediment volumes to predictions calculated by drainage inversion. Several important factors must be considered when choosing a suitable location to conduct this study:

- Can the region of continental lithosphere that is being incised by onshore drainage be linked to an offshore sedimentary basin on a continental margin?
- Has the region remained relatively tectonically stable for a geologically significant period of time?
- Has the region been subject to sub-lithospheric processes which have caused uplift and erosion onshore and subsidence offshore?

The Mauritanian basin, which forms part of the larger Mauritania-Senegal-Guinea-Bissau-Conarky (MSGBC) Basin, is relatively under-explored compared to West Africa's other major passive margin sedimentary basins (e.g. Niger Delta, Angola, Namibia). However, several recent high-profile hydrocarbon discoveries have put the region into the spotlight (e.g. oil discoveries in the Banda and Tiof Fields in Neogene sandstones and gas discoveries in the Pelican Field in Upper Cretaceous sandstone reservoirs). The existence of the Mauritanian basin and discoveries of Neogene clastic hydrocarbon reservoirs is somewhat peculiar given the fact that it lies on a passive continental margin and has not experienced rifting or lithospheric stretching since the margin's separation from Gondwana at ~ 225 Ma (Brownfield and Charpentier, 2003; Vear, 2005; Davison, 2005). Sediment deposited to the Mauritanian basin is supplied by the Senegal river and those draining the dynamically-supported Fouta-Djallon topographic swell (Figure 2B). Global sediment thickness data compiled from previously published isopach maps, ocean drilling results and archived seismic reflection profiles indicate that < 10 km of sedimentary rock is present in the Maurtianian basin (Figure 2A, Divins, 2003; Whittaker et al., 2013). Data on the subsidence history of the Mauritanian basin is scarce. However, Janssen

et al. (1995) backstrip 200 wells from 14 African sedimentary basins to argue that a comparison between subsidence histories of the continent's basins and the breakup history of Gondwana shows that a strong correlation can be established between changes in plate motions and reactivation of extensional basins in the African plate. They are unable to explain what causes Neogene–Recent subsidence in the Mauritanian basin and tentatively suggest that this is caused by halokinetic movements due to the presence of Upper Triassic–Jurassic salt. The causes of Neoegene–Recent subsidence within recent geological history in the Mauritanian basin were unknown, until now.

I use a database of commercial seismic and well data to constrain stratigraphy in the Mauritanian basin, offshore West Africa, and calculate a history of Late Cretaceous–Recent sedimentary flux for the first time. Backstripping of the wells in my inventory is used to calculate the subsidence history of the basin. I use an updated version of Fishwick (2010)'s tomographic model for West Africa to calculate upper mantle temperatures from the Mauritanian margin to the Cape Verde hotspot using two parametrisations (mineral physics approach of Goes et al., 2012 and empical approach of Priestley and McKenzie, 2006). I combine calculations of residual ocean-age depths calculated from seismic data presented in this study for the first time to the global database of Hoggard et al. (2017) to explore the causes of basin subsidence from Neogene–Recent times. Finally, I extract 14700 longitudinal river profiles from across the African continent to invert for a history of continental uplift. I address the 'source to sink' problem by comparing the pattern of sedimentary flux to West Africa's passive continental margin predicted from drainage inversion to calculations made using offshore data in the Mauritanian basin from Neogene–Recent times. The results of this study synthesise dynamic subsidence, continental uplift and offshore sedimentary deposition to West Africa's passive margin. A summary of each chapter of this thesis is outlined in the next section.

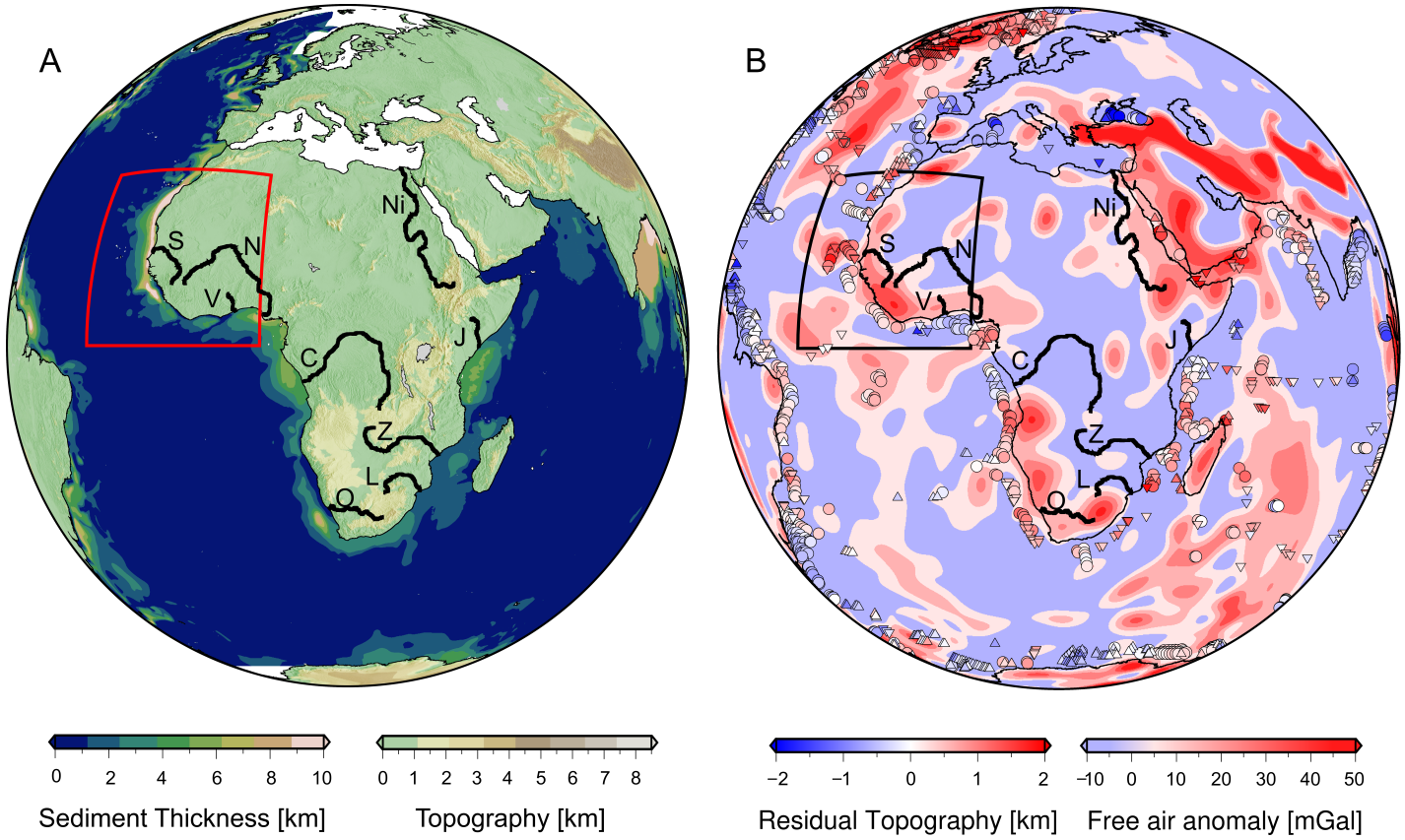


Figure 2: **Major African rivers, continental topography, offshore sediment thickness, residual topography, dynamic topography.** (A) African offshore sediment thickness from Whittaker et al. (2013) and continental topography plotted using ETOPO1 1 Arc-Minute Global Relief Model from Amante and B.W. (2009). White polygons = regions where sedimentary thickness data is unavailable. (B) Dynamic topography and ocean-age depths. Continental Red/blue colour scale = dynamic topography calculated using long wavelength ($\sim$ 800–2500 km) free-air gravity data from GOCE dataset and an admittance $Z = 35$ mGal km^{-1} (see e.g. Tapley et al., 2005; Jones et al., 2012; Förste et al., 2014); contour interval = 10 mGal $\sim$ 0.3 km. Circles/upward/downward pointing triangles = accurate/minimum/maximum residual ocean-age depth estimates Hoggard et al., 2017) Black lines = major African rivers, S = Senegal, N = Niger, V = Volta, C = Congo, O = Orange, L = Limpopo, Z = Zambezi, J = Jubba-Shebelle, Ni = Nile. Red & black polygons on (A) and (B) = study area.

1.2 Thesis structure

Chapter 2: Stratigraphy and sedimentary flux history of the Mauritanian basin

In this chapter, I use a database of 8 commercial wells and 38 two-dimensional seismic lines with record lengths of 8–10 seconds to map stratigraphy in the Mauritanian basin. Seven prominent acoustic impedance anomalies are identified and correlated across the basin using seismic well-ties. Biostratigraphic data from wells is used to date each stratigraphic horizon and to constrain the Cretaceous–Recent chronostratigraphy of the basin. Check-shot data from wells are used to determine the best-fitting numerical parameters (initial porosity and compaction wavelength) in order to convert stratigraphic horizons mapped in two-way time to depth and to remove the effects of sediment and water loading. The distribution and volumes of sedimentary rock between mapped stratigraphic horizons and the Cenozoic–Recent sediment flux history of the Mauritanian basin are calculated in this study for the first time.

Chapter 3: Shallow mantle convection beneath the Mauritanian basin

In this chapter, the origins of the Mauritanian basin are explored. Well data are used to calculate the subsidence history of the Mauritanian basin, corrected for water-loading and palaeo-water depths. The position of the Moho as determined by seismic data is used to calculate residual depth anomalies across the Mauritanian basin. A tomographic model for West Africa is used to calculate upper mantle temperatures and the depth to the 1330°C isotherm along a profile beneath the Mauritanian basin and Cape Verde hotspot by applying both a mineral physics and empirical parametrisation to convert shear-wave velocities to temperature. The causes of subsidence beneath the Mauritanian basin are explored by integrating geological, geophysical and shear wave tomographic results.

Chapter 4: African uplift and sedimentary flux from continental drainage inversion

In this chapter, I extract 14700 longitudinal river profiles from remote sensing data across the African continent. I apply a linear two-dimensional inverse model to calculate the best-fitting cumulative uplift history for the African continent during the last 30 Ma by inverting continental drainage profiles. Finally, the cumulative uplift history of rivers draining into the Mauritanian basin is applied to predict patterns of solid sedimentary flux produced due to the dynamic uplift of West Africa's passive continental margin from 30 Ma to Recent times. Predicted patterns of solid sedimentary flux calculated from drainage inversion are compared to fluxes calculated from offshore seismic and well data.

Chapter 5: Future work & conclusions

In this section, I summarise the results of each chapter and discuss the implications of these results. Several open questions regarding the application of the inverse method to the 'source to sink' problem are discussed. Firstly, how far far back in time can we go? Secondly, what are the implications for industry? Finally, can this method be applied to localised studies and be applied to predict marine benthic environments?

Chapter 2

Stratigraphy and sedimentary flux history of the Mauritanian basin

2.1 Northwest Africa

West Africa's relative tectonic stability since the onset of Triassic separation from Gondwana, it's isolation from other sources of continental clastic sedimentation and position adjacent to dynamically supported topographic swells (e.g. Atlas and Fouta-Djallon, Figure 3) drained by rivers that deliver sediments to offshore sedimentary basins, make it a useful laboratory to study the 'source to sink' problem (Davison, 2005). In this chapter, I focus on the northwest African margin, and calculate the Late Cretaceous–Recent solid sedimentary flux history of the Mauritanian basin using an inventory of seismic and well data provided by TGS & Tullow Oil Plc. Today, this region is drained by rivers that carry sediment through the Mauritanides fold-belt, which extends from the northern High-Atlas of Morocco to southern Senegal, and disgorge into the Atlantic Ocean (Villeneuve, 2005; Figure 3). The modern Senegal catchment drains the northern part of the Fouta Djallon swell and delivers sediment to the Atlantic Ocean at rates of ~ 3 Mt a^{-1} (Milliman and Farnsworth, 2013). Atop the Fouta Djallon swell, drainage networks are arranged in a broadly radial pattern (Figure 3). Rivers draining into the Atlantic margin of northwest Africa are bounded to the north by the Atlas mountains. This topographic swell is also drained by fluvial networks with an approximately radial pattern (Figure 3).

Hydrocarbon exploration offshore northwest Africa has generated a body of seismic and well data that constrain the stratigraphy of the margin. Gas discoveries have been made in Upper Cretaceous sandstone reservoirs in the Pelican, Tortue and Yakaar fields in the wider MSGBC basin. Oil discoveries at the Chinguetti and Tiof fields have been made in Cenozoic sandstone reservoirs and are probably charged by Cenomanian–Turonian source rocks (Brownfield and Charpentier, 2003; Davison, 2005; Vear, 2005). However, the distribution of sediments, sedimentary flux history and chronostratigraphy of the Mauritanian basin remain yet to be discovered.

My approach to mapping and examining the history of sedimentary flux to the Mauritanian basin builds on these observations and has three steps. Firstly, I mapped basin stratigraphy using commercial two-dimensional seismic and well data, provided courtesy of Tullow Oil Plc and TGS. Secondly, volumes of sedimentary rock present between dated and mapped seismic horizons are corrected for the effects of porosity and compaction. The distribution of sedimentary rock in the Mauritanian basin was used to calculate the Late Cretaceous–Recent history of sedimentary flux. Results from this chapter will be used to bring together measurements of offshore sedimentary deposition with observations of continental uplift and erosion in a step towards generating a predictive framework for the African 'source-to-sink' sedimentary routing system.

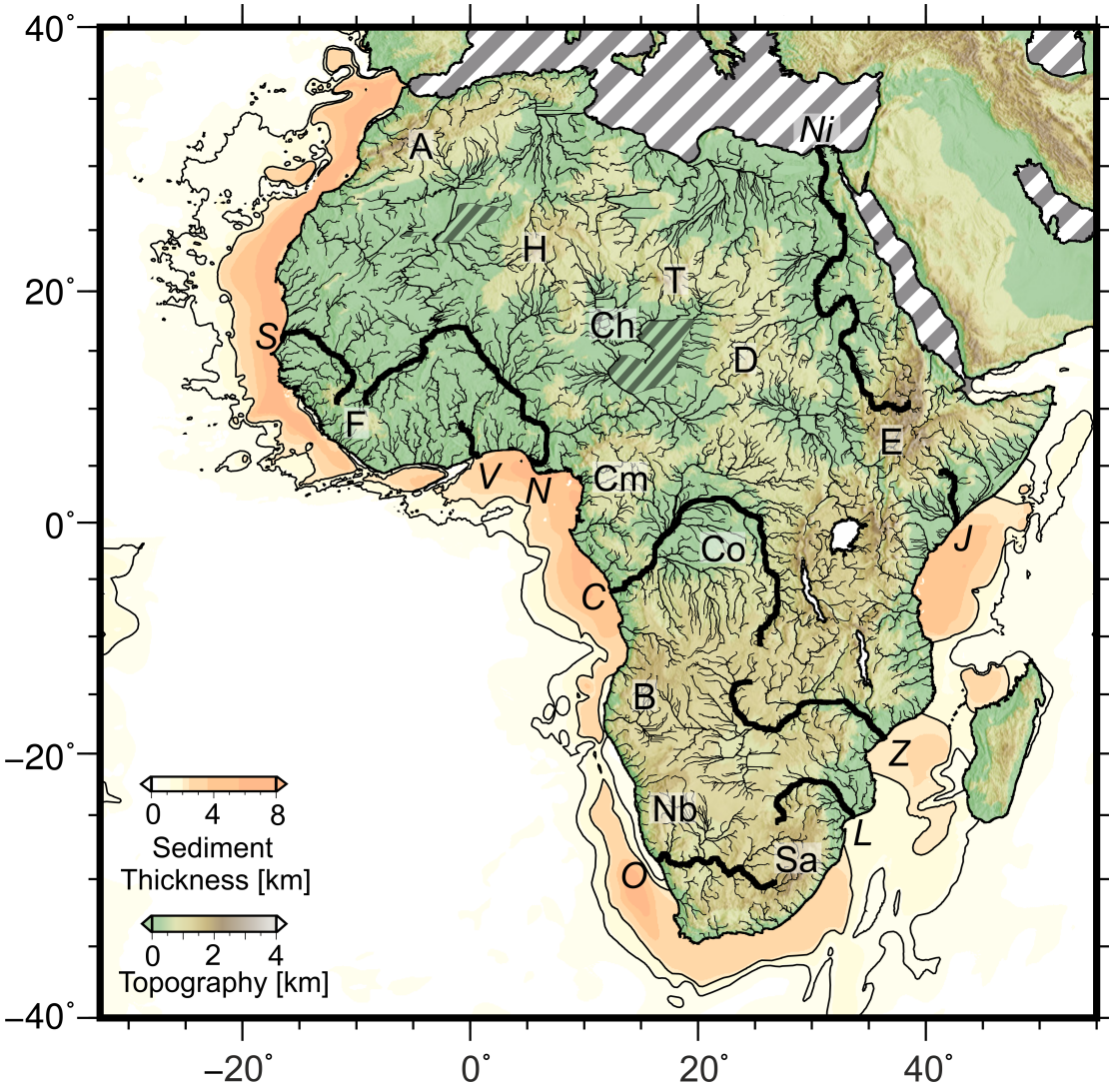


Figure 3: **African topography, drainage and sedimentary rock offshore**. Black lines onshore = drainage networks extracted from 90 × 90 m SRTM dataset. Thick black lines = principal African river catchments, *S* = Senegal, *V* = Volta, *N* = Niger, *C* = Congo, *O* = Orange, *L* = Limpopo, *Z* = Zambezi, *J* = Jubba-Shebelle and *Ni* = Nile. Topographic swell labels: A = Atlas, F = Fouta-Djallon, H = Hoggar. T = Tibesti, D = Darfur, Cm = Cameroon, B = Bíe, Nb = Namibia, Sa = South Africa, E = Ethiopian Plateau. Continental basins labelled C = Congo and Ch = Chad. Thin hatchet pattern covers regions with unreliable drainage extraction. Colour scale offshore = thickness of sedimentary rock from Whittaker et al. (2013). Contours indicate thicknesses of 2 km and 4 km. Thick hatchet pattern = regions of no data. The methodology used to extract drainage from remote sensing data is described in Chapter 4.

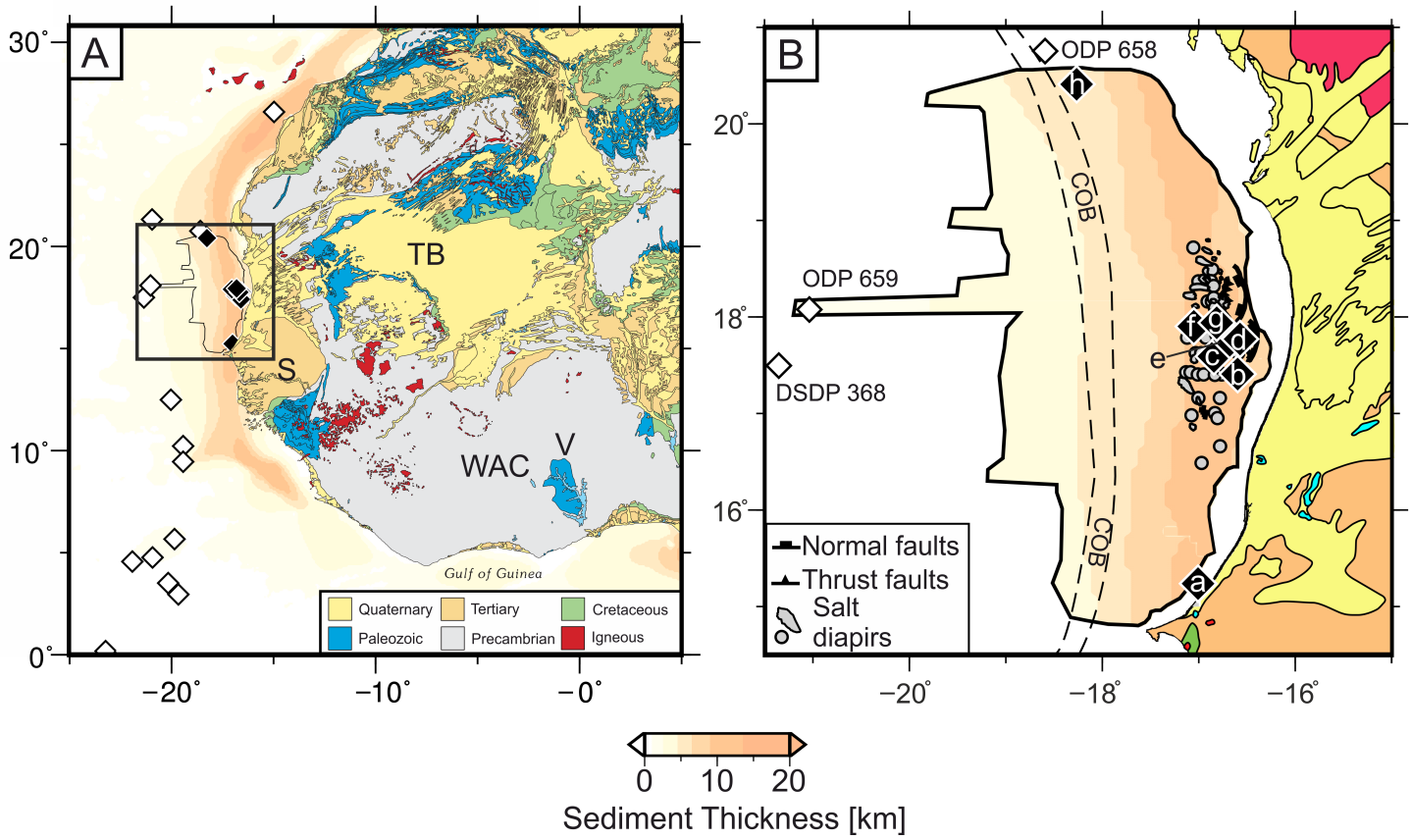


Figure 4: **Mauritanian margin and surroundings.** (A) Geological map and offshore sedimentary thickness of West Africa (after Brownfield and Charpentier, 2003; Whittaker et al., 2013; Lodhia et al., 2018). S = Senegal; TB = Tauodenni basin; WAC = West African craton; V = Volta. Black diamonds = commercial wells used in this study; white diamonds = ODP/DSDP wells. Black square = extent of panel B. (B) Black polygon = region covered by seismic survey used in this study. Black labelled diamonds = commercial wells A–H. Dashed lines labelled COB = continent-ocean boundary mapped from reflection seismic data in this study.

2.2 Data

2.2.1 Well data

An inventory of eight commercial wells located across the Mauritanian basin is used to map stratigraphy and provide biostratigraphic age constraints. The wells are located in the north, centre and south of the basin and are summarised in Table 1. Standard N and CN schemes have been used to calibrate the planktonic foraminiferal and calcareous nannoplankton assemblages, respectively. Eighteen biostratigraphically constrained stratigraphic horizons are identified in the basin (Table 2). Of these, seven prominent acoustic impedance anomalies identified as seismic marker horizons are interpreted and mapped across the dataset. Well data are used to determine the ages of these marker horizons (seabed; 5.6 Ma; 23.8 Ma; 58.4 Ma; 70.4 Ma; 89.0 Ma and basement; Figure 5).

The deepest well in my inventory encounters over 4000 m of Jurassic–Pliocene stratigraphy (Well B; Figure 5). Upper Jurassic–Albian stratigraphy is dominated by platform carbonates (limestones), which are characterised on seismic data by reflectors with high amplitude anomalies and steeply-dipping margins. Platform carbonates extend across the continental margin of the basin (Figure 6 & 7). Upper Cretaceous–Paleocene stratigraphy in the centre of the basin is almost exclusively clastic (e.g. claystones, shale, siltstones and sandstones), whereas $\sim$500 m of limestone is encountered at Well A in the south of the Mauritanian basin. Almost all of the rock between the 58.4 Ma and 23.8 Ma (Eocene–Miocene) marker horizons is carbonate. Increased incision along the continental margin is observed in the centre of the basin at Well D where the majority of Oligocene–Eocene stratigraphy has been removed. Importantly, Miocene–Recent clastic stratigraphy encountered at all wells consists of sandstones and claystones/shale on the continental shelf and basin floor, respectively. Rock recovered from the upper sections (100–1000 m) of all wells are characterised by unconsolidated claystones and shales with high porosity. The water depth, palaeo-water depths and stratigraphy of each well are summarised on Table 1.

Well	Water Depth [m]	First sample depth [km]	Total Depth [m]	Stratigraphic range	Benthonic biofacies (e.g.)	Paleo-water depth
A	79	~ 0.3	3167	Eocene-Albian	*Triorites africaensis & Cibicides lobatulus*	
B	172	~ 1.3	4977	Pliocene-Upper Jurassic	*Gabonisporis vigourpxi & Lucianorhabdus compactus*	UB-N
C	1266	~ 2.2	3080	Miocene	*Bulmina costata*	MB
D	281	~ 1.0	2608	Miocene-Eocene	*Cibicidoides grosseperforatus*	UB-LB
E	490	~ 1.4	2715	Miocene-Eocene	*Epinoides vicksburgenis*	UB
F	1776	~ 2.7	3060	Miocene-Eocene	*Bulimina costata & Turborotalia passagnoensis*	UB-LB
G	1120	~ 2.1	2908	Miocene-Oligocene	*Bulmina striata & Caenopedina cubensis*	MB-LB
H	1414	~ 1.9	3299	Eocene-Upper Cretaceous	*Cibicidoides grimsdale*	B

Table 1: **Summary of wells used in this study.** WD = water-depth; FR = depth to first rock samples; TD = total depth; PWD = palaeo-water depth. Palaeo-water depths are based on the following definitions from Immenhauser (2009): Neritic (N) = 0–150 m; upper bathyal (UB) = 150–500 m, middle bathyal (MB) = 500–2000 m; lower bathyal (LB) = >2000 m; bathyal (B) = >150 m.

Horizon [age, Ma]	Type	Occurrence	Species	Biostratigraphic range	Well	Reference
5.6	**PF**	**FO**	**G. tumida**	**Present - Messinian**	**E**	**Wade et al. (2011)**
11.4	PF	LO	G. mayeri	Mid. Miocene - Mid. Oligocene	G, C, F	Bolli et al. (1989)
12.7	PF	FO	G. praefohsi	Mid. Miocene	C, F	Blow (1969); Kennett and Srinivasan (1983); Wade et al. (2011)
15.1	PF	FO	Orbunia sp.	Holocene - Miocene	C, F	Young et al. (2018)
23.8	**PF**	**FO**	**G. kugleri**	**Early Miocene**	**E, G**	**Blow (1969); Berggren et al. (1995)**
29.0	PF	LO	G. increbescens	E. Oligicene - Mid. Eocene	G	Bandy., 1949, Blow., 1979, Leckie et al. (1993)
45.7	PF	FO	T. giffinae	Eocene	D	Olsson et al. (2006)
53.7	CN	FO	S. editus	Early Eocene	B	Perch-Nielsen et al. (1978)
58.4	**CN**	**FO**	**F. bitectus**	**Paleocene**	**H**	**Romein (1979); Monechi et al. (2013)**
58.4	**PF**	**LO**	**G. psuedomenardii**	**Paleocene**	**A**	**Bolli (1957b,a); Olsson et al. (1999)**
58.4	**CN**	**LO**	**C. tenuis**	**Paleocene**	**B**	**Perch-Nielsen (1977); Varol (1989)**
62.3	PF	FO	G. angulata	Paleocene	A	Olsson et al., 1999
70.4	**CN**	**LO**	**T. phacelosus**	**Cretaceous**	**B**	**Brown et al. (1998); Burnett (1998)**
75.9	CN	LO	L. grilli	Late Cretaceous	B	Burnett (1998)
78.0	PS	FO	R. fornicata	Cretaceous	A	Plummer (1931)
81.3	CN	LO	B. hayi	Late Cretaceous	B	Burnett (1998)
84.9	CN	LO	L. moratus	Late Cretaceous	B	Burnett (1998)
89.0	**CN**	**FO**	**M. furcatus**	**Late Cretaceous**	**B**	**Bolli et al. (1989); Burnett (1998)**
89.0	**PS**	**LO**	**T. africaensis**	**Cretaceous**	**A**	**Jardiné and Magloire (1965)**
94.0	CN	LO	R. cushmani	Cretaceous	B	Sigal (1948)
139.4	CN	LO	U. gr. granulosa	Cretaceous - Jurassic	B	Bralower et al. (1989)

Table 2: **Biostratigraphy of seismic horizons identified at wells in this study**. Seismic horizons in bold are correlated across the basin (Figures 3 & 4), depth converted and decompacted (Figure 6) to calculate isopachs (Figure 7). PF = planktonic foraminifera, CN = calcareous nannofossil, PS = palynofossil, FO = first occurrence, LO = last occurrence.

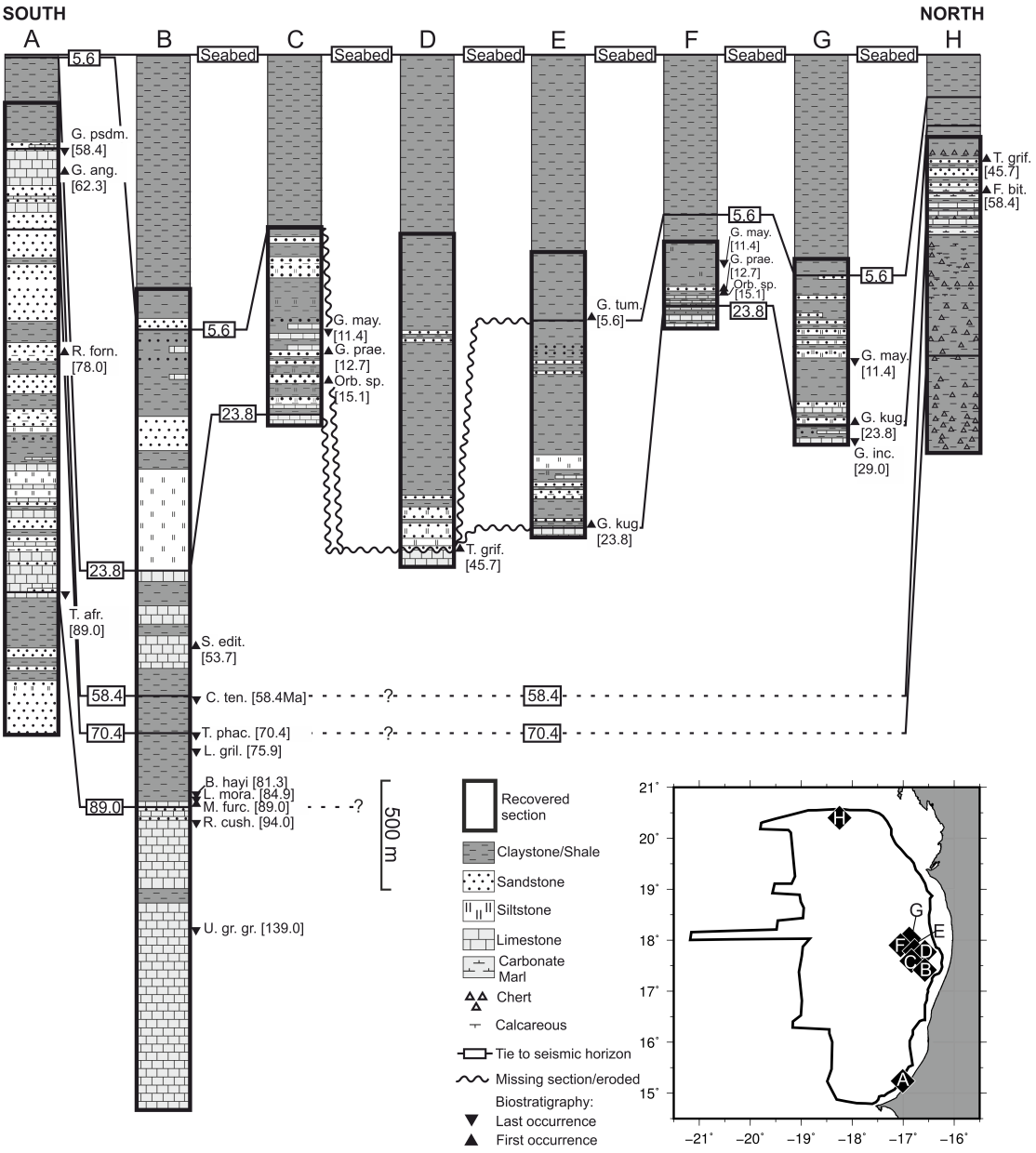


Figure 5: **Mauritanian stratigraphy**. Correlation of stratigraphy recorded in wells. Biostratigraphy including first and last occurrences and age are abbreviated in this figure and described in Table 1. Inset map shows location of wells.

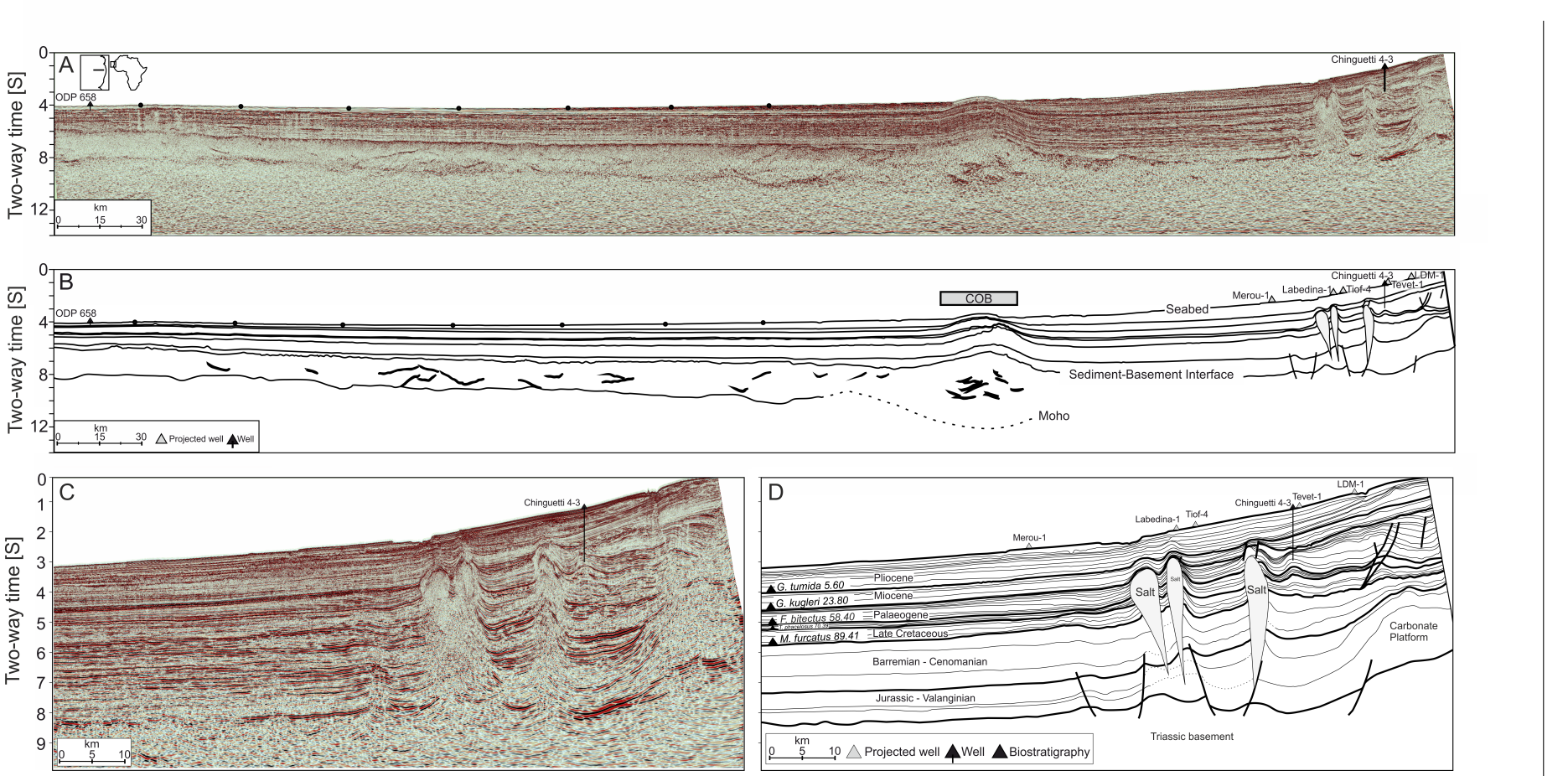


Figure 6: **Seismic data.** (A) Seismic dip-line from TGS dataset (see inset map). Imagery is generally excellent away from salt. Black circles = location of residual ocean age depth measurements used in Chapter 3. (B) Interpreted seismic line. Chronostratigraphy is based on seismic and well data (see body text). Note this line intersects oceanic lithosphere. (C-D) Eastern portion of line. Note thick Miocene to Recent sedimentary rock with no/minor stratigraphic growth. Seismic data provided courtesy of TGS.

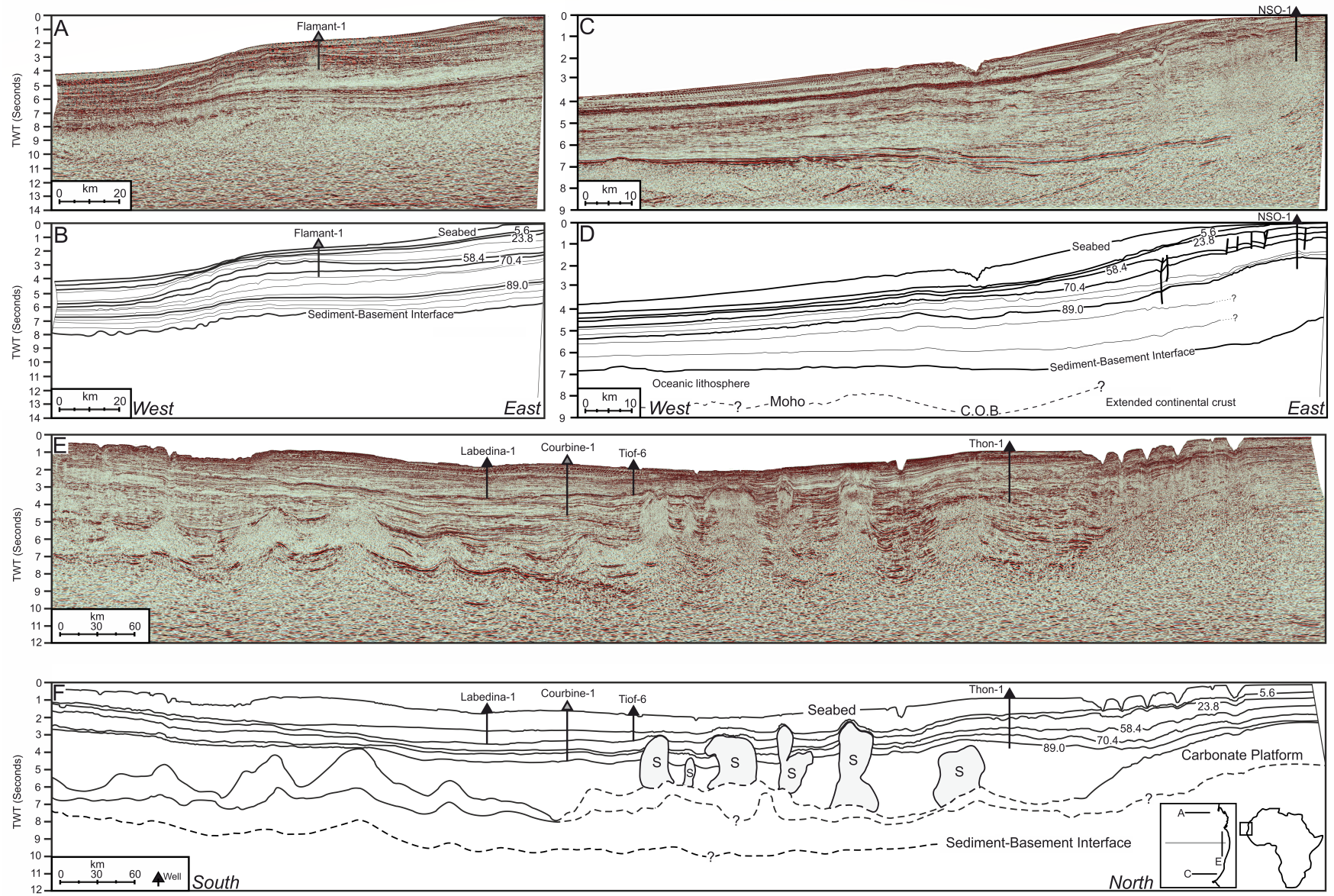


Figure 7: **Seismic data**. (A-B) Northern seismic line and interpretation. (C-D) Southern seismic line and interpretation. (E-F) North-South strike line in the centre of the Mauritanian basin and interpretation. Imagery is generally excellent away from salt. Black lines labelled on inset map = positions of seismic lines in this study. Grey line on inset map = location of seismic dip line intersecting the study area from Lodhia et al. (2018) and Figure 6. Seismic data provided courtesy of TGS.

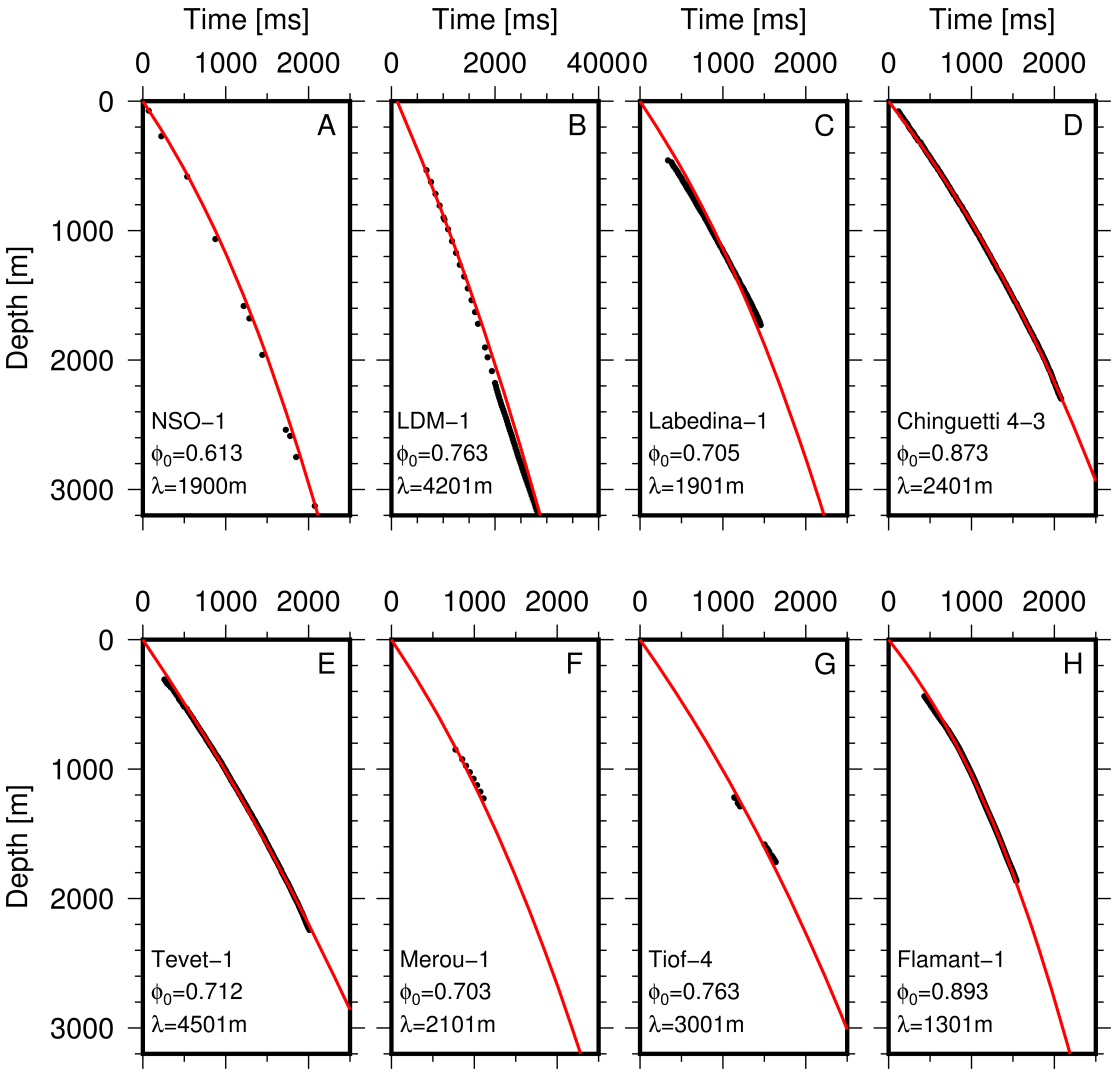


Figure 8: **Check shot data for Mauritanian wells**. Best-fitting compaction parameters (initial porosity, $\phi_\circ$, and compaction wavelength, λ) were determined by minimising misfit between observed check shot data and calculated time-depth curves (red crosses; Figure 9).

Due to data confidentiality, lithologic descriptions of wells and logs have been removed for the public version of this thesis. For access, please contact Tullow Oil Plc or the Ministère du Pétrol de l'Energie et des Mines, Mauritania.

2.2.2 Seismic & check-shot data

Mauritanian stratigraphy was mapped using 8 oil and gas industry wells, 1 IODP well and 38 two-dimensional seismic lines from the TGS 'Dolphin' survey, which had a 10×5 km grid spacing and record lengths of 8–10 seconds two-

way time (TWT). The region covered by the seismic survey used in this study is shown by the black polygon in Figure 4B. Figure 6 shows seismic data from a regional dip line that extends ~ 500 km from the centre of the Mauritanian margin towards the Cape Verde Rise. Figure 7A–D shows seismic data from the northern and southern portions of the Mauritanian basin, and Figure 7E–F shows a strike-line which intersects the basin from north to south. The quality and resolution of the seismic data is generally very good and only deteriorates beneath salt structures. To determine the relationship between two-way time and depth, check-shot data from each well are used to calculate an average regional velocity model (Section 2.3; Figure 9).

2.3 Methodology to calculate solid sedimentary flux

Stratigraphy

To determine the solid sedimentary flux history of the Mauritanian basin, I first mapped the distribution of sedimentary rock using my database of seismic and well data. Eighteen biostratigraphically-constrained stratigraphic horizons were identified using well data (Tables 1 & 2). The oldest horizon encountered in the basin is 139 Ma at a depth of 4150 m at Well B, and is underlain by Cretaceous–Jurassic platform carbonates at this well. Of the 18 stratigraphic horizons identified, 7 horizons marked by prominent acoustic impedance anomalies are mapped in two-way time (bold text in Table 2). These horizons are correlated using seismic-well ties across the basin (Appendix 1, Figure 35) and are used to generate isopachs from which volumes of sedimentary rock are calculated (Figure 6 and Figure 7). A regional chronostratigraphy of the Mauritanian basin produced using my inventory of seismic and well data is shown in Figure 10. Ages of hydrocarbon source rock and reservoir intervals are from Vear (2005) and Davison (2005).

Regional velocity model & depth conversion

Check shot data from each well were used to construct a regional velocity model. As all wells are approximately vertical (i.e. they have minimal hori-

zontal deviations) and velocities are broadly similar, I used mean time-depth values to generate a mean velocity model of the form $z(t) = 0.0017t^2 + 0.9t - 34$, where t = two-way travel time in ms. This model was used to calculate the depth of each mapped horizon.

Uncertainties were determined by calculating one standard deviation, $\pm\sigma$, above and below the mean time-depth relationship, μ. The $+\sigma$ velocity model has the form $z(t) = 0.000134t^2 + 0.8t + 38$ and the $-\sigma$ velocity model has the form $z(t) = 0.000232t^2 + 0.9t - 129$. Figure 17 shows check-shot data, mean and $\pm\sigma$ time-depth relationships for each well. Seismic horizons converted from time to depth using the mean time-depth relationship are shown on Figure 36 in Appendix 1.

Compaction parametrisation & decompaction

In order to calculate solid sedimentary flux, it is necessary to first correct for compaction caused by sediment and water-loading. Porosity, ϕ , was parametrised using Athy (1930)'s formulation,

$$\phi = \phi_\circ \exp\left(-\frac{z}{\lambda}\right) \tag{2.1}$$

The initial porosity, $\phi_\circ$, and compaction wavelength, λ, were constrained using a simple empirical relationship between velocity as a function of depth, $v(z)$, and compaction, such that

$$\frac{1}{v(z)} = \frac{\phi(z)}{v_w} + \frac{1-\phi(z)}{v_{sg}}, \tag{2.2}$$

where v_w is pore fluid velocity and v_{sg} is solid grain velocity (Wyllie et al., 1956). For seawater, $v_w = 1.5$ km s^{-1}. I assume that $v_{sg} = 5.5 \pm 0.5$ km s^{-1}, which is appropriate for a mixture of sand and clay (Christensen, 1982). Since two-way time, $t = 2\int_0^z \mathrm{d}z/v(z)$, Equations (2.1) & (2.2) can be combined to obtain:

$$\frac{t}{2} = \frac{z}{v_{sg}} + \phi_\circ\lambda\left(\frac{1}{v_w} - \frac{1}{v_{sg}}\right)\left[1 - \exp\left(-\frac{z}{\lambda}\right)\right] \tag{2.3}$$

I seek the minimum root-mean-squared (rms) misfit between observed and theoretical time-depth values by varying $\phi_\circ$ and λ (Figure 9), by minimising:

$$\text{rms} = \sqrt{\frac{1}{N}\sum_{i=1}^{N}(t_o^i - t_c^i)^2} \tag{2.4}$$

where t_o and t_c are observed and calculated times and N is the number of time-depth measurements.

The effects of loading are removed (i.e. decompacted) by calculating thickness of the sedimentary layer $z_1 z_2$ when deposited at the surface, $z_3 z_4$. At the surface $z_3 = 0$. As the solid component must remain constant during compaction we can integrate

$$\int_{z_1}^{z_2}(1-\phi)\mathrm{d}z = \int_{0}^{z_4}(1-\phi)\mathrm{d}z \tag{2.5}$$

to obtain

$$z_4 = z_2 - z_1 + \phi_\circ\lambda\left[\exp\left(-\frac{z_2}{\lambda}\right) + \exp\left(-\frac{z_1}{\lambda}\right) + 1 - \exp\left(-\frac{z_4}{\lambda}\right)\right] \tag{2.6}$$

z_4 is solved by the iterative Newton-Raphson method.

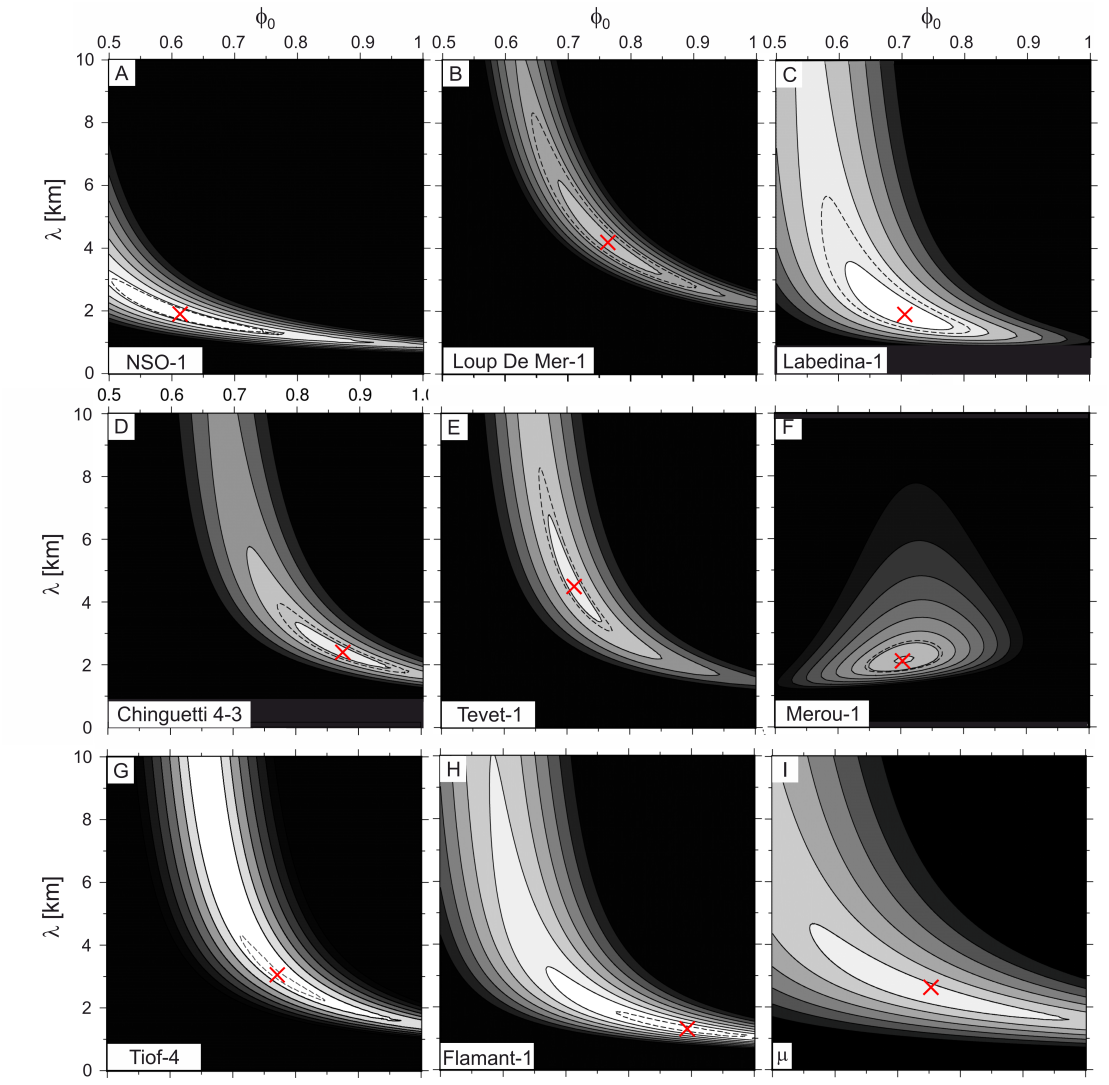


Figure 9: **Compaction parametrisation**. (A–H) Root-mean-squared (rms) misfit between observed and calculated time-depth curves plotted as a function of initial porosity, $\phi_\circ$, and compaction decay length, λ. Red crosses = compaction parameters with lowest residual misfit to time-depth data (Figure 8); dashed lines = contours of misfit used to estimate compaction uncertainties. (I) Regional compaction parametrisation. Root-mean-squared (rms) misfit between observed mean and calculated time-depth curves plotted as a function of initial porosity and compaction decay length. Red cross = best-fitting compaction parameters with lowest residual misfit to time-depth data calculated from the mean $\phi_\circ$ & λ from all wells.

Solid sediment thickness

The solid sediment thickness, T_{sol}, between seismic horizons was calculated using:

$$T_{sol} = z_2 - z_1 + \phi_\circ \lambda \left[\exp\left(-\frac{z_2}{\lambda}\right) - \exp\left(-\frac{z_1}{\lambda}\right) \right] \quad (2.7)$$

which corrects for the effects of compaction (Walford et al., 2005). I use the compaction parameters, $\phi_\circ = 0.75 \pm 0.1$, $\lambda = 2.66 \pm 1.2$ km, that best-fit the mean time-depth pairs of all check-shot data for the wells in my database (Figure 9). z_1 and z_2 are the depths of the top and bottom of a seismic interval, respectively (see e.g. Walford et al., 2005). Solid sedimentary thickness of rock in the Mauritanian basin is shown in Figure 11. Solid sedimentary fluxes are summarised on Table 3 and are shown on Figures 11 & 12. Uncorrected sediment thicknesses between mapped stratigraphic horizons are shown on Figure 37 in Appendix 1.

2.4 Ages of acoustic basement and salt

Up to 8 km of sedimentary rock is present between the acoustic basement and the oldest correlated seismic horizon, 89.0 Ma (Turonian), in the Mauritanian basin (Figure 11F). The extent of the Mauritanian salt and underlying rift basins can be seen occasionally in the seismic data and covers some parts of the study area (Figure 6 and Figure 7E-F). The earliest phase of Atlantic margin deposition in northwest Africa is recorded by red-bed sandstones, typical of an arid continental environment, which dominate the Triassic section in the Essaouira Basin of Morocco, (Vear, 2005). In common with previous authors, I assume a Late Triassic (~ 225 Ma) age for the acoustic basement based on Moroccan analogues to the north of the Mauritanian basin (e.g. Brownfield and Charpentier, 2003; Vear, 2005; Davison, 2005). All known intersections of salt within the MSGBC basin (Casamance-1, Maritime-3, 5, 8 in Senegal and Chinguetti-1 in Mauritania) are allochthonous (Vear, 2005). There are no intersections of syn-rift evaporites at any wells in MSGBC basin. However, analogues of syn-rift evaporites deposited during the later stages of rifting in the Proto-Central Atlantic ocean in the axes of the Triassic-Early Jurassic graben

are recovered north of the MSGBC basin along the northwest African margin in Morocco and Algeria (Vear, 2005). In common with previous authors, I assume an Early Jurassic age for syn-rift salt deposition in the MSGBC (including the Mauritanian) basin based on Moroccan analogues further north (Emery and Uchupi, 1984; Brownfield and Charpentier, 2003; Vear, 2005; Davison, 2005). In the Essaouira Basin of Morocco the most complete stratigraphy was encountered in well JRP-1 (see Figure 6B in Davison, 2005). Central Atlantic Magmatic Province (CAMP) basalts have been found below, within, and above the Triassic evaporite sequence (see Figure 6B in Hafid et al., 2000), which indicates that the age of the salt is 200 ± 1 Ma (Early Jurassic; Davison, 2005).

2.5 Solid sedimentary flux of the Mauritanian basin

89.0 Ma – Basement

The total thickness of solid sedimentary rock deposited to the study area from the commencement of rifting due to the breakup of Gondwana (~ 225 Ma) to the age of the oldest dated Turonian seismic marker horizon (89.0 Ma) is shown on Figure 11F. Up to 8 km of solid sediment is present in this interval and consists of both syn-rift and post-rift sequences. Solid sediment thickness in this interval decreases basinwards (from east to west) and is thickest in areas affected by halokensis along the West African continental margin. The quality of seismic data beneath salt diapirs and sheets is poor, however some basin structure can be identified by acoustic impedence anomalies interpreted as faults due to rifting (Figure 6C–D).

Syn-rift carbonate deposition to the Mauritanian basin is similar to that of the southern Senegal basin, and consists principally of thick Triassic–Early Jurassic evaporites overlying inferred Triassic clastic rocks, which may include organic-rich lacustrine rocks (Uchupi et al., 1976; Brownfield and Charpentier, 2003). A major post-rift marine carbonate platform extends across the entire eastern edge of the Mauritanian basin and comprises the majority of Early Jurassic to Late Cretaceous stratigraphy. This regional carbonate platform is penetrated by Well B and ceases at the Valaginian aged horizon, 139.0 Ma (Table

??). Samples collected from Well B show that there was a significant change in depositional facies from carbonate to clastic during the Valaginian. The longevity of the regional carbonate platform across the eastern margin of the Mauritanian basin indicates that continental topographic gradients must have been low and clastic sedimentation to the Mauritanian basin must have been minimal until the death of the platform at 139.0 Ma. During the Valaginian, a major regression took place and carbonate platforms along the entire northwest African margin were drowned, suffocated and covered by prograding delta clastics (e.g. Boudjour and Tan Tan deltas, Davison, 2005). A prominent acoustic impedence anomaly identified in seismic data above the carbonate platform is tentatively inferred to represent this Valanginian regression surface (Figure 6C–D). This was followed by the deposition of a marine carbonate bank until Middle Albian times as indicated by stratigraphy recovered from Well B.

Middle Albian–Turonian stratigraphy is dominated by deltaic clastics towards the West African continental margin and shales towards the basin. A lack of faulting during this period of clastic deposition suggests that the change in facies observed across the Mauritanian basin from the Middle Albian is a result of changing conditions of continental clastic production along the West African continental margin.

This indicates that the primary geologic control on the pattern of sedimentary flux to the Mauritanian basin during the post-rift interval to Turonian times was the pre-existing structure of the rift basin, halokenesis, a major Valanginian marine regression and an increase in continental clastic sedimentary production from Middle Albian times. The average solid sediment flux to the Mauritanian basin from 89.0–225 Ma is $0.15^{+0.15}_{-0.13} \times 10^3$ km^3 Ma^{-1} (Table 3).

70.4 – 89.0 Ma

The total thickness of solid sedimentary rock deposited to the study area between the seismic marker horizons 70.4 Ma and 89.0 Ma is shown on Figure 11E and consists exclusively of clastic material. During this interval, < 2 km of clastic sedimentary rock was deposited predominantly in the northern and southern portions of the Mauritanian basin. The centre of the basin is characterised by low solid sedimentary thickness, however small regions of clastic

sediment accumulation correspond to localised salt basins along the eastern margin of the Mauritanian basin. Normal faults in this interval are visible in the seismic data (e.g. Figure 6 and 7), indicating that accommodation was created during the Late Cretaceous. A renewed phase of subsidence in many of Africa's northwest-southeast striking basins is observed from Campanian-Maastrichtian times and has been attributed to the reactivation of underlying basement rift structures (Benkhelil, 1989; Guiraud, 1993; Janssen et al., 1995). The causes of subsidence in the Mauritanian basin are discussed in Chapter 3. Solid sedimentary flux to the Mauritanian basin during the Late Cretaceous appears to be controlled by the creation of accommodation due to basin reactivation and subsidence due to halokenitic movements. The average solid sedimentary flux from 70.4–89.0 Ma is $0.41^{+0.21}_{-0.18} \times 10^3$ km^3 Ma^{-1} (Table 3).

58.4 – 70.4 Ma

The total thickness of solid sedimentary rock deposited to the study area between the seismic horizons 58.4 Ma and 70.4 Ma is shown on Figure 11D and consists predominantly of clastic material. This interval is characterised by low solid sedimentary flux, whereby thicknesses of < 300 m of solid sediment was deposited to an area covering over 90% of the Mauritanian basin. Small regions of high solid sedimentary thickness correspond to areas affected by faulting due to halokinetic movements in the Mauritanian basin along the continental margin and this appears to be the primary geologic control on the solid sedimentary flux to the Mauritanian basin during this interval. The average solid sedimentary flux from 58.4–70.4 Ma is $0.25^{+0.21}_{-0.17} \times 10^3$ km^3 Ma^{-1} (Table 3).

23.8 – 58.4 Ma

The total thickness of solid sedimentary rock deposited to the study area between the seismic horizons 23.8 Ma and 58.4 Ma is shown on Figure 11C. A major change in facies is observed across the entire basin during this interval, whereby Eocene–Oligocene stratigraphy is dominated by carbonate reef deposits in proximal regions and by mixed carbonate/clastic sediment in distal regions of the Mauritanian basin. Up to 2 km of solid sediment was deposited

in the northern portion of the Mauritanian basin during this interval. Oligocene stratigraphy is recovered from Wells G and H, however is absent from all other wells used in this study. The biostratigraphically constrained seismic horizon, 45.7 Ma is identified at Well D (Table **??**). At Well D, this horizon intercepts the overlying unconformity, 23.8 Ma whereby the two events become indistinguishable on seismic data (Figure 6C). Estimates of solid sedimentary flux must represent a minimum due to the effects of sediment removal from eroison during this period. The mapping of dated and regionally correlated relict lateritic landforms across Sub-Saharan West Africa by Grimaud et al. (2018) was used to calculate continental denudation rates and offshore clastic sediment fluxes. Low continental denudation rates characterise West Africa during this period and solid sedimentary flux estimates to the Senegambia catchment to the south of the study area are close to the values calculated for the Mauritanian basin (Figure 12). Results indicate that the primary geologic control on the solid sedimentary flux to the Mauritanian basin from 23.8–58.4 Ma is a lack of continental clastic supply, which allowed the growth of carbonate reefs. Erosional events as recorded by well and seismic data have removed Oligocene stratigraphy from the centre of the basin, meaning that calculated solid sedimentary fluxes must be minimum estimates. The average solid sedimentary flux from 23.8–58.4 Ma is $0.16^{+0.18}_{-0.11} \times 10^3$ km^3 Ma^{-1} (Table 3).

2.5.1 5.6 – 23.8 Ma

The total thickness of solid sedimentary rock deposited to the study area between the seismic horizons 5.6 Ma and 23.8 Ma is shown on Figure 11B. A major change from carbonate to clastic sedimentation is observed across the Mauritanian basin at 23.8 Ma. The horizon, 23.8 Ma is clearly identified as a prominent acoustic impedance anomaly that extends across the entire basin (Figure 6 & 7) and marks a significant regional event. This surface is irregular, undulating and cuts into underlying stratigraphy. This marker horizon is easily identified in seismic data across the basin, except at the Well D, where this horizon becomes indistinguishable with the Eocene horizon, 45.7 Ma (Figure 6C–D). At this location, 21.5 Ma of Middle Eocene–Oligocene stratigraphy has been removed (Figure 10). There is no evidence of halokinetic movement from

23.8 Ma, and in several locations along the West African continental margin this undulating surface cuts into the tops of salt diapirs. The 23.8 Ma horizon is interpreted to represent a major regional erosive event.

Up to 2 km of solid sediment was deposited in a small $\sim 500 \times 500$ km region in the centre of the basin (Figure 11) between 5.6–23.8 Ma. The north, south and distal parts of the Mauritanian basin are characterised by low sedimentary flux during this period. An increase in onshore denudation rates is calculated by Grimaud et al. (2018), who also observe a similar increase in clastic sedimentary flux deposited to the Senegambia catchment (Figure 12). Increased rates of continental uplift during this period are documented across Africa (discussed in Chapters 1 and 4). In order to explain the observed increase of clastic solid sedimentary flux to the centre of the Mauritanian basin during Miocene times, both the creation accommodation offshore and production of clastic sediments due to erosion onshore must have occurred concomitantly. The processes responsible for this must provide the primary geological control on the solid sedimentary flux to the Mauritanian basin during Miocene times. The average solid sedimentary flux to the Mauritanian basin from 23.8–5.6 Ma is $0.20^{+0.20}_{-0.10} \times 10^3$ km^3 Ma^{-1} (Table 3).

0 – 5.6 Ma

The total thickness of solid sedimentary rock deposited to the study area between the seismic horizons 5.6 Ma and 0 Ma is shown on Figure 11A. Up to 2 km of clastic sediment was deposited across the Mauritanian basin during this interval, marking a significant change in conditions across the basin. The horizon, 5.6 Ma is visible across the entire basin (Figures 6 & 7). In proximal parts of the basin, the horizons 5.6 Ma and 23.8 Ma are separated by < 1200 ms, however this decreases significantly in distal parts of the basin where the two horizons become very closely spaced. The horizon, 5.6 Ma, does not cut into underlying stratigraphy or the 23.8 Ma event in any part of the basin. Hence, this horizon is interpreted as a stratigraphic surface and not an erosional event or unconformity.

An order of magnitude increase in clastic solid sedimentary flux across the entire Mauritanian basin at rates of $1.9^{+2.0}_{-1.4}$ ^{3} km^3 Ma^{-1} occurs between 5.6–0

Ma (Table 3). For this to occur, both the rate of creation of accommodation and production of continental clastic sediments onshore West Africa must have increased significantly. The observed pattern of increasing Miocene–Recent clastic solid sedimentary flux to the Mauritanian basin is similar to that observed in other nearby depositional systems such as the Senegambia catchment (Figure 12, Grimaud et al., 2018).

Time [Ma]	Rate	Error
0–5.6	1.90	+2.00/-1.40
5.6–23.8	0.20	+0.20/-0.10
23.8–58.4	0.16	+0.18/-0.11
58.4–70.4	0.25	+0.21/-0.17
70.4–89.0	0.41	+0.21/-0.18
89.0–225	0.51	+0.15/-0.13

Table 3: **Solid sedimentary flux of the Mauritanian basin**. Solid flux was calculated using isopach volumes between seismic intervals mapped across the basin (Figure 6 & 6). Rate and its uncertainty have units of $\times 10^3$ km^3 Ma^{-1}. Errors for solid sedimentary flux are calculated by propagating compaction parametrisation uncertainties. A tentative age of ~225 Ma is assigned to the basement, based on the age of Gondwana breakup (see e.g. Brownfield and Charpentier, 2003; Davison, 2005; Vear, 2005).

2.6 Distribution of sedimentary rock in the Mauritanian basin

2.7 Conclusions

Isopach mapping, depth conversion and decompaction indicate that solid sedimentary flux decreases from $0.41^{+0.21}_{-0.18} \times 10^3$ km^3 Ma^{-1} during the Cretaceous, to Paleocene rates of $0.25^{+0.21}_{-0.17} \times 10^3$ km^3 Ma^{-1} and Oligocene rates of $0.16^{+0.18}_{-0.11} \times 10^3$ km^3 Ma^{-1}. Uncertainties were calculated by propagating errors in compaction parameters. Note that these values include carbonate that has been produced in situ. Volumes of mapped carbonate indicate that Eocene-Oligocene clastic flux is approximately a factor of two smaller than these values. The distribution

of sedimentary rock varies significantly with time. Late Cretaceous deposition (Figure 11E) is concentrated at the northern and southern parts of the basin and was followed by low Paleocene rates of deposition across the basin (Figure 11D). Eocene–Oligocene deposition was concentrated in the northern part of the basin.

1.5 km of clastic rock deposited between 23.8–5.6 Ma in the centre of the basin indicates that the base Miocene unconformity, 23.8 Ma, marks a major change in sedimentation. The top Miocene unconformity, 5.6 Ma, marks a second significant change in post-Miocene sedimentation when < 2 km of sediment was deposited across most of the basin. Solid clastic sedimentary fluxes for the Miocene and post-Miocene are $0.2^{+0.20}_{-0.10} \times 10^3$ km^3 Ma^{-1} and $1.9^{+2.00}_{-1.40} \times 10^3$ km^3 Ma^{-1}, respectively. Whilst the overall solid sedimentary flux during the Eocene-Oligocene is similar to that of the Miocene, it is important to note that the majority of Miocene sedimentation is restricted to a small region in the centre of the basin adjacent to the Senegal river (Figure 11B). I note that these estimates of sedimentary flux are likely to be under-estimates because I do not consider material that has gone into solution. The solid sedimentary flux of the Mauritanian basin is similar to that measured from the erosion history of lateritic horizons in the Sene-Gambia system adjacent to the Fouta-Djallon swell south of the study area (Grimaud et al., 2018; Figure 12).

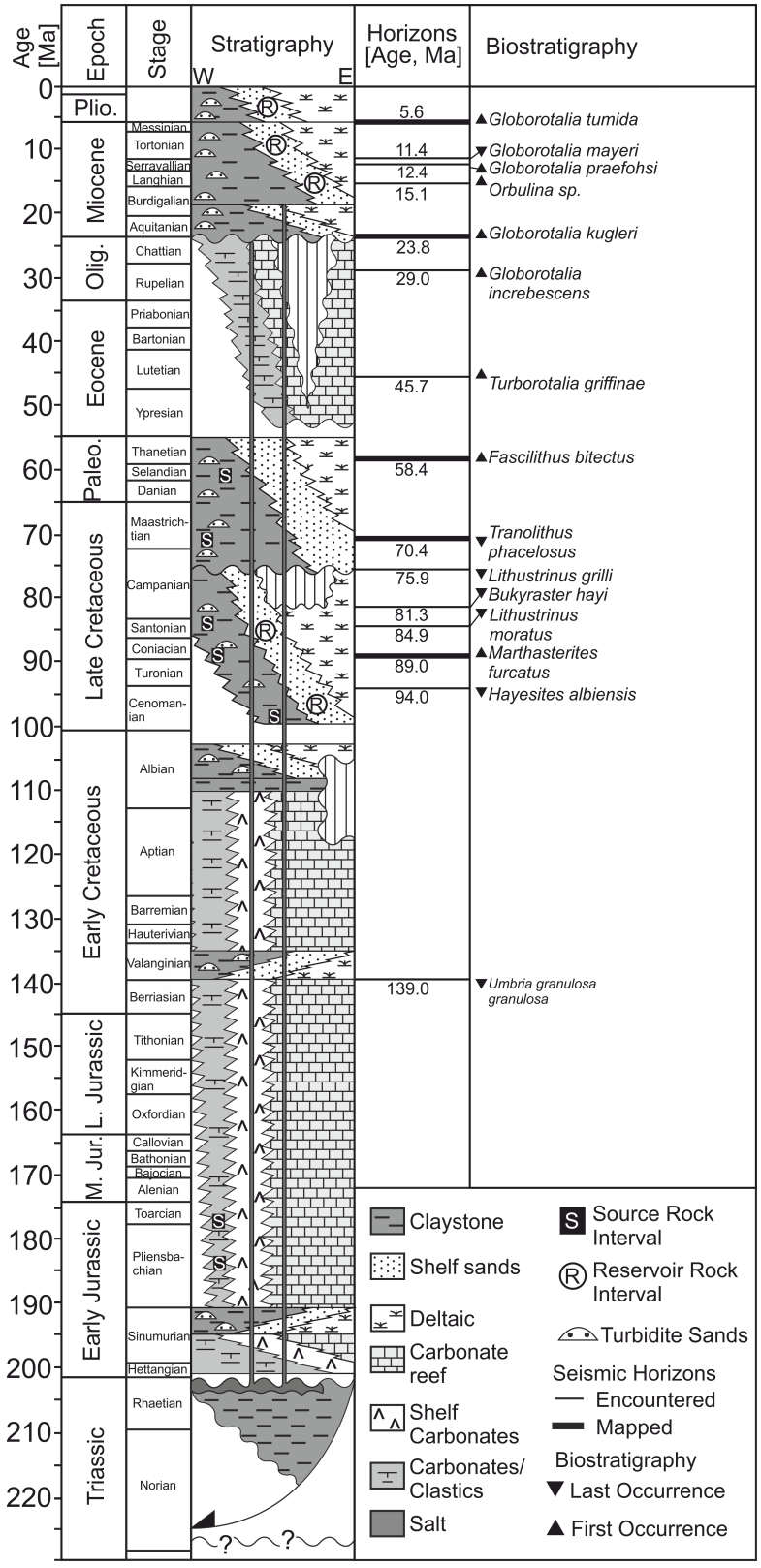


Figure 10: **Mauritanian chrono- and biostratigraphy**. Up/down arrows = first/last occurrences of planktonic foraminifera, calcareous nannofossils and palynofossils used to constrain ages of seismic horizons across the Mauritanian margin.

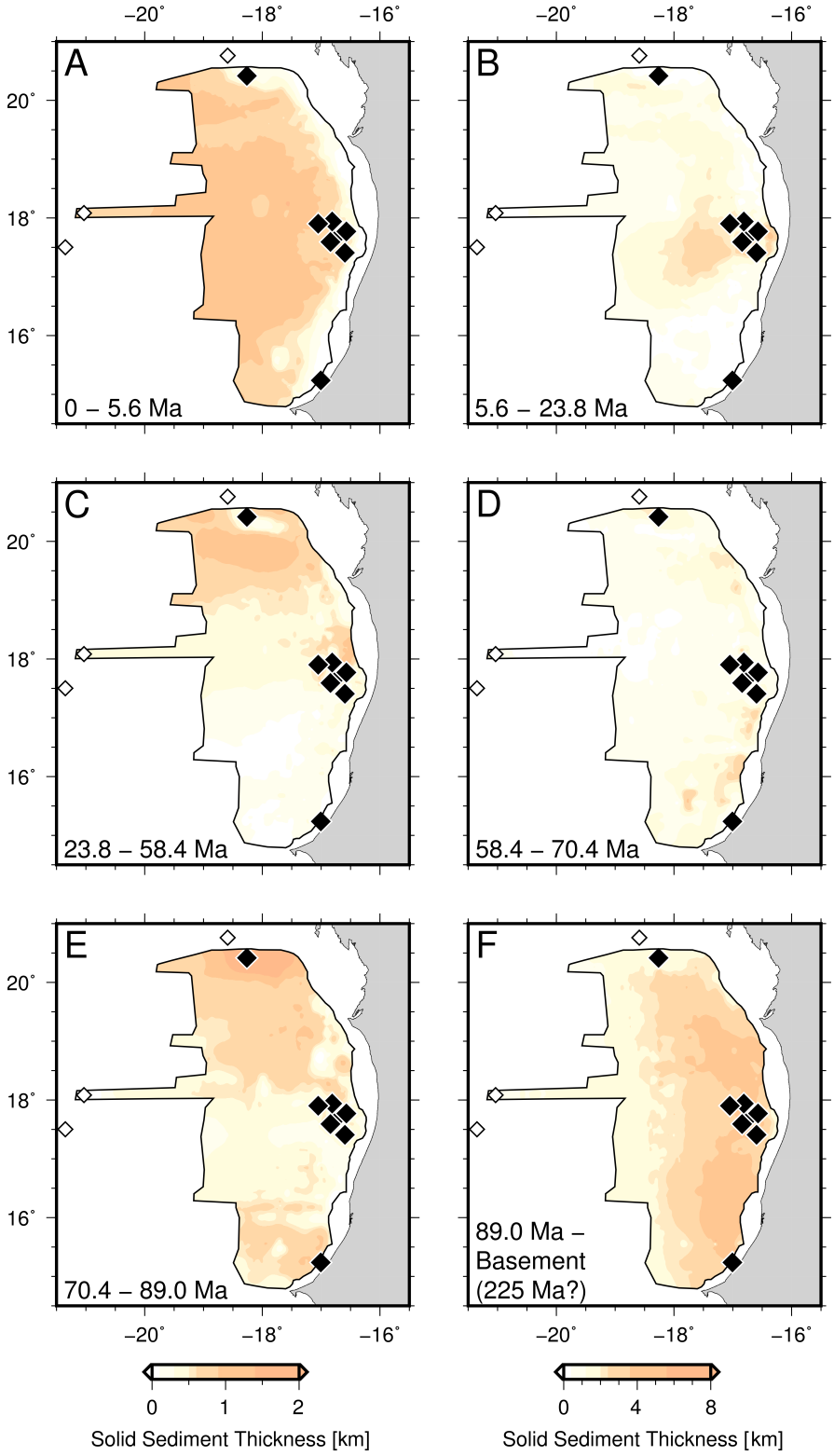

A
0 – 5.6 Ma
B
5.6 – 23.8 Ma
C
23.8 – 58.4 Ma
D
58.4 – 70.4 Ma
E
70.4 – 89.0 Ma
F
89.0 Ma –
Basement
(225 Ma?)
−20˚
−18˚
−16˚
20˚
18˚
16˚
0
1
2
Solid Sediment Thickness [km]
0
4
8
Solid Sediment Thickness [km]

Figure 11: **Solid sedimentary thickness of the Mauritanian basin**. (A-E) Isopach thickness maps for intervals between seismic horizons identified in the Mauritanian basin (Figures 6, 7 & 5). Black diamonds = wells from this study, white diamonds = DSDP/ODP wells, black polygon = boundary of seismic dataset. (F) Isopach thickness map for the interval between the acoustic basement (∼225 Ma) and 89 Ma. Note that panel F has a colour scale with a larger range than panels A-E.

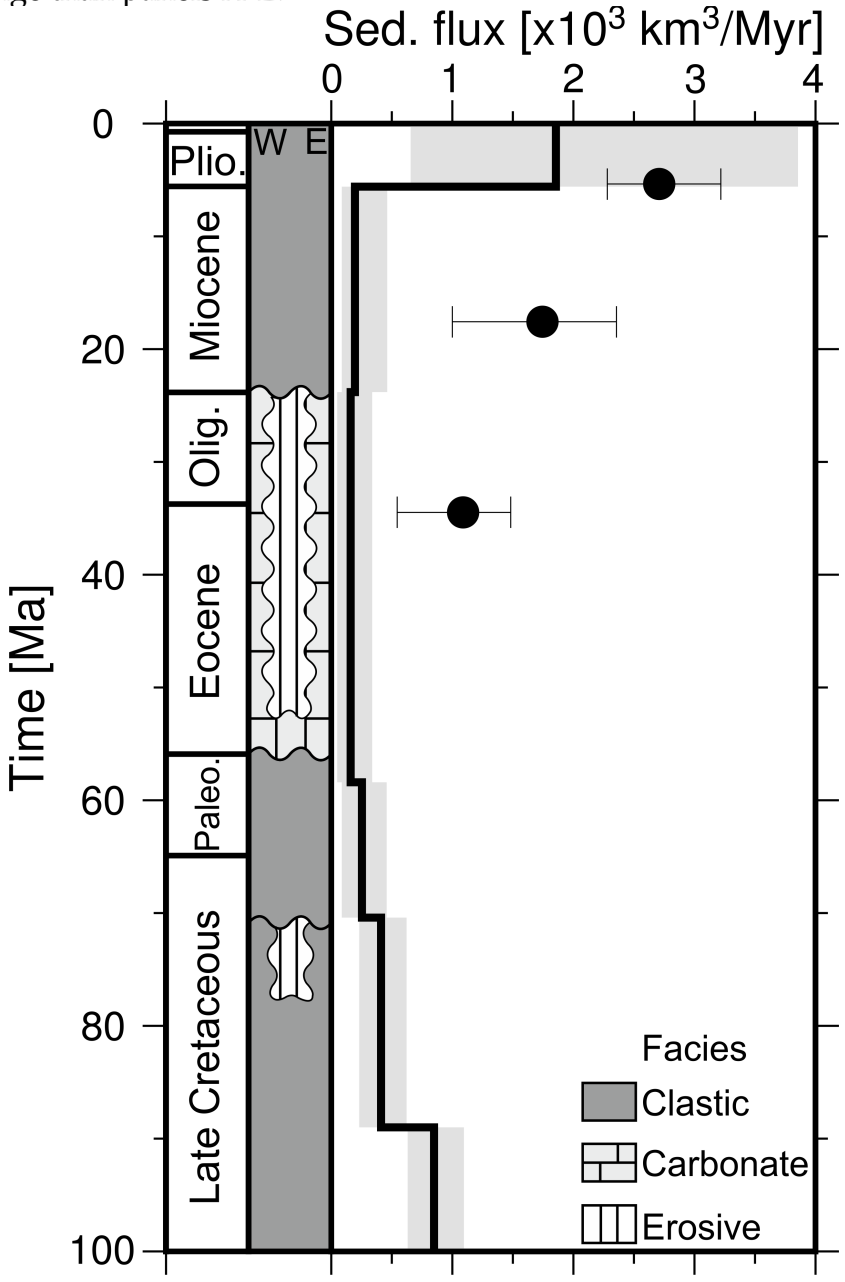


Figure 12: **Mauritanian sedimentary flux**. Grey polygon = uncertainties calculated from compaction parameters (see Table 3). Simplified Mauritanian chronostratigraphy shown on left hand side, please see Figure 10. Black circles with error bars = sedimentary flux of Senegambia calculated from estimates of denudation in sub-Saharan West Africa (Grimaud et al., 2018).

2.8 Prelude to next chapter

The history of solid sedimentary flux to the Mauritanian basin is surprising considering that it lies on a passive continental margin that has remained relatively tectonically stable since the Triassic. Miocene–Recent aged sediment present in the Mauritanian basin is concentrated near the shelf edge (East), and forms a wedge-like geometry. A lack of progradation is clearly visible in the seismic data (Figures 6 & 7). The accumulation of ~ 2 km of sediments from Miocene–Recent times is only possible if both accommodation in the basin was created during these times and there was a sufficient supply of sediment from continental sources. A significant amount of rapid Neogene–Recent tectonic subsidence must have occurred across the Mauritanian basin to create the accommodation required to capture the sedimentary volumes deposited during these times. However, the subsidence history of the Mauritanian basin remains ambiguous and is poorly is understood. Possible causes of localised subsidence in the Mauritanian basin include flexural loading of the lithosphere due to emplacement of the Cape Verde Volcanic Load, salt withdrawal, thin-skinned tectonics or glacio-eustasy. In the following chapter, I constrain the history of tectonic movement of the lithosphere in the Mauritanian basin by calculating the water-loaded subsidence history from Late Cretaceous–Recent times, and explore the origins of the observed subsidence using a newly developed framework for shallow mantle convection beneath the basin.

Chapter 3

Shallow mantle convection beneath the Mauritanian basin

The work presented in this chapter is based on Lodhia et al. (2018).

3.1 Introduction

Tomographic studies, magmatic histories and mantle flow models suggest that variations in mantle temperature, lithospheric thickness and plate motion play an important role in generating shallow mantle convection (e.g. Pekeris, 1935; McKenzie et al., 1974; King and Ritsema, 2000; Moucha and Forte, 2011; Davies and Rawlinson, 2014; Barnett-Moore et al., 2017; Hoggard et al., 2017; Müller et al., 2017). Constraining scales and evolution of sub-plate support and its expression at the Earth's surface, particularly at passive margins, has important implications for interpretation of stratigraphy, heat flow, glacio-eustasy and for parametrising models of mantle convection (e.g. Courtney and White, 1986; Hartley and Allen, 1994; Flament et al., 2013). I combine seismic reflection and well data along the West African margin with shear wave tomography and the uplift and magmatic history of the Cape Verde Rise to constrain thermal, spatial and temporal scales of upper mantle convection.

It is generally accepted that the mantle beneath the African plate supports short ($\sim 10^3$ km) wavelength swells and basins (e.g. Holmes, 1965; Nyblade

and Robinson, 1994; Burke, 1996; Crosby and Whipple, 2006; Burke and Gunnell, 2008; Al-Hajri et al., 2009; Jones et al., 2012). Some swells are magmatic (e.g. Afar, Hoggar, Tibesti, Cape Verde), others are amagmatic (e.g. Bié, Fouta Djallon), most have positive free-air gravity anomalies (Figure 2B), sit atop slow upper mantle shear-wave velocity anomalies and those intersecting oceanic lithosphere have residual bathymetry of up to $+2$ km (e.g. Courtney and White, 1986; Lithgow-Bertelloni and Silver, 1998; Pim et al., 2008; Fishwick, 2010; Ramalho et al., 2010; Jones et al., 2012; Ritsema et al., 2011; French et al., 2013; Priestley and McKenzie, 2013; Schaeffer and Lebedev, 2013; Hoggard et al., 2017, Figure 2B). Drainage networks splay radially from many domal swells suggesting sub-plate support exerts an important control on geomorphology (Paul et al., 2014). In contrast, negative free-air gravity anomalies and ocean-age depth residuals, subsidence patterns and anomalously fast upper mantle shear-wave velocity anomalies indicate that some parts of the continent (e.g. Congo basin) are convectively drawn down (e.g. Crosby et al., 2010; Jones et al., 2012; Hoggard et al., 2017). These observations show that mantle convection plays an important role in determining vertical motions of African lithosphere.

Continental uplift histories provide information about the timescale of positive sub-plate support. For example, laterites and lateritic gravels indicate that pre-Oligocene topographic gradients in West Africa were low (e.g. Burke and Gunnell, 2008; Chardon et al., 2016). The broadly coeval growth of carbonate reefs on deltas fringing the African continent imply low rates of clastic efflux until $\sim$ 23 Ma (e.g. Walford et al., 2005; Paul et al., 2014). Uplifted marine terraces, over-compacted stratigraphy, sedimentary flux histories and magmatism indicate post-Oligocene epeirogeny occurred in Africa (e.g. Partridge and Maud, 1987; Walford et al., 2005; Al-Hajri et al., 2009; Guiraud et al., 2010). Uplift rate histories calculated by inverting drainage networks indicate that post-35 Ma, uplift of topographic swells was diachronous and staged (Paul et al., 2014; Rudge et al., 2015). This work suggests that the landscapes of the African continent are largely Neogene in age and are a result of changing patterns of sub-plate support. If upwelling mantle generated regional uplift, it may be expected that downwelling mantle generated broadly coeval regional subsidence patterns.

In this chapter, the history of sub-plate support beneath the West African margin was examined where hitherto ambiguous Neogene–Recent subsidence histories contain important information about thermal and spatial scales of convective drawdown. The structure of modern lithosphere and the upper mantle using a newly updated shear wave tomographic model and gravity data was determined. Results indicate that uplift and magmatism of the Cape Verde Rise is broadly coeval with rapid Neogene–Recent subsidence of the Mauritanian margin constrained by well and seismic data. These uplift and subsidence patterns were then combined with temperature and simple isostatic calculations to constrain thermal and spatio-temporal scales of upper mantle convection.

3.2 Data Processing and Methodology

3.2.1 Shear wave velocities

To determine mantle structure, an updated version of the Rayleigh wave African tomography model from Fishwick (2010) is used, which is probably the highest resolution regional tomography model available. The shear-wave velocity structure is derived in a two stage process. The first stage involves inverting waveforms at periods between 50 and 120 s for the fundamental mode and the first four overtones (where present above the noise). The second stage is a series of tomographic inversions to provide a velocity model defined at 25 km depth intervals. The 2010 version of the model was updated to incorporate data from recent deployments, which has more than doubled the path coverage in Africa. For West Africa and it's continental margin, the most significant are the inclusion of data from Mid Atlantic Ridge events recorded on the PICASSO (Levander et al., 2009) and Muenster-Morocco (Thomas, 2010) deployments. These provide a significant improvement in density of path coverage in north-west Africa (see Figure 15). Resolution tests show that velocity perturbations of a few percent at wavelengths ~ 300 km are resolvable beneath Cape Verde and the Mauritanian basin within the uppermost mantle (Figure 14). Figure 14

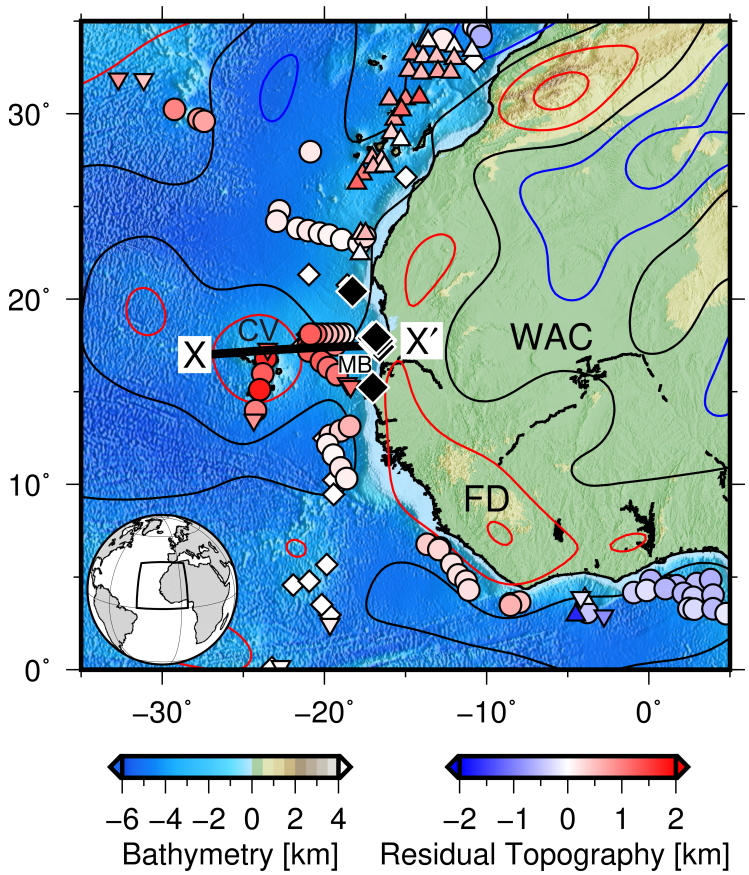


Figure 13: **Bathymetry and residual topography of the West African margin**. Black polygon on inset globe = location. Red/black/blue contours = positive/zero/negative long wavelength (800–2500 km) free-air gravity anomalies from GOCE dataset (Förste et al., 2014); contour interval = 10 mGal. Circles/upward/downward pointing triangles = accurate/minimum/maximum residual ocean-age depth estimates (this study; Hoggard et al., 2017). Black/white diamonds = commercial/IODP-DSDP wells. X—X′ = cross-section shown in Figure 20. CV = Cape Verde Rise, MB = Mauritanian basin, WAC = West African craton and FD = Fouta Djallon swell.

shows slices at 25 km intervals through the shear wave velocity model for West Africa and its surroundings for depths between 75–200 km.

3.2.2 Tomography model

The automated waveform inversion procedure of Debayle (1999) is used as the basis for the first stage of the surface wave tomography. Events with a $M_w > 5.0$ are used to provide a good distribution of sources from the mid-ocean ridges. Waveforms with low signal-to-noise ratios between periods of 50–120 s were

removed from the dataset prior to inversion. Following the same approach as Fishwick (2010), the inversion is performed from four different starting models defining the mantle structure. Only data that produces a coherent final model from these different starting models is used within the tomographic inversion. The data are clustered, and $24,699$ path average velocities are incorporated into the tomographic inversion. The tomography uses spherical B-splines to provide smoothing within the inversion procedure. Following Fishwick (2010), the long wavelength structure is recovered in an initial inversion and then used as a reference for the final inversion with two-degree knot points. Damping (to the reference model) is applied to regularise the inversion.

Path coverage used to constrain the tomographic model is shown in Figure 15. Figure 15C–D shows the difference in path density between the current model and Fishwick (2010) for the region discussed in this study; there are significant increases throughout the whole area. The resolution of the tomographic model was examined at 150 km depth by inverting synthetic data constructed using the checker board velocity model shown in Figure 15E. Path average velocities were calculated using the inventory of African paths shown in Figure 15A and noise with a standard deviation of 0.02 km s^{-1} was added to the synthetic dataset. The standard deviation for the noise was calculated using the standard deviation of the residuals between observed path average velocities and those predicted by the final tomographic model. Figure 15F shows the recovered velocity structure obtained by inverting the noisy synthetic data. Importantly for the purposes of this study, velocity perturbations of a few percent at wavelengths of ~ 300 km are resolvable beneath Cape Verde and the Mauritanian basin. Figure 14 shows the velocity model for West Africa and its surroundings.

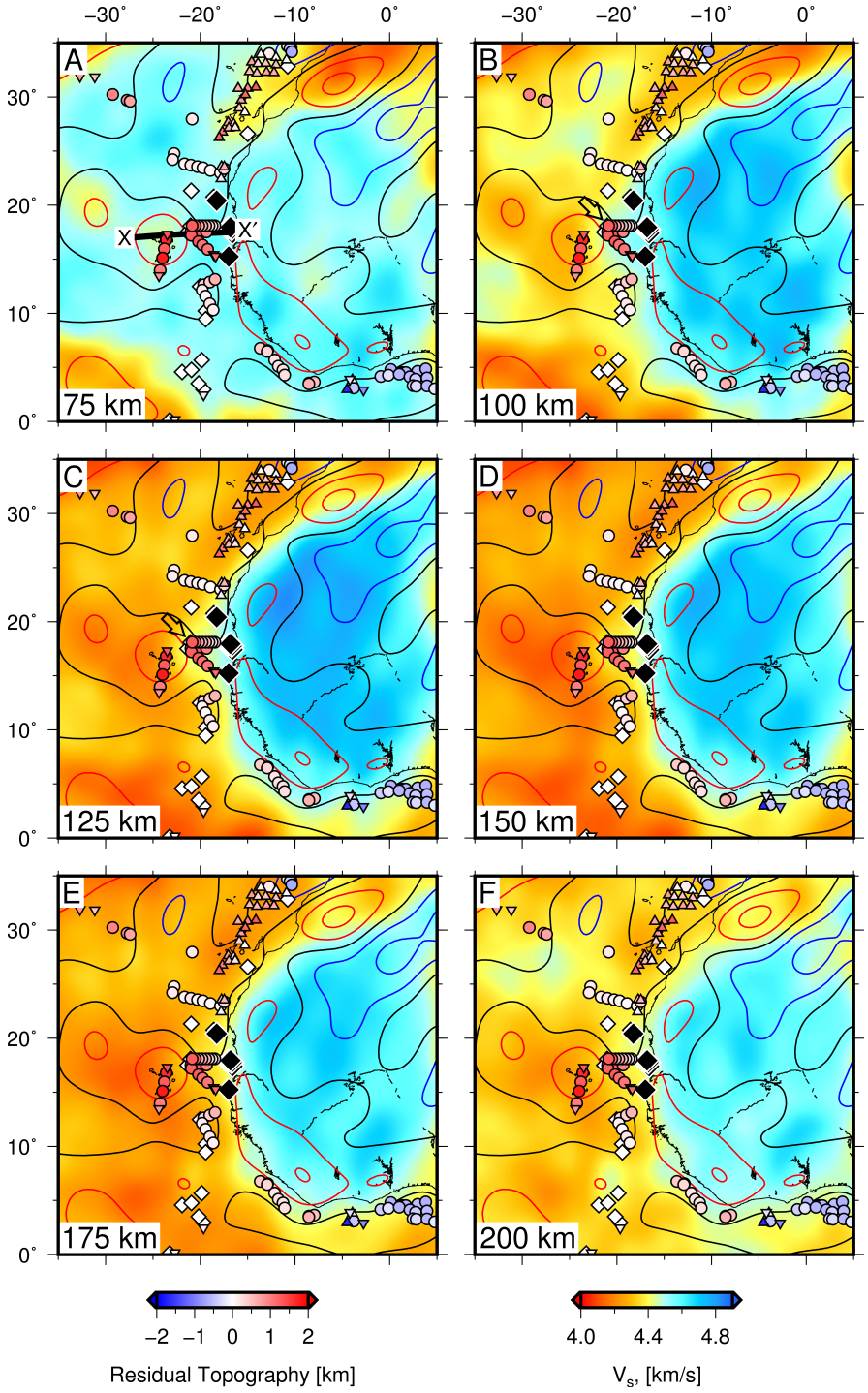


Figure 14: **Shear wave tomography model**. (A–F) Slices through new shear wave tomographic model from 75–200 km depth. Colour scale = absolute shear wave velocities. Note protuberance of fast velocities beneath the Mauritanian basin (arrows in panels B and C).

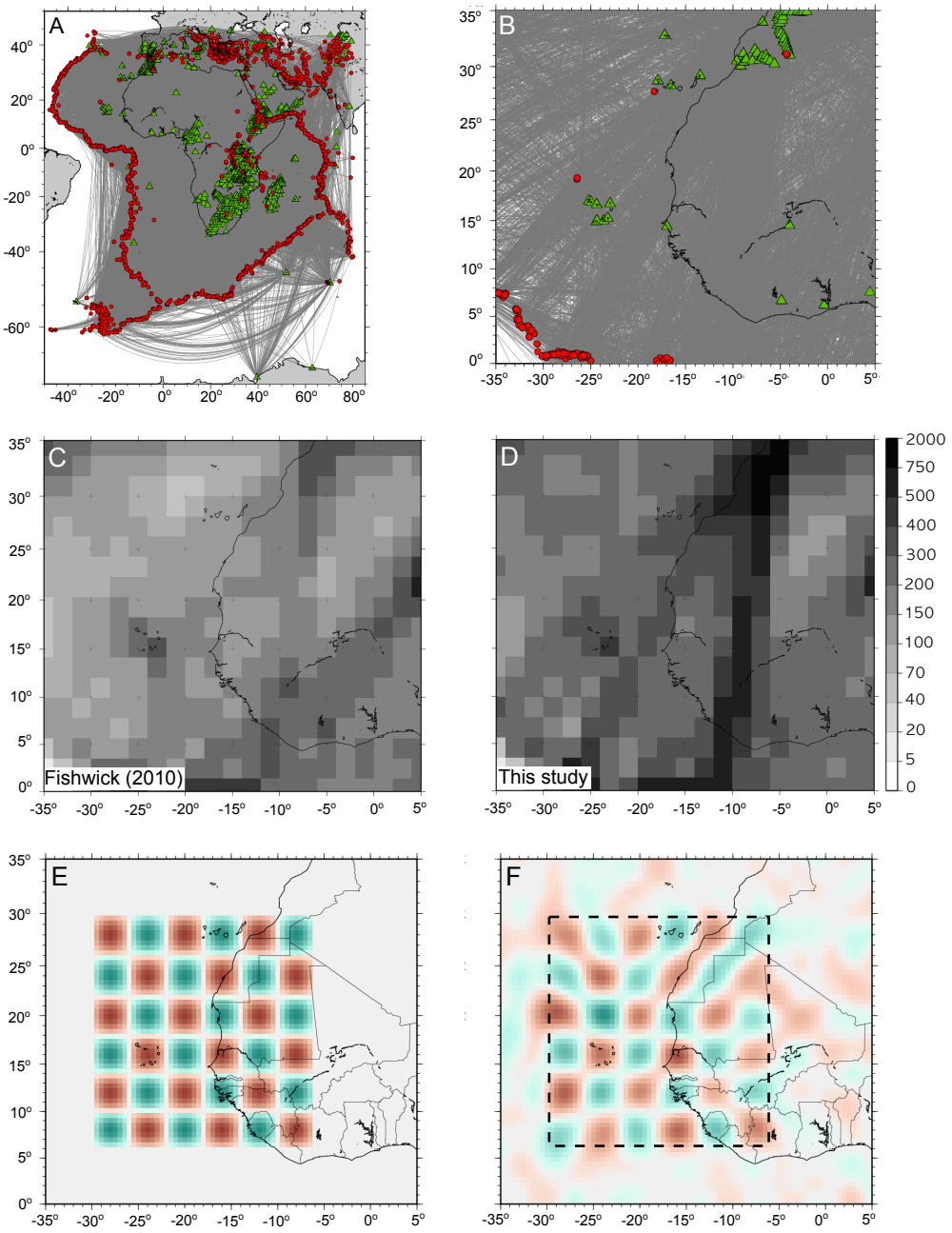


Figure 15: **Path coverage & checkerboard tests**. (A) Path coverage (gray lines), seismic stations (triangles) and events (circles) used to constrain African tomographic model. (B) Coverage across Mauritanian margin. (C–D) Comparison between path coverage in Fishwick (2010) and this study. (E–F) Recovery of synthetic velocity perturbations at 150 km depth. (E) Checkerboard pattern of input velocity perturbations of $\pm 6\%$ at 4° separation. (F) Recovered velocity model from inversion of synthetic data calculated using path coverage shown in panel A and noise commensurate with uncertainties in real data at 150 km depth. Dashed line encloses non-zero synthetic velocity perturbations in input.

3.2.3 Temperature from shear wave velocities

I estimate mantle temperatures from shear waves using three techniques adapted from Priestley and McKenzie (2006, 2013) and Goes et al. (2012).

Priestley & McKenzie (2006)

Priestley and McKenzie (2006)'s approach uses mineral-physics based expressions, but with parameters chosen to reconcile tomographic velocities with thermal constraints from the oceanic plate cooling model and cratonic xenoliths. In their updated conversion they show that parameter values may need to vary depending the global tomographic model used (Priestley and McKenzie, 2013). Equation (5) in Priestley and McKenzie (2006) is used to generate a look-up table of temperatures, T, as a function of pressure, P, and shear wave velocities, V_s. Using Equation 5 from Priestley and McKenzie (2006), I assume that pressure is lithostatic (i.e. $P = \rho g z$, where $\rho = 3300$ kg m^{-3} is density, $g = 9.81$ m s^{-2}, z = depth) to obtain:

$$V_s = [1 + b_v(z - 50)] \left\{ mT + c + A \exp \left[-\frac{E + PV_a}{R(T + 273.15)} \right] \right\}, \qquad (3.1)$$

where $b_v = 3.84 \times 10^{-4}$ km^{-1}, $m = -2.8 \times 10^{-1}$ m s^{-1} ∮C^{-1}, $c = 4720$ m s^{-1}, $A = -1.8 \times 10^{16}$ m s^{-1} are empirically determined constants and T = Temperature in °C. Activation energy $E = 409 \times 10^3$ J mol^{-1}, activation volume $V_a = 10^{-6}$ m^3 mol^{-1} and the gas constant $R = 8.3145$ J mol^{-1} K^{-1}. Solutions to Equation (3.1) can be easily recast to extract $T(P(z), V_s)$.

Priestley & McKenzie (2013)

A modified approach based on McCarthy et al. (2011)'s scaling of seismic wave frequencies, f, by Maxwell relaxation times, τ, is given in Priestley and McKenzie (2013). The Maxwell time scale $t = \eta/\mu$, where η and μ are viscosity and the shear modulus, respectively. A dimensionless frequency is expressed as $f' = f\tau$ and expressions for $V_s(f')$ can then be obtained. Priestley and McKenzie (2013) combine this approach with an empirical parametrisation similar to

that in their 2006 paper. Combining their Equations (4–7), (9), (10) and (12), I obtain:

$$V_s = \sqrt{\rho^{-1}\mu(P,T)F(f')}, \tag{3.2}$$

where

$$\mu(P,T) = \mu_0 + (\partial\mu/\partial T)_P T + (\partial\mu/\partial P)_T P, \tag{3.3}$$

$$F(f') = \begin{cases} \sum_{k=0}^{6} a_k (\ln f')^k & \text{for} \quad f' \leq 10^{13} \\ 1 & \text{for} \quad f' > 10^{13} \end{cases} \tag{3.4}$$

a_k were determined empirically by McCarthy et al. (2011): $a_0 = 0.55097$, $a_1 = 0.054332$, $a_2 = -0.0023615$, $a_3 = -5.7175 \times 10^{-5}$, $a_4 = 9.9473 \times 10^{-6}$, $a_5 = -3.4761 \times 10^{-7}$, $a_6 = 3.9461 \times 10^{-9}$. Seismic frequencies $f = 0.01$ to 0.05 Hz are tested and calculated the dimensionless frequencies using $\tau = \eta/\mu$, where $\eta = \eta_0/a^\star$, $a^\star = \exp[(E + P_r V_a)/RT_r]/\exp[(E + PV_a)/RT]$. Values for the following parameters are from their Table 1: $\mu_0 = 72.66 \times 10^9$ Pa, $\partial\mu/\partial T = -0.871 \times 10^7$ Pa K^{-1}, $\partial\mu/\partial P = 2.04$, $\log_{10}\eta_0 = 22.38\ \log_{10}(\text{Pa s})$, $E = 402.9 \times 10^3$ J mol^{-1}, $V_a = 7.81 \times 10^{-6}$ m^3 mol^{-1}, $R = 8.3145$, $T_r = 1473$ K, $P_r = 1.5 \times 10^9$ Pa. The values used are dependent on the global tomographic model used in the empirical parametrisation. Note that Equations (18)–(22) in their paper can also be used to determine $V_s(P,T)$.

Calculated lithospheric geotherms are similar to those from their 2006 parametrisation. However, calculated sub-lithospheric temperatures are significantly greater. Takei et al. (2014)'s experimental results, which extend the frequency range of McCarthy et al. (2011)'s experiments to incorporate seismic frequencies, indicate that $T(V_s, P)$ determined using Priestley and McKenzie (2013)'s results are probably too high at low wave speeds (see also Richards et al., 2016). For these reasons I use their earlier parametrisation, which yields broadly similar results to Goes et al. (2012)'s approach.

Goes et al. (2012)

The V_s calculation of Goes et al. (2012) combines a thermodynamic calculation of anharmonic velocities with an anelastic correction. Anharmonic velocities and densities are computed for a pyrolitic composition using the code PerPleX (Connolly, 2005) with the mantle database from Xu et al. (2008). PerPleX performs Gibbs free energy minimisation to determine phase composition as a function of pressure and temperature, and the Xu et al. (2008) database provides the relevant activity and solidus solution models and the parameters to compute elastic parameters and density using a 3^{rd} order Birch-Murnaghan equation of state with a Mie-Grüneisen thermal correction. Voigt-Reuss-Hill averaging is used to combine mineral properties. Finally, a correction for anelasticity is applied according to Equation (3.5), yielding V_s as a function of temperature and pressure, major-element composition, X, and frequency such that:

$$V_s(T, P, X, f) = V_{\mathrm{anh}}(T, P, X) \left[1 - \frac{Q_g^{-1}(f, T, P)}{2\tan(\pi\alpha/2)}\right], \tag{3.5}$$

where

$$Q_g(f, T, P) = A_g f^{\alpha_g} \exp\left(\frac{\alpha_g \gamma T_m}{T}\right). \tag{3.6}$$

Ag = 0.1, frequency $f = 0.05$ Hz, $\alpha = 0.15$, $\gamma = 38$, T_m is the dry solidus from Herzberg et al. (2000). This model was used to generate the look-up chart shown in Figure 16B. These and similar attenuation laws have previously yielded lithosphere and shallow mantle temperatures that can reasonably reconcile P and S-velocities, surface heat flow, and attenuation in the shallow mantle below several continental regions (e.g. Goes et al., 2000; Goes, 2002; Hwang et al., 2009), the range of observed seismic velocities as a function of oceanic plate age (Goes et al., 2012), and shear-wave speeds, major-element petrology and bathymetry of mid-ocean ridges (Dalton et al., 2014).

3.2.4 Temperature from shear wave velocities and isostasy

To estimate the thermal state of the mantle beneath West Africa and Cape Verde, the newly updated shear wave model of Fishwick (2010) was converted into temperature. Look-up charts showing temperature as a function of depth and shear wave velocity (V_s) are shown in Figure 16 for Priestley and McKenzie (2006)'s empirical parametrisation and for Goes et al. (2012)'s mineral physics approach. The difference between the two parametrisations is also shown. Calculated temperatures differ by < 200°C for V_s values in this study (i.e. within 0.3 km s^{-1} of AK135: see Figure 16C). Figure 16D–G shows temperature profiles calculated using the two parametrisations beneath Mauritania and the Cape Verde Rise. Solutions to the analytical expressions in Section 2 of Priestley and McKenzie (2013) yield a similar lithospheric geotherm to their 2006 parametrisation. The isostatic support, U, generated by excess asthenospheric temperature, $\overline{T}$, within a layer of thickness h can be calculated using:

$$U = \frac{h\alpha\overline{T}}{1 - \alpha T_\circ}, \tag{3.7}$$

where $T_\circ$ is the background temperature, which I set to 1330°C, and α is the thermal expansion coefficient (Rudge et al., 2008). Note that this calculation is insensitive to assumed background temperature because $\alpha \ll 1$. For example, a 100°C change in background temperature changes calculated uplift by ~ 1 m.

3.2.5 Ocean age-depth residuals

Residual ocean-age depth measurements help identify regions supported by sub-plate processes and can test results obtained using Equation (3.7) (e.g. Richards et al., 2016). The longest seismic line in my inventory extends > 400 km from the West African margin towards the Cape Verde Rise (Figure 6A). The seabed, sediment-basement interface and oceanic Moho are easily identified (Figure 6B). I interpret the prominent intra-crustal impedance contrasts as igneous sills. I use Hoggard et al. (2017)'s sediment and crustal thickness corrections, which incorporate a large amount of seismic data from the Atlantic Ocean, to calculate residual depths from their plate cooling model. Residual depths were measured at the points marked on Figure 6B and are plotted in

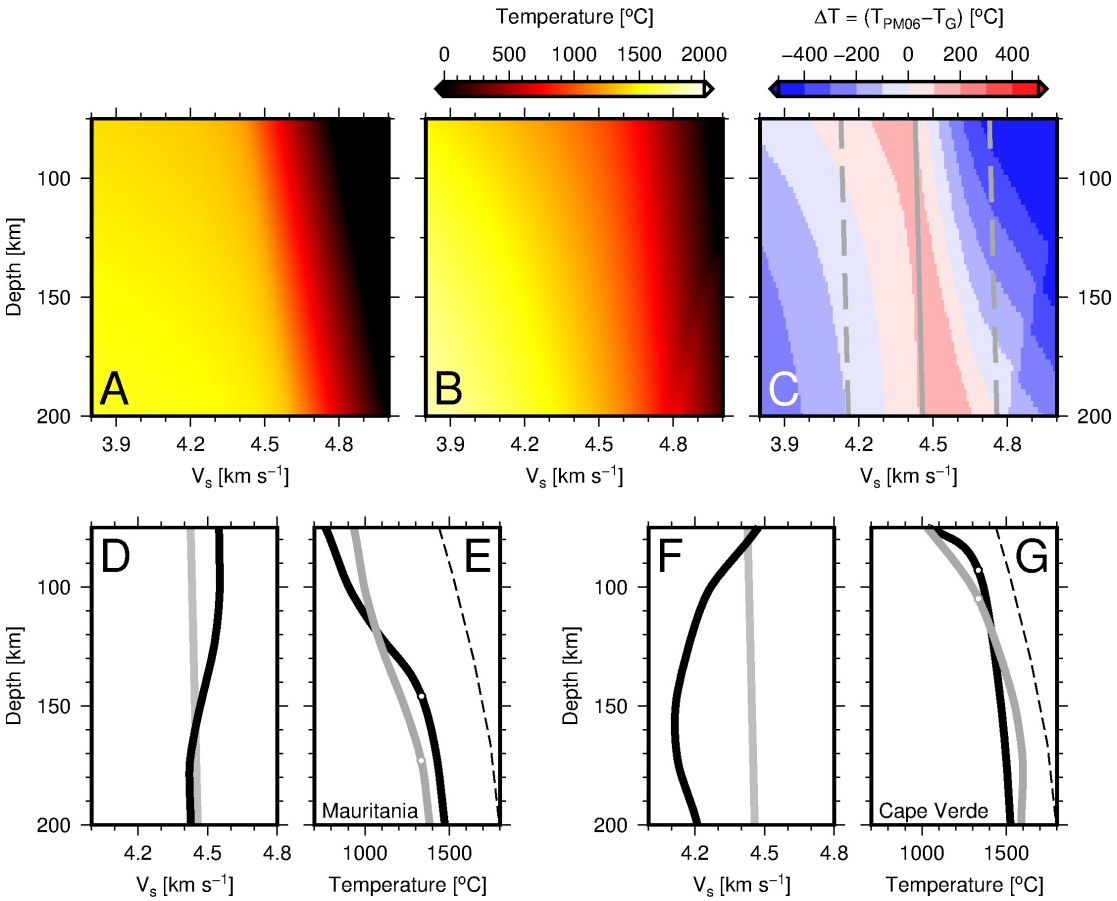


Figure 16: **Shear wave tomography to temperature conversion**. Look-up charts showing temperature as a function of depth and shear wave velocity (V_s) for (A) Priestley and McKenzie (2006)'s empirical parametrisation (T_{PM06}). (B) Goes et al. (2012)'s mineral physics parametrisation with anelastic velocity correction (T_G). (C) Difference between the two parametrisations. Gray line = global average (modified AK135 from Schaeffer and Lebedev, 2013); dashed lines = global average ± 0.3 km s^{-1}. (D) Black curve = absolute shear wave velocities, V_s, beneath Mauritania from new tomographic model. Gray line = global average. (E) V_s converted to temperature as a function of depth using Priestley and McKenzie (2006)'s parametrisation (black line) or the Goes et al. (2012) parametrisation corrected for anelasticity (gray line). Circles = $1330°$C used to map lithosphere-asthenosphere boundary (see Figure 20). Dashed line = dry peridotite solidus (Fitton et al., 1991). (F–G) Velocities and calculated temperatures beneath the Cape Verde Rise.

Figure 13 along with Hoggard et al. (2017)'s compilation. These values are compared to estimates of dynamic topography calculated using long wavelength (800–2500 km) components of the EIGEN6c GOCE gravity field and an admittance of 35 ± 10 mGal km^{-1} (Figure 13, Förste et al., 2014; Hoggard et al., 2017).

3.3 Subsidence history

3.3.1 Extrapolations of seismic horizons

A regional time-depth relationship that best-fits the mean time-depth pairs of all check-shot data from wells used in this study ($\phi_\circ = 0.75 \pm 0.1$, $\lambda = 2.66 \pm 1.2$ km) was used to convert seismic marker horizons mapped in two-way time to depth across the entire Mauritanian basin as described in Chapter 2.3. However, to determine the subsidence history of each well in this study, values for the depths of seismic marker horizons which were not penetrated beneath shallow wells must be determined.

Figure 17 shows the ages and depths of stratigraphic horizons penetrated by each well and the range of depth values to seismic marker horizons calculated using the mean time-depth relationship, μ, upper and lower error bounds (one standard deviation above and below the mean, $\pm\sigma$). To calculate the depths of seismic marker horizons which were not penetrated by shallow wells, the appropriate best-fitting time-depth relationship (μ, $+\sigma$ or $-\sigma$) was used for each well. Across all wells, measured stratigraphic depths match closely with either the μ, $+\sigma$ or $-\sigma$ velocity model, justifying such an approach.

3.3.2 Backstripping for subsidence histories

The subsidence history of the Mauritanian basin was calculated by backstripping the eight wells in my inventory. Using the methodology described in Chapter 2, the water-loaded subsidence is calculated by assuming a fixed sea level for each well and using a simple isostatic calculation:

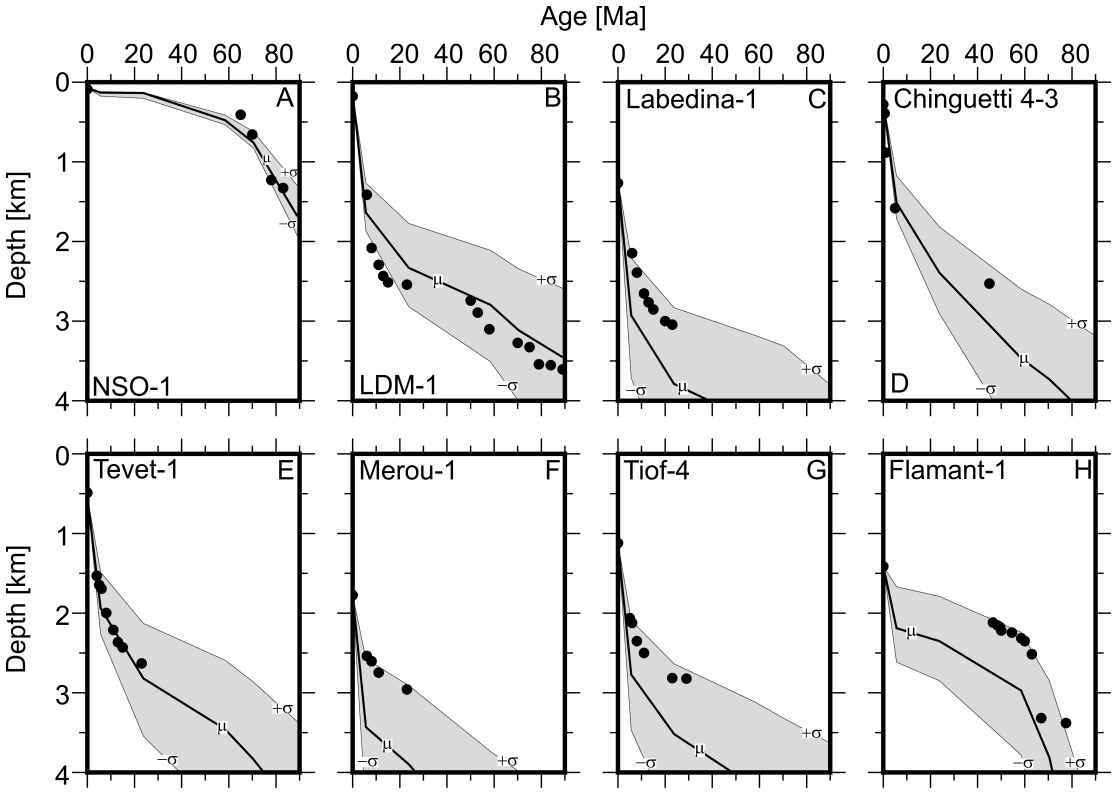


Figure 17: **Age–depth curves of Mauritanian wells**. (A-H) Depths of stratigraphy penetrated by each well and time-depth relationships used to extrapolate deep stratigraphy. Black circles = depths of stratigraphic horizons penetrated by each well; thick black line = mean (μ) time-depth relationship; thin black lines = upper and lower error bounds ($\pm\sigma$ time-depth relationships as labelled); grey regions = region of uncertainty.

$$S_w = S_s \left(\frac{\rho_a - \rho_s}{\rho_a - \rho_w} \right) + W_d, \tag{3.8}$$

where water loaded subsidence, S_w, is expressed as a function of sediment-loaded subsidence, S_s (Sclater and Christie, 1980). Asthenospheric density, $\rho_a = 3200$ kg m^{-3}, sediment density, ρ_s = 2400 kg m^{-3}, and density of water, ρ_w = 1000 kg m^{-3}. I apply palaeo-water depth corrections, W_d, based on benthonic biofacies (e.g foraminifera assemblages) documented in well reports. Table **??** summarises the palaeo-water depth corrections, which are consistent with Vear (2005). Water-loaded subsidence and chronostratigraphy for all wells are shown in Figure 18.

3.3.3 Theoretical thermal subsidence

Measured subsidence patterns are compared to theoretical post-rift (i.e. thermal) subsidence. The thermal subsidence curves, $S_t(t)$ in Figure 18 were produced using:

$$S_t = E_\circ r \left[1 - \exp\left(-\frac{t}{\tau}\right)\right], \tag{3.9}$$

where

$$E_\circ = \frac{4l\rho_m \alpha T}{\pi^2(\rho_m - \rho_w)}, \qquad r = \frac{\beta}{\pi}\sin\left(\frac{\pi}{\beta}\right). \tag{3.10}$$

Parameters and their values are as follows, t = time, τ = thermal time constant = $l^2/\pi^2\kappa$, where l = lithospheric thickness (125 km), thermal diffusivity, κ = 10^6 m^2 s^{-1}. Mantle density, ρ_m = 3300 kg m^{-3}, $\alpha = 3.3 \times 10^{-5}/^\circ$C, and temperature of the asthenosphere = 1330°C (Fowler, 2006). The end of rifting (i.e. $t = 0$) is assumed to have occurred at 170 Ma (Vear, 2005). The best-fitting post-Cretaceous (< 65 Ma) stretching factors, β, are annotated in Figure 18.

3.4 Results

3.4.1 Tomography

The Mauritanian margin sits between the Cape Verde swell and the West African Craton. The Cape Verde swell is underlain by slow mantle ($V_s < 4.4$ km s^{-1}) between 75 and 200 km depth (Figure 14). A protuberance of fast velocities ($V_s > 4.4$ km s^{-1}) extends from the West African Craton beneath the Mauritanian margin between ~ 100–150 km depth (Figure 14). This protuberance extends beneath the stretched lithosphere of the West African margin, and is located beneath the central portion of the Mauritanian basin (the region covered by the wells used in this study). Two receiver function studies from Cape Verde have shear wave velocities that differ by > 0.5 km s^{-1} at depths < 100 km, which makes them difficult to interpret (cf. Lodge and Helffrich, 2006; Vinnik et al., 2012). Vinnik et al. (2012)'s study indicates that shear wave velocities are up to 0.4 km s^{-1} slower than AK135 at depths of 100–200 km,

which is broadly similar to the velocity structure in the regional tomographic model presented here.

3.4.2 Temperature from shear wave velocities

The 1330°C isotherm calculated using Priestley and McKenzie (2006)'s and Goes et al. (2012)'s parametrisations is at a depth of 90–105 km beneath Cape Verde and 145–175 km beneath the Mauritanian basin (Figure 20C). Conversion of shear wave velocities into temperature yield average values of 1486 ± 26°C and 1248 ± 34°C for a 100–200 km deep layer beneath the Cape Verde Rise and Mauritanian basin, respectively. The uncertainties in calculated temperatures encapsulate the range of values determined from the Priestley and McKenzie (2006) and Goes et al. (2012) parametrisations. Uncertainties in temperatures from V_s based on uncertainties in experimental elastic and anelastic parameter values have been estimated to be about 50°C (Cammarano et al., 2003). Using a simple isostatic relationship between excess temperature of the layer and uplift yields $+643 \pm 88$ m for the Cape Verde Rise and -180 ± 114 m for the Mauritanian basin (Equation 3.7). Calculated temperature (and isostatic support) depends strongly on the data distribution and inversion method used to derive the shear velocity model. For example, isostatic support of Cape Verde and the Mauritanian basin calculated using Schaeffer and Lebedev (2013)'s shear wave model are $+466 \pm 20$ m and -827 ± 16 m, respectively. These calculations indicate that a change in sub-plate support of order $+10^3$ m to -10^3 m exists from Cape Verde to West Africa.

3.4.3 Ocean age-depth

Residual ocean-age depths decrease from $+1.5 \pm 0.5$ km on the Cape Verde Rise eastward to 0 km where oceanic lithosphere abuts the Mauritanian margin (Figure 13). These observations are consistent with Courtney and White (1986)'s heat flow anomalies, which decrease to normal oceanic values from $+16 \pm 4$ mW m^{-2} at the centre of rise. The change in residual depth anomalies is coincident with an increase in shear wave speeds from < 4.2 km s^{-1} beneath

the Cape Verde Rise to > 4.4 km s^{-1} beneath the Mauritanian basin (Figure 14B–C).

3.4.4 Stratigraphy and subsidence

There is at least 8 km of Cenozoic and Mesozoic sedimentary rock in the Mauritanian basin. Paleocene-Eocene stratigraphy is characterised by low rates of clastic deposition. Apart from the northernmost part of the study area, Eocene to Late Oligocene stratigraphy is dominated by extensive carbonate deposition. Proximal sedimentary rock has been eroded, which was probably caused by Oligocene-Neogene uplift and erosion of continental topography (e.g. Rudge et al., 2015; Chardon et al., 2016). This denudation is most clearly expressed at well Chinguetti 4-3 where Early Miocene stratigraphy (~ 23 Ma) is underlain by a prominent unconformity that marks a significant change from carbonate to clastic input (Figure 6). Foraminiferal assemblages indicate that Cenozoic palaeo-water depth was neritic (0–150 m) at proximal wells and middle bathyal (500–2000 m) at distal wells (Table **??**; Figure 18; Lekie and Olson, 2003; Vear, 2005; Immenhauser, 2009). The foraminiferal data indicate that dramatic Cenozoic changes in water depth did not occur, which could be a result of high Neogene sedimentation rates and the post-rift setting.

Cenomanian to Campanian water-loaded subsidence is 0.4–0.8 km for all wells in the study area. Best-fitting theoretical thermal subsidence curves indicate that stretching beneath all wells was modest ($\beta < 1.5$; Figure 18). Cenozoic subsidence at the northern and southern fringes of the Mauritanian basin is very low (Figure 18). In contrast, wells in the centre of the basin record water-loaded subsidence of up to 0.8 km from 23.8–0 Ma (~ 0.03 mm a^{-1}). This subsidence pattern is a significant departure from predicted thermal subsidence patterns. Reflection data does not contain evidence of significant Neogene stratigraphic growth (Figure 6). The thick Neogene sedimentary pile, mapped using the seismic dataset, indicates this subsidence pattern is regional and extends ~ 500 km from the centre of the Mauritanian basin (Figure 11).

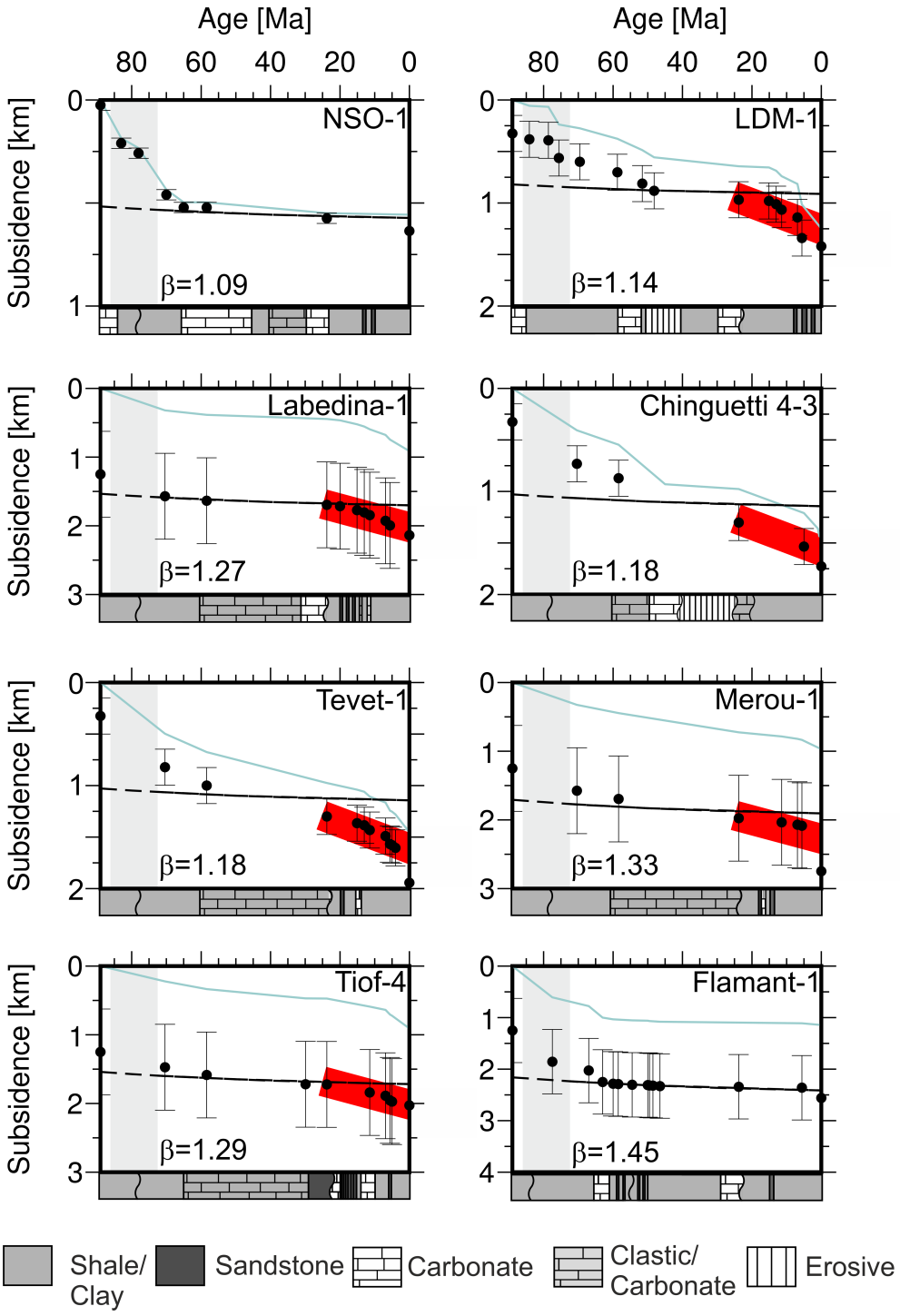


Figure 18: **Water-loaded subsidence results of Mauritanian wells**. (A-H) Cenozoic subsidence of Mauritanian margin. Solid lines = decompacted, water-loaded subsidence; line thicknesses = compaction uncertainties (< 50 m). Circles = decompacted, water-loaded subsidence corrected for palaeo-water depth (error bars); dashed-lines = best-fitting thermal subsidence profiles; blue lines = uncorrected subsidence; grey boxes = period of Late Cretaceous subsidence (see section 3.7); red lines = anomalous Neogene subsidence (0.03 mm a^{-1}). (I-J) Gray/black curves = Haq/Miller eustatic curves (Haq et al., 1987; Miller et al., 2005).

3.5 Discussion

Following a major change in the relative movement and collision of the African and Eurasian plates at 85 Ma, prominent regional unconformities across the Senegal and Gabon Basins mark the cessation of rifting (Laubscher and Bernoulli, 1977; Savostin et al., 1986; Westphal et al., 1986; Dercourt et al., 1986; Ziegler, 1988). This is concomitant with the beginning of a period of erosion caused by basin inversion associated with the Alpine orogeny (De Klasz, 1978; Guiraud et al., 1987; Teisserenc and Villemin, 1989). Backstripping results from this study show that a period of Late Cretaceous subsidence occurred across the Mauritanian basin (grey boxes in Figure 18). During this time, < 2 km of sediment was accumulated in the northern and southern parts of the Mauritanian basin (Figure 11E, Chapter 2). This is consistent with results from Janssen et al. (1995), who backstrip 20 wells from across the Senegal basin and observe ~ 400 m of water-loaded tectonic subsidence across the West African margin during this time. Following basin inversion, Campanian to Maastrictian subsidence is recorded in many northwest-southeast striking African basins (e.g. Senegal, Gabon, Lamu, Sirte, Termit, Abu Gabra, Janssen et al., 1995; Benkhelil, 1989; Guiraud, 1993). Whilst it is beyond the scope of this study to determine the exact cause of this phase of anomalous Late Cretaceous subsidence, a plausible explanation for the observed stress regime and renewal of subsidence following basin inversion is the ongoing, possibly accelerated, subduction of the Neo-Tethys at the northeastern African margin (Janssen et al., 1995). Following tectonic quiescence from the Paleogene to Oligocene, the extent of Neogene to Recent subsidence observed across the Mauritanian basin is variable. Wells at the northern and southern fringe of the Maurtianian basin indicate that Neogene subsidence was < 50 m (Figure 18). In contrast, stratigraphy in the centre of the Mauritanian basin records up to 0.8 km of Neogene subsidence. Interpretation of a two-dimensional seismic reflection dataset shows that Neogene subsidence occurred over an area of $\sim 250 \times 10^3$ km^2 (Figure 11). Seismic data does not contain evidence of significant Neogene stratigraphic growth, which indicates that this phase of subsidence was unrelated to stretching or salt movement (Figures 6, 7 & 13). Neogene subsidence is an order of magnitude larger than, and the opposite sign to, estimated glacio-eustasy (Figure 18;

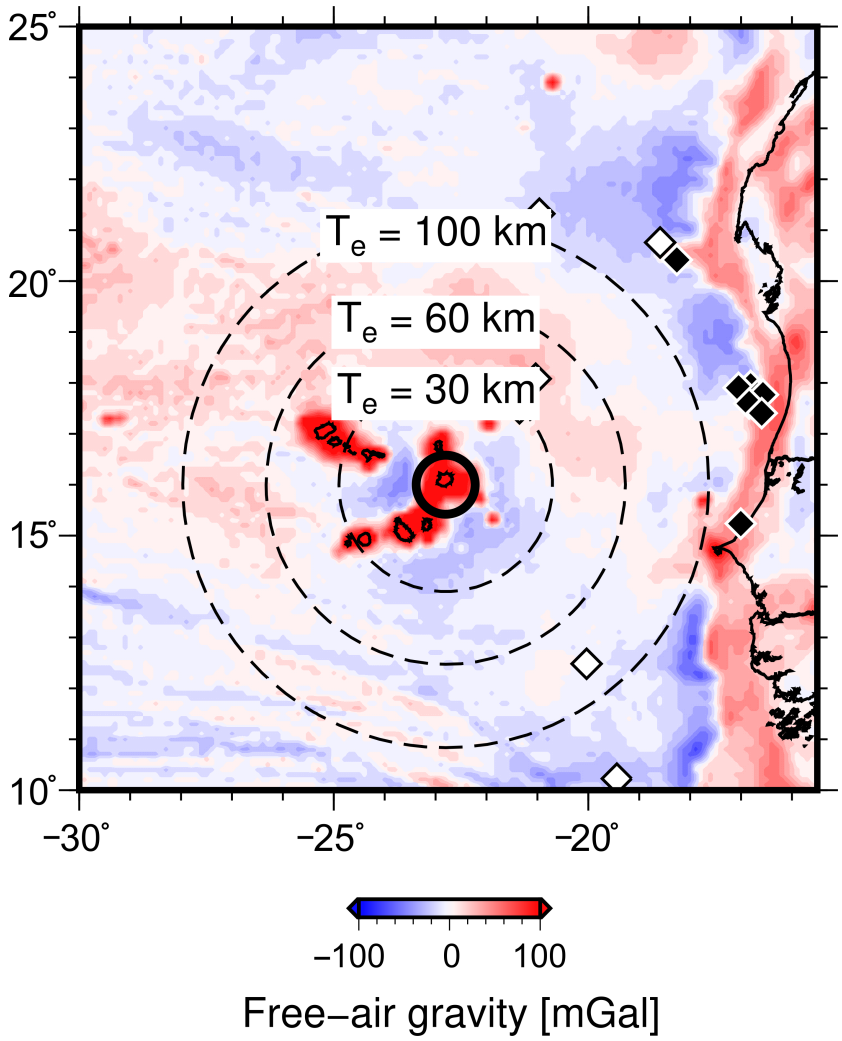


Figure 19: **Flexure due to Cape Verde crustal load**. Flexure of an infinite plate for different elastic thicknesses for a point load centred on Boa Vista (solid circle). Colour scale = free-air gravity data from EIGEN6c GOCE dataset (Förste et al., 2014). Dashed lines = position of maximum uplift (forebulge) for $T_e = 30$, 60 or 100 km (cf. Pim et al., 2008; Wilson et al., 2013). Black diamonds = backstripped wells on West African margin. White diamonds = IODP & DSDP wells.

Haq et al., 1987; Miller et al., 2005). The results of this study are in contrast to Janssen et al. (1995)'s hypothesis that Neogene–Recent subsidence in the Senegal/Mauritanian basin is a result of halokinetic movements, as evidence for this is not seen in the seismic data (Figures 6 & 7, Chapter 2).

The backstripping performed (e.g. Figure 18) assumes that the Mauritanian margin has negligible elastic strength, which is consistent with Watts (1994)'s suggestion that the lithosphere along parts of the northwest African margin

is weak ($T_e < 5$ km). To assess the impact of loading by Cape Verde on subsidence of the Mauritanian margin, the position of maximum uplift (i.e. flexural forebulge, $x_b = \pi\alpha_f$) was estimated, where flexural parameter, α_f, is a function of elastic thickness, T_e . Assuming an infinite elastic plate and that the load is concentrated at Boa Vista, ~ 700 km away from the backstripped wells in the Mauritanian basin. The flexural parameter is a function of flexural rigidity, D, thus

$$\alpha_f = \left[\frac{4D}{g\left(\rho_m - \rho_w\right)}\right]^{1/4}, \qquad D = \frac{ET_e^3}{12\left(1-\sigma^2\right)}. \tag{3.11}$$

Mantle and water densities were set to $\rho_m = 3300$ kg m^{-3} and $\rho_w = 1000$ kg m^{-3}, $g = 9.81$ m s^{-2}. Young's modulus $E = 70$ GPa and Poisson's ratio, $\sigma = 0.25$ (e.g. Turcotte and Schubert, 2002). Using Pim et al. (2008)'s estimate of $T_e = 30$ km from wide-angle seismic data and gravity modelling indicates that the crest of the forebulge, x_b, is 230 km away from Cape Verde. This small circle encloses the moat of negative free-air gravity anomalies surrounding the islands at the centre of the rise. If $T_e = 60$ km, x_b = 392 km (cf. Wilson et al., 2013). If $T_e = 100$ km, $x_b = 574$ km. These calculations show that loading from Cape Verde could not have generated the Neogene subsidence observed ~ 700 km away in the Mauritanian basin (Figure 19).

Thus, loading, salt withdrawal, thin-skinned tectonics or glacio-eustasy cannot explain the observed localised Neogene subsidence of the Mauritanian basin. Instead, shear wave tomography, residual ocean-age depth measurements and long wavelength free-air gravity anomalies indicate that a gradient in sub-plate support exists from Cape Verde to Mauritania (Figure 20). Calculated excess temperatures in the asthenosphere are large enough to generate isostatic support of a few hundred meters. Note that this estimate of sub-plate support does not include that generated by viscous stresses (i.e. the dynamic problem). Close agreement between observed and theoretical thermal subsidence patterns and fast shear wave velocity anomalies beneath the plate indicate that sub-plate support has developed since ~ 23 Ma. ^{40}Ar/^{39}Ar and K/Ar dated Cenozoic volcanism indicates that growth of the Cape Verde swell has been sporadic since ~ 26 Ma (e.g. Mitchell et al., 1983; Holm et al., 2008; Madeira et al., 2010). Growth of the swell probably precedes onset of Neogene

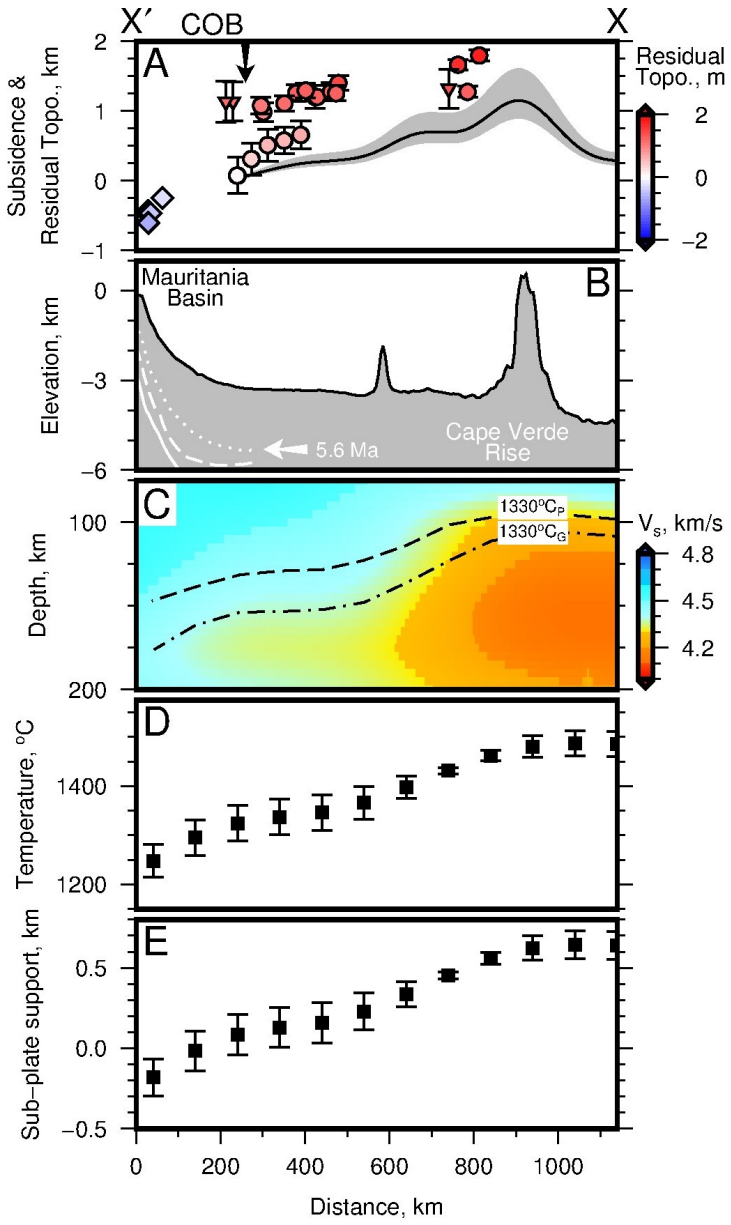


Figure 20: **Summary of results along cross-section X—X′** (see Figures 13 & 14). (A) Circles and downward pointing triangles = residuals from ocean age-depth projected onto line. Diamonds = Neogene–Recent (23.8–0 Ma) subsidence calculated from wells in the centre of Mauritanian basin. Gray band and black line = dynamic topography calculated using long wavelength (800 ± 2500 km) free-air gravity anomalies from GOCE dataset and an admittance of 35 ± 10 mGal km^{-1}. Arrow = continent-ocean boundary (COB) mapped using reflection seismic data. (B) Topographic swath and thickness of sedimentary rock in Mauritanian basin: solid/dashed/dotted white lines = 58.4/23.8/5.6 Ma horizons (Figure 6). (C) Surface wave tomography. Dash-dot/dash lines = 1330°C isotherm calculated using (P) Priestley and McKenzie (2006)/(G) Goes et al. (2012) parametrisations. (D) Squares = calculated average temperature between 100–200 km depth. Error bars = range from P and G parametrisations. (E) Black squares = isostatic support calculated using excess temperatures (Equation 3.7).

subsidence in the Mauritanian basin by a few million years. These observations combined with a gradient in residual ocean age depth measurements and shear wave velocity anomalies indicate small-scale ($\sim 1000 \times 200$ km) upper mantle convection beneath Cape Verde and the West African margin since at least ~ 23 Ma. Neogene infilling of accommodation, which I suggest was created by mantle drawdown, has resulted in hydrocarbon maturation in the Mauritanian basin (Vear, 2005).

Models of small-scale (e.g. edge-driven) convection often invoke plate motion as an important cause of mantle flow (e.g. Shahnas and Pysklywec, 2004; Davies and Rawlinson, 2014). However, that mechanism cannot explain the observations from this study because the African plate has been relatively stationary since ~ 30 Ma (e.g. Burke, 1996). Instead, Neogene subsidence patterns, the history of magmatism at Cape Verde, and tomographic and isostatic modelling indicate that hot upwelling mantle and consequent asthenospheric flow can trigger mantle downwelling at continental margins (Figure 21).

3.6 Conclusion

The subsidence history of the Mauritanian basin, offshore West Africa, was calculated by backstripping 8 wells and mapping 53,000-line-km of two dimensional seismic reflection data. Cenomanian–Campanian subsidence is observed in wells across the basin and is followed by post-rift thermal sag. Stretching factors are modest, $\beta < 1.5$. In the centre of the basin an additional 0.4–0.8 km of Neogene water-loaded subsidence is observed. The amplitude of subsidence indicates that glacio-eustasy is not responsible for generating the regional increase in accommodation observed. The wavelength, location and amplitude of subsidence preclude loading as a viable mechanism for generating observed subsidence. Stratal geometries in seismic data intersecting wells contain little/no evidence of growth in the shallow section, which indicate that Neogene salt withdrawal or thin-skinned tectonics did not generate the observed subsidence patterns. Measured ocean-age depth residuals, calculated subsidence histories, magmatic histories and a new shear wave tomographic model suggest that upper mantle convection has generated an east-west bathymetric

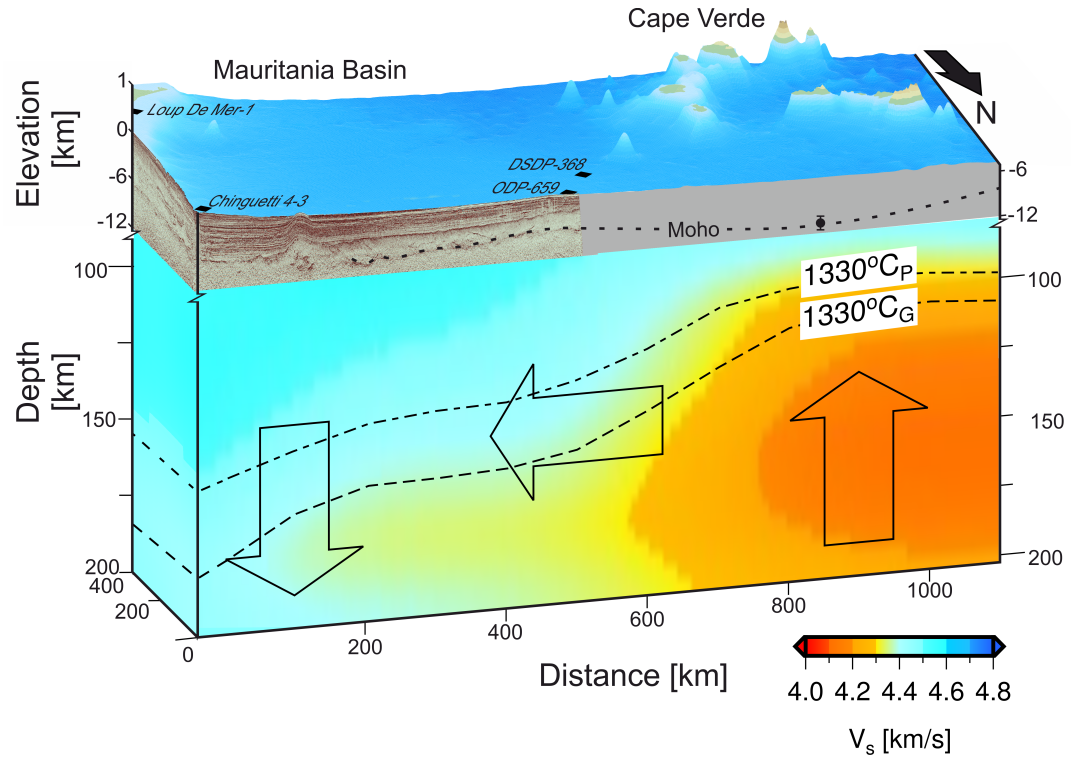


Figure 21: **Cartoon summarising results**. Black circle beneath Cape Verde = Moho estimated from wide-angle seismic data (Pim et al., 2008). Arrows indicate shallow mantle flow.

gradient of $\sim 1/300$ during the last ~ 23 Ma (Figure 21). These observations are consistent with mantle downwelling below the Mauritanian part of the West African margin that formed in response to the flow of hot asthenosphere away from the upwelling mantle beneath Cape Verde.

3.7 Prelude to next chapter

The distribution of solid sediments deposited in the Mauritanian basin since the Late Cretaceous has varied significantly with time. Accommodation created due to Late Cretaceous and Neogene–Recent subsidence is responsible for the accumulation of > 8 km of sediments across the basin, which has resulted in the formation of significant working petroleum systems in the Mauritanian basin such as the Tiof and Chinguetti fields. However, to fully understand the nature of sedimentation to West Africa's passive continental margin, it is necessary to bring the processes that create the conditions to capture significant

volumes of sediment offshore and those that are responsible for producing clastic sediments onshore, together. In the next chapter, I use remote sensing data to extract 14700 longitudinal river profiles from across the African continent, apply a least squares approach to invert for a spatio-temporal history of continental uplift rate and predict patterns of sedimentary flux to West Africa's passive margin. To address the 'sorce to sink' problem, patterns of sedimentary flux calculated from drainage inversion are compared to results from Chapter 2. The relationship between dynamic uplift and offshore sedimentary flux to Africa's passive margins is explored by contextualising the uplift rate histories of major river systems and the sedimentary flux histories of the continent's passive margin basins.

Chapter 4

African uplift and sedimentary flux from continental drainage inversion

4.1 Introduction

Records of clastic efflux to passive margins contain information about histories of tectonic and erosional processes. They provide clues about longevity of topography and erosional processes, and in regions of dynamic support the sedimentary archive can constrain length- and time-scales of mantle convective processes (e.g. Walford et al., 2005; Clift and Sun, 2006; Allen, 2008; Rouby et al., 2009; Somme et al., 2011; Czarnota et al., 2014). Furthermore, constraining sources of sedimentary rock and their history of deposition is critical for understanding the origin and distribution of natural resources including hydrocarbon reservoirs (e.g. Vear, 2005; Somme et al., 2011). To tackle this problem, I compare measurements of sedimentary efflux to the West African passive margin recorded by stratigraphy (Chapter 2) and predictions calculated by inverting continental longitudinal river profiles from the sediment source region onshore Mauritania and Senegal, using a least-squares approach. Drainage extracted from across the African continent is inverted to calculate a best-fitting spatio-temporal history of uplift rate. I focus on calculating patterns

of Neogene–Recent sedimentary flux to the Mauritanian margin of West Africa, which is drained by several large rivers that are sourced atop long wavelength, dynamically supported, topographic swells (Figure 3).

African uplift

It is generally accepted that convective flow in the sub-lithospheric mantle has generated African topography during the last 30 Ma (e.g. Nyblade and Robinson, 1994; Burke, 1996; Moucha and Forte, 2011; Paul et al., 2014; Rudge et al., 2015). The observed topography is strongly bimodal. Sub-equatorial Africa is characterised by a broad $\sim 10^4 \times 10^4$ km superswell whilst northern Africa is generally low-lying (Nyblade and Robinson, 1994). Superimposed on this bimodal framework are smaller $\sim 1000 \times 1000$ km domal swells (Holmes, 1944; Burke, 1996). Widespread volcanic activity, basin subsidence, uplifted domes (e.g. Bié, Hoggar, Tibesti and Fouta Djallon; Figure 3 and Figure 22) and extension at the East African Rift characterise present-day African topography (e.g. Burke, 1996; Crosby et al., 2010; Moucha and Forte, 2011). Estimates of dynamic topography calculated using long wavelength (800–2500 km) components of the EIGEN6c GOCE gravity field using an admittance, $Z = 35 \pm 10$ mGal km^{-1} is shown in Figure 22 (McKenzie and Fairhead, 1997; Crosby et al., 2010; Jones et al., 2012; Förste et al., 2014; Hoggard et al., 2017). These results imply that the Bié, Namibian, South African and North African swells (e.g. Atlas, Fouta Djallon, Hoggar, Tibesti) are dynamically supported by sub-lithospheric density anomalies. Radial drainage patterns are centred on many of these swells and many areas of low topography have dendritic drainage networks (e.g. Congo; Figure 22). These observations suggests that sub-plate processes determine the pattern of drainage across the African continent. A subset of these continental drainage patterns have been used to invert for smooth spatio-temporal histories of uplift, which yields results that are consistent with the notion that many of Africa's domal swells have grown during the last ~ 30 Ma (Pritchard et al., 2009; Roberts et al., 2012a; Paul et al., 2014; Rudge et al., 2015). A concomitant increase in clastic solid sedimentary flux to many of Africa's major river delta systems is also recorded during the last ~ 30 Ma. This includes the Senegal, Volta, Niger, Congo, Limpopo, Zambezi, Jubba-

Shebelle and Nile (Dingle, 1983; DuToit et al., 1997; Aal et al., 2000; Hall et al., 2005; Walford et al., 2005; Paul et al., 2014; Grimaud et al., 2018). However, the link between dynamic topography, drainage evolution and resultant solid sedimentary flux remains poorly understood.

4.2 Data & Methodology

4.2.1 Continental drainage and dynamic topography

A digital elevation model (DEM) of the African continent has been generated using the Shuttle Radar Topography Mission (SRTM) dataset, which has a resolution of $\sim 90 \times 90$ m (Farr et al., 2007). Hancock et al. (2006) tested the vertical and horizontal accuracy of SRTM data by benchmarking against GPS measurements on spatial scales of 10^1–10^6 m, yielding values of $\pm$16 m and ± 20 m, respectively. In order to extract longitudinal river profiles, anomalous spikes and sinks are first removed from the DEM. Flow routing algorithms in the Esri software package, ArcGIS, were used to identify the direction of steepest descent. The number of cells upstream of any given cell was calculated and a threshold drainage area determined the maximum number of cells which contribute to the initiation of overland flow. A total of 14700 rivers have been extracted from the DEM and verified using LandSat and SRTM satellite imagery (Figure 23).

4.2.2 Uplift as a function of time and space

Forward model

To investigate the source of sedimentary flux to Africa's passive margins, drainage data was inverted for a history of Neogene uplift rate. First, a suitable forward model has to be defined. The rate of change of elevation, $\partial z/\partial t$, of a river must be a function of uplift, U, and erosion, E, such that:

$$\frac{\partial z}{\partial x} = U(x,t) + E(x,t) \tag{4.1}$$

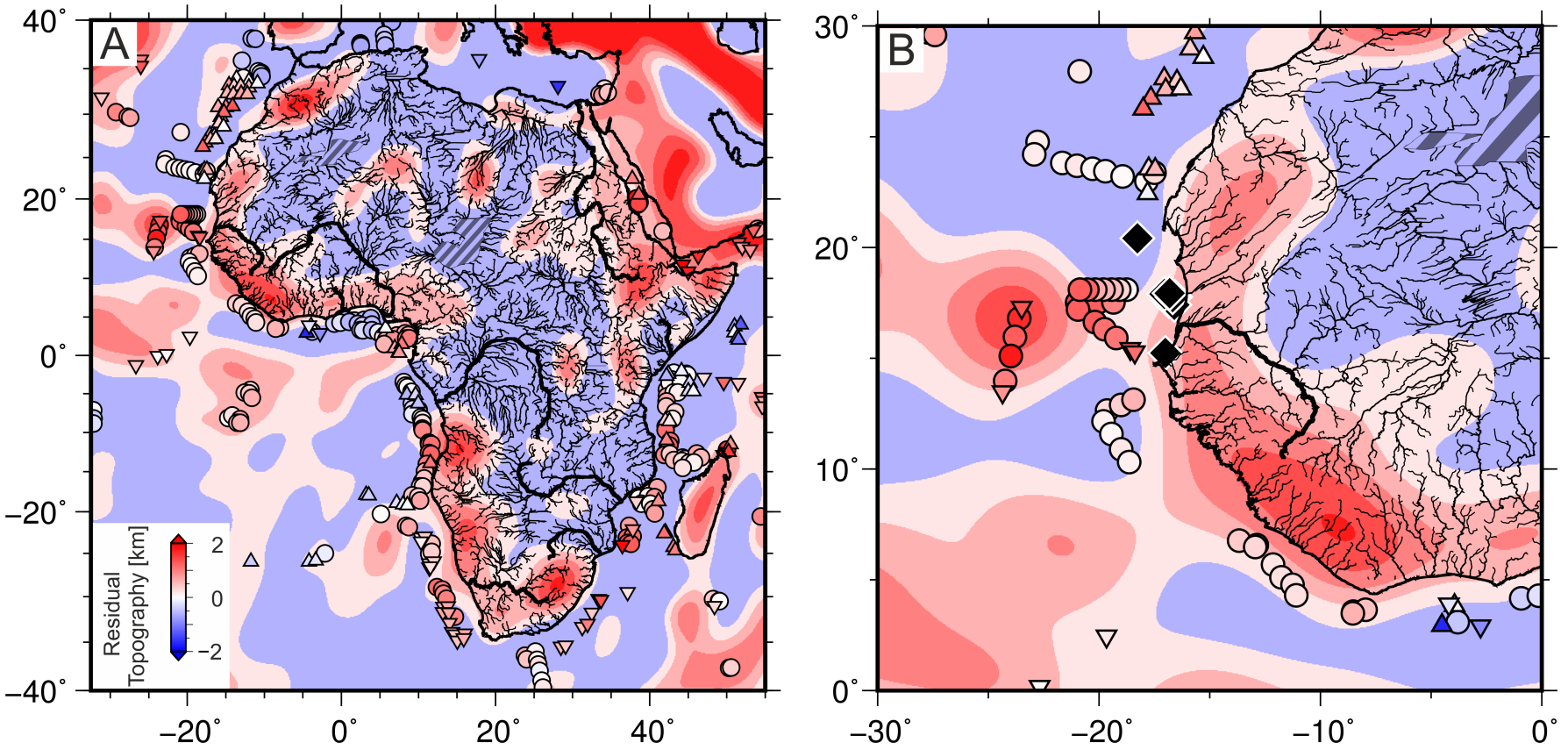


Figure 22: **Sub-plate support and drainage patterns of Africa and the Mauritanian margin**. (A) Red/white/blue colour scale = dynamic topography calculated using long wavelength ($\sim$ 800–2500 km) free-air gravity data from GOCE dataset and an admittance $Z = 35$ mGal km^{-1} (see e.g. Jones et al., 2012; Förste et al., 2014); contour interval = 10 mGal $\sim$ 0.3 km. Thin/thick black curves = drainage networks extracted from SRTM DEM (see Figure 3). Circles/triangles = accurate/upper or lower bound estimates of residual ocean-age depths (Hoggard et al., 2017; Lodhia et al., 2018). (B) Zoom-in of Residual topography in study area. Black diamonds = wells used in this study. Note radial drainage patterns atop Africa's domal swells. Hatched areas = regions where drainage cannot be reliably extracted.

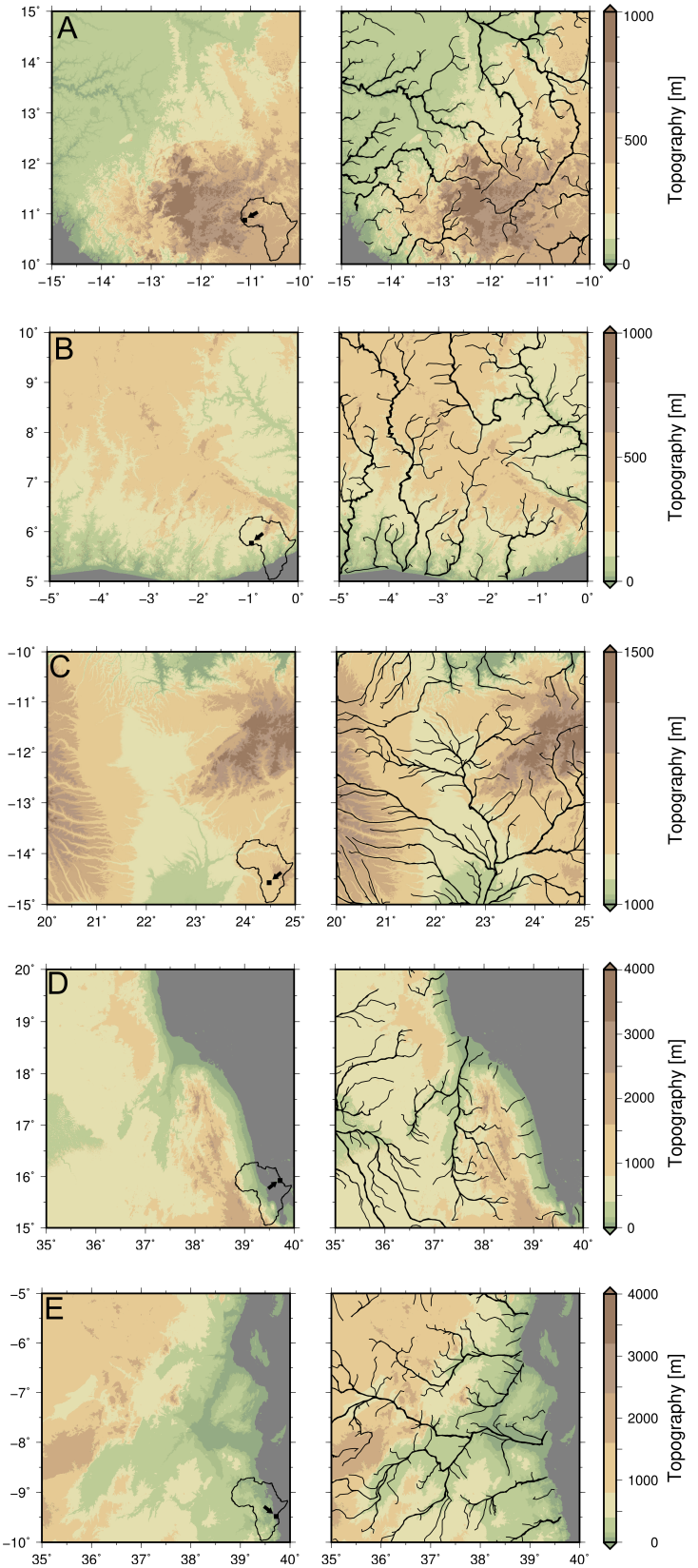


Figure 23: **Continental drainage extreacted from SRTM DEM**. (A–E) Selected tiles of SRTM DEM from across the African continent on left hand side. Black lines on right hand side = drainage extracted using methodology described in Section 4.2. Black squares and map on bottom right = location of SRTM DEM data tile.

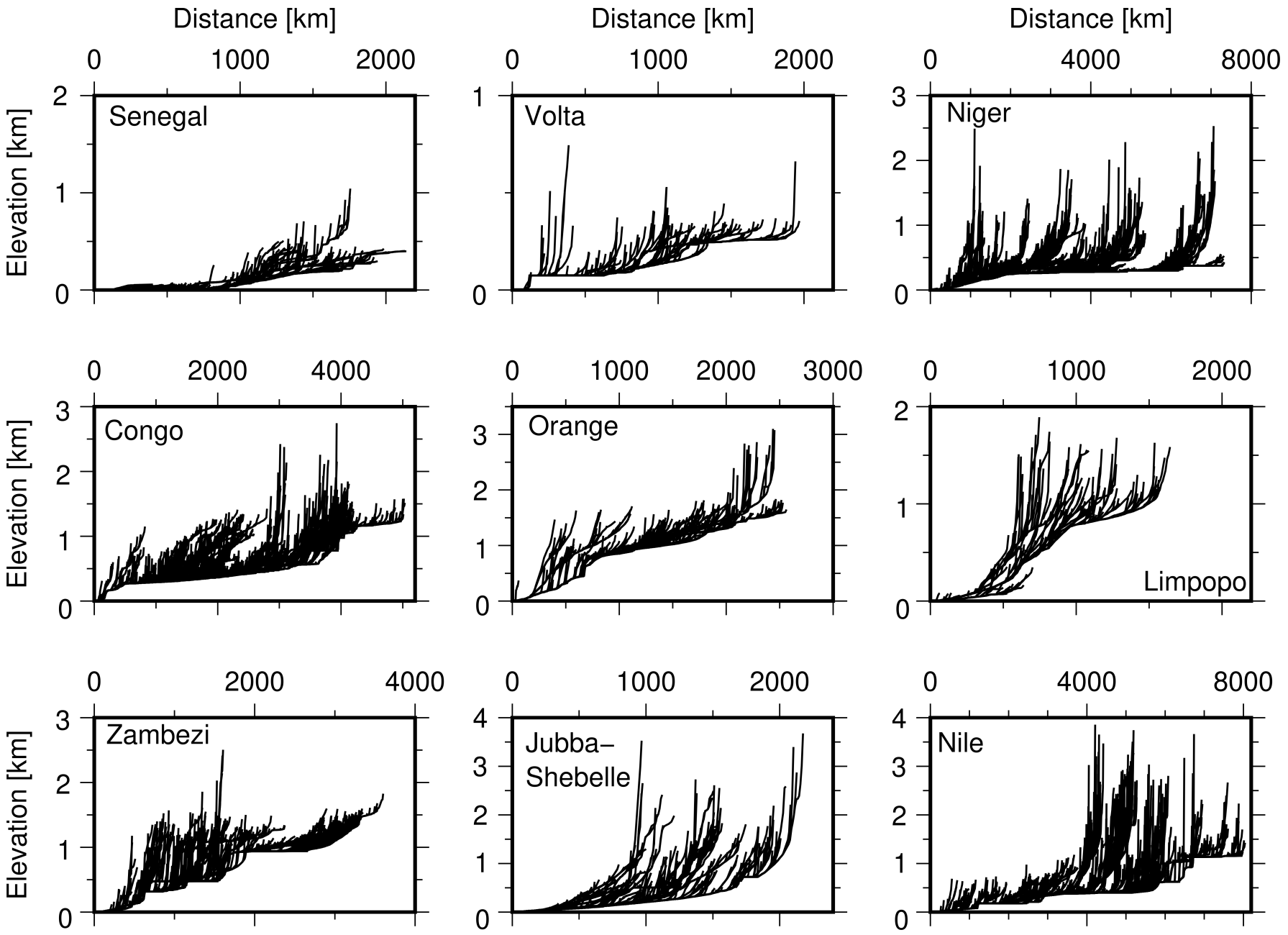


Figure 24: **Longitudinal river profiles of major African drainage systems**. Black lines = longitudinal river profiles extracted from SRTM DEM.

where x is the downstream distance from the river source and t is time. The erosion rate, $E(x,t)$, parametrises a complex suite of fluvial erosional processes. After Hack (1957) and Weissel and Seidl (1998), Pritchard et al. (2009), I assume that river discharge varies geometrically with distance, x. Their governing law for the evolution of a longitudinal river profile is of the form:

$$\frac{\partial z}{\partial t} = U(t) - v_0 A(x)^m \left(-\frac{\partial z}{\partial x}\right)^n + \kappa(x)\frac{\partial^2 z}{\partial x^2} \tag{4.2}$$

where v_0 is the knickpoint velocity if $m = 0$ and $n = 1$, m and n are dimensionless parameters, and κ is the erosional diffusivity. The term $A(x)^m$ is used as a proxy for discharge by Whipple and Tucker (1999), where $A(x)$ is the upstream drainage area at any position, x. This term is represented as x^m by Pritchard et al. (2009) and represents discharge, which increases downstream. The relative importance of advective (i.e. detachment-limited) and diffusive (i.e. transport-limited) terms is determined by a morphodynamic Péclet number:

$$Pe = \kappa^{-1} v_0^{\frac{1}{n}} L^{\frac{1+m}{n}} U_0^{\frac{l-1}{n}} \tag{4.3}$$

where U_0 is uplift rate (Pritchard et al., 2009). Where the Péclet number, $Pe >> 1$, the diffusive term becomes negligible and Equation (4.2) becomes:

$$U(t) = \frac{\partial z}{\partial t} + v_0 A(x)^m \left(-\frac{\partial z}{\partial x}\right)^n \tag{4.4}$$

Hence, Pritchard et al. (2009) showed that at long wavelengths the erosional process is dominated by advection, i.e. knickpoint retreat, and that changes in lithology and discharge play a secondary role in determining the transient form of a river profile (e.g. Hack, 1957; Howard, 1971, 1987, 1988; Howard and Hemberger, 1991; Howard et al., 1994; Howard and Kerby, 1983; Rosenbloom and Anderson, 1994; Weissel and Seidl, 1998; Whipple and Tucker, 1999; Sklar and Dietrich, 1998, 2001; Tomkin et al., 2003; Crosby and Whipple, 2006; Whittaker et al., 2007; Pritchard et al., 2009; Roberts and White, 2010; Roberts et al., 2012a,b; Whittaker and Boulton, 2012; Rudge et al., 2015).

In advective syetems (i.e. Equation 4.4), the diffusive term in Equation (4.2) becomes negligible as $\kappa << 1$ and $Pe >> 1$. Hence, Equation (4.2) reduces to:

$$\frac{\partial z}{\partial t} = U(x,t) - vA(x)^m \left(\frac{\partial z}{\partial x}\right)^n \tag{4.5}$$

To solve for uplift as function of space and time, $U(x,t)$, an inverse method is required that uses present-day drainage measurements and erosional parameters calibrated by independent geological constraints.

The erosional parameters v, m and n affect shapes of predicted river profiles in different ways (e.g. Rosenbloom and Anderson, 1994; Whipple and Tucker, 1999; Pritchard et al., 2009; Roberts and White, 2010; Roberts et al., 2012b). There is considerable debate about the values of v, m and in particular n (e.g. van der Beek and Bishop, 2003; Mudd et al., 2014; Lague, 2014). It has been shown that v and m trade off negatively with each other so that different combinations of v and m yield equally acceptable fits between observed and calculated river profiles (Roberts and White, 2010; Croissant and Braun, 2014). If $n \neq 1$, shocks can occur, whereby steeper slopes propagate faster than shallower slopes (Pritchard et al., 2009; Royden and Perron, 2013). There is no compelling evidence for shock wave behaviour along rivers at the long wavelengths of which this study is concerned. Fits between observed and theoretical river profiles are lowest when $n \sim 1$ (e.g. Paul et al., 2014) which is corroborated by some field studies (Whittaker et al., 2007; Whittaker and Boulton, 2012). The constant, v must be calibrated using independent geological data. The value of m depends to some extent on the topology of the drainage network and can be estimated by comparing misfit between families of observed and theoretical river profiles. Paul et al. (2014) calibrate the relationship between v and m for westward draining rivers on the Bié dome, Angola (Figure 22) which has a minimum post-Pliocene uplift rate of 0.3 mm a^{-1} at the coast (Guiraud et al., 2010). When $n = 1$ and $m = 0.35$, Paul et al. (2014) obtain $v = 3.62$ and successfully constrain $\partial z/\partial t$ using Miocene uplift rates (Partridge, 1998; Partridge and Maud, 2000; Burke and Gunnell, 2008). These values were also applied to the African continent by Rudge et al. (2015). In common with previous authors, I use these values of v, n and m to invert river profiles for continental uplift rate histories across Africa.

Inverse modelling of drainage

The principle behind the inverse method is to allow uplift rate, $U(x,t)$ to vary with space and time to calculate theoretical longitudinal river profiles. Uplift rate is varied until the misfit between calculated and observed river profiles is minimised. The calculated uplift rate histories of African domes (e.g. Bié, Southern Africa) indicate that these swells grew during the last 40–30 Ma at rates of fractions of a millimetre per year. Roberts et al. (2012b) generalised this approach to solve for uplift rate as a function of space and time. They showed that families of longitudinal river profiles contain coherent information about histories of regional uplift. Paul et al. (2014) extracted 710 river profiles of Strahler order ≥ 5, to reconstruct an uplift rate history of Africa since 50 Ma. Rudge et al. (2015) subsequently showed that similar results can be obtained by linear inversion without recourse to prior information (cf. Goren et al., 2014), which greatly speeds up the inversion process.

Equation (4.1) suggests that if the shape of a river profile is known (i.e. as can be extracted from SRTM DEM data, section 4.2.1) and if E is suitably parametrised, it is possible to extract $U(t)$. The residual rms misfit, H, between observed and theoretical river profiles is given by:

$$H = \sqrt{\frac{1}{K}\sum_{ij=1}^{lJ}\left(\frac{z_{ij}^{o}-z_{ij}^{c}}{\sigma}\right)^{2}} \tag{4.6}$$

where z_{ij}^{o} and z_{ij}^{c} are observed and predicted river profile elevations, σ is the uncertainty associated with each elevation (typically ~ 20 m away from narrow channels, Farr et al., 2007), l is the number of points along a given river profile, J is the number of river profiles, and K is total number of data points (Rudge et al., 2015). At $n \sim 1$, rms misfit has a global minimum (Pritchard et al., 2009; Roberts and White, 2010; Roberts et al., 2012a,b; Paul et al., 2014; Rudge et al., 2015). Hence, at $n = 1$, a reliable uplift rate history can be calculated using the inverse method. To invert for U, Roberts et al. (2012b) devised a trial function with suitable penalties, which measures the difference (i.e. residual misfit) between an observed river profile and a synthetic river profile calculated for any given U. This trial function is minimised by systematically varying U as a function of time alone. Roberts et al. (2012b) find that v and m trade-

off negatively against each other to some extent which means that different combinations of these parameters will produce the similar uplift rate histories and fit a given river profile. When $n = 1$, v and m directly control knickpoint velocity, v. When $U = 0$ and $\kappa = 0$, Equation (4.1) can be rearranged as:

$$v = \frac{\partial z}{\partial t}\left[A^m\left(\frac{\partial z}{\partial x}\right)^n\right]^{-1} \tag{4.7}$$

Roberts et al. (2012b) find that if $\kappa = 0$ and $n = 1$, the time taken for a knickzone to propagate upstream, τ_G, is given by:

$$\tau_G = \int_0^x \frac{dx}{vA^m} \approx \sum_{i=1}^{x} \frac{\Delta x_i}{vA_i^m} \tag{4.8}$$

whereby τ_G is the Gilbert Time (i.e. landscape response time). Roberts et al. (2012b) reduce rms misfit from 54 to ∼2 following model optimisation for the Colorado River. Their results show that joint inverse modelling of the Colorado River and its principal tributaries suggests that three phases of uplift produced the large-scale knickzones. This form of Monte Carlo inversion allows uncertainty envelopes to be calculated for $U(t)$, where uncertainty is found to decrease towards the present day (Roberts et al., 2012b). This method is exploited by Rudge et al. (2015), who closely follows the approaches used by Lighthill and Whitham (1955); Luke (1972); Weissel and Seidl (1998); Smith et al. (2000), and Pritchard et al. (2009) to derive the following analysis. The solution to the kinematic wave equation (Equation 4.5) takes the form of $z(x,t) = z(x(t),t)$. Since:

$$\frac{dz}{dt} = \frac{\partial z}{\partial t} + \frac{dx}{dt}\frac{\partial z}{\partial x} = \left(vA^m + \frac{dx}{dm}\right)\frac{\partial z}{\partial x} - U(x(t),t) \tag{4.9}$$

the solution can be written as a pair of ordinary differential equations, such that:

$$\frac{dx}{dt} = -vA^m \tag{4.10}$$

and

$$\frac{dz}{dt} = -U(x(t),t) \tag{4.11}$$

The appropriate boundary conditions at $t = 0$ are:

$$x = x^*, z = z^* \tag{4.12}$$

and at $t = \tau_G$ are:

$$x = 0, z = 0 \tag{4.13}$$

where τ_G is the Gilbert Time. The first boundary condition represents the present day, where at a position x^* along a river, the elevation is z^*. The second boundary condition represents a time in the past, τ_G, where the characteristic curve intersects the river mouth (i.e., $x = 0$), which occurs at sea level. From Equations (4.10), (4.12) and (4.13), τ_G must satisfy:

$$\tau_G = \int_0^{x^*} \frac{dx}{vA^m} \tag{4.14}$$

Hence a general solution for Equations (4.10)–(4.13) can be written in integral form as:

$$\tau_G - t = \int_0^{x(t)} \frac{dx}{vA^m} \tag{4.15}$$

and

$$z^* = \int_0^{\tau_G} U(x(t), t)dt \tag{4.16}$$

Hence, to calculate uplift, U as a function of space, $x(t)$ and time t, Equation (4.16) must be solved.

Linear least squares inversion after Rudge et al. (2015)

The inversion process as set out by Rudge et al. (2015) is carried out in three steps. Firstly, Equation (4.10) is integrated once using the trapezoidal rule to yield values of Gilbert Time, for which Equation (4.15) is used obtain the characteristic curves. Secondly, the curves must be combined with linear interpolation to discretise Equation (4.16) using the trapezoidal rule. Thirdly, a damped least squares approach is exploited.

The time taken for a kinckzone to travel along a characteristic path is given by Equation (4.14), and for a set of points, n along curve, j, can be expressed as:

$$\tau_{G_j} = \int_{x_n^*}^{x_n^*-1} \frac{dx}{vA^m} + \int_{x_{n-1}^*}^{x_{n-2}^*} \cdots + \int_{x_{j+1}^*}^{x_j^*} \frac{dx}{vA^m} \tag{4.17}$$

Equation (4.17) is discretised using the trapezoidal rule, such that:

$$\tau_{G_j} = \sum_{k=j}^{n} \frac{(x_k^* - x_{k+1}^*)}{2} \left(\frac{1}{vA\left(x_n^*\right)^m} + \frac{1}{vA\left(x_{n+1}^*\right)^m} \right) \tag{4.18}$$

where $x_n^* = 0$ at the river mouth and $\tau_G = 0$ at the present day. Similarly, Equation (4.15) can be approximated by:

$$\tau_{G_j} - T_{ij} = \int_0^{x_i^*} \frac{dx}{vA^m} = \tau_{G_i} \tag{4.19}$$

so that

$$T_{ij} = \tau_{G_j} - \tau_{G_i} \tag{4.20}$$

where

$$i = j, j+1, \ldots n \tag{4.21}$$

T_{ij} are values of time along the characteristic curve that is located at $x = 0$ and $t = \tau_G$ where distances and elevations along the river are known (i.e., $x(T_{ij}) = x_i$). Uplift rate, U, is defined at discrete times and at positions (e.g. $t_1, t_2, \ldots$ at positions $x_1, x_2, \ldots$). To determine the value of U in between discrete times and positions, linear interpolation is required. Elevations are determined by integrating uplift rates according to Equation (4.16) along the characteristic paths using the trapezoidal rule.

For intermediate points located between nodes whose loci are defined by t and x (see Figure A1 in Rudge et al., 2015), uplift rate histories are interpolated by applying Equation (4.16) to each point. Along a characteristic curve, j, Equation (4.16) takes the form:

$$z_j = \int_{S_{1_j}}^{S_{2_j}} U(\mathbf{x}(t), t)dt + \int_{S_{2_j}}^{S_{3_j}} \ldots \tag{4.22}$$

where $\mathbf{x}(t)$ is the position in space along the characteristic curve (i.e. river profile) at time, t. Equation (4.22) cannot be solved directly, however can be approximated by:

$$z_j^* = \sum_{k=1}^{m(j)} \frac{(S_{k+1,j} - S_k)}{2} \left[U\left(\mathbf{x}\left(S_{k+1,j}\right), S_{k+1,j}\right) + U\left(\mathbf{x}\left(S_{kj}\right), S_{kj}\right) \right] \tag{4.23}$$

where S_{ij} consists of dividing the integral up, both by times T_{ij}, at which the position of the river is known and by times $t_1, t_2, \ldots$, at which uplift times are discretised. The number of points on characteristic curve j is $m(j)$. At time T_{ij}, linear interpolation in time is carried out so that:

$$U\left(T_{ij}, \mathbf{x}\left(T_{ij}\right)\right) = U\left(T_{ij}, \mathbf{x}_i\right) = \frac{\left[T_{ij}^+ - T_{ij}\right] U\left(T_{ij}^+, \mathbf{x}_i\right) + \left[Tij - T_{ij}^-\right] U\left(T_{ij}^-, \mathbf{x}_i\right)}{T_{ij}^+ - T_{ij}^-} \tag{4.24}$$

where T_{ij}^+ and T_{ij}^- are time nodes which bracket T_{ij}. At a time t_i, a linear interpolation in space is carried out such that:

$$U\left(t_i, \mathbf{x}(t_i)\right) = \alpha U\left(t_i, \mathbf{x}_a\right) + \beta U\left(t_i, \mathbf{x}_b\right) + \gamma U\left(t_i, \mathbf{x}_c\right) \tag{4.25}$$

where α, β and γ are the barycentric weights for position $\mathbf{x}\left(t_i\right)$. The mesh nodes of the triangle containing $\mathbf{x}\left(t_i\right)$ are $\mathbf{x}_a, \mathbf{x}_b$ and $\mathbf{x}_c$ (Rudge et al., 2015, see their Figure A2 for a diagram of the traingular mesh and nodes in relation to α, β and γ). Hence, there is now a linear relationship between each river elevation, z_j^*, and uplift rate at each point in space and time node which in matrix form, is written as:

$$\mathbf{z} = M\mathbf{U} \tag{4.26}$$

Using this methodology and 14700 longitudinal river profiles from across Africa, I solve the integral equation (Equation 4.16) to calculate the uplift rate history, $U(x,t)$, of the African continent. The spatial regularisation grid and distribution of uplift vertices used with the triangular mesh described for Africa and West Africa is shown on Figures 25 & 26.

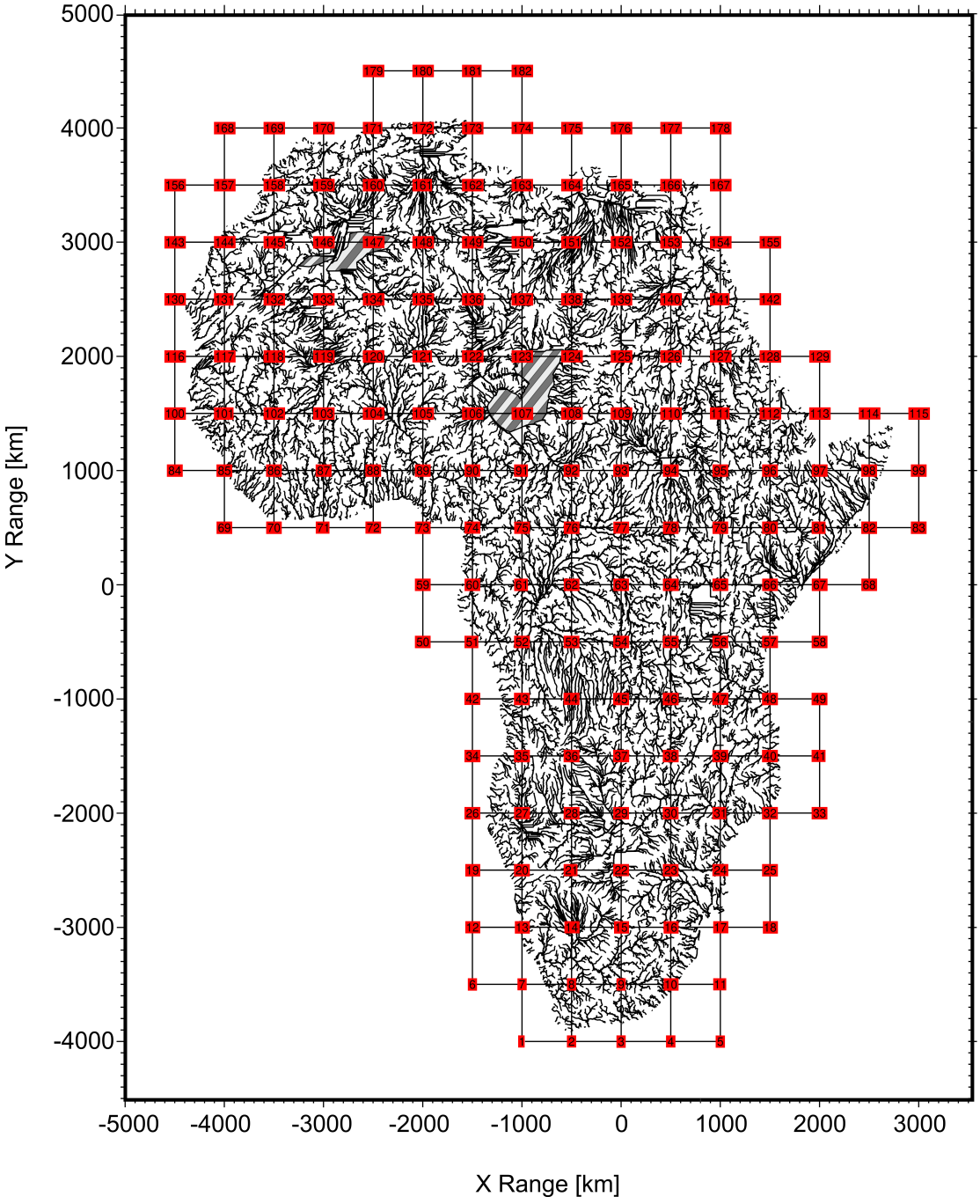


Figure 25: **Distribution of vertices in inverse model for African rivers**. Black lines = modelled rivers; red numbered boxes = position of vertices where uplift is input into the model. X and Y are plotted in kilometres. Uplift rate at each point along a river is linearly interpolated from four surrounding vertices. Hatched polygons = areas where drainage cannot be reliably extracted.

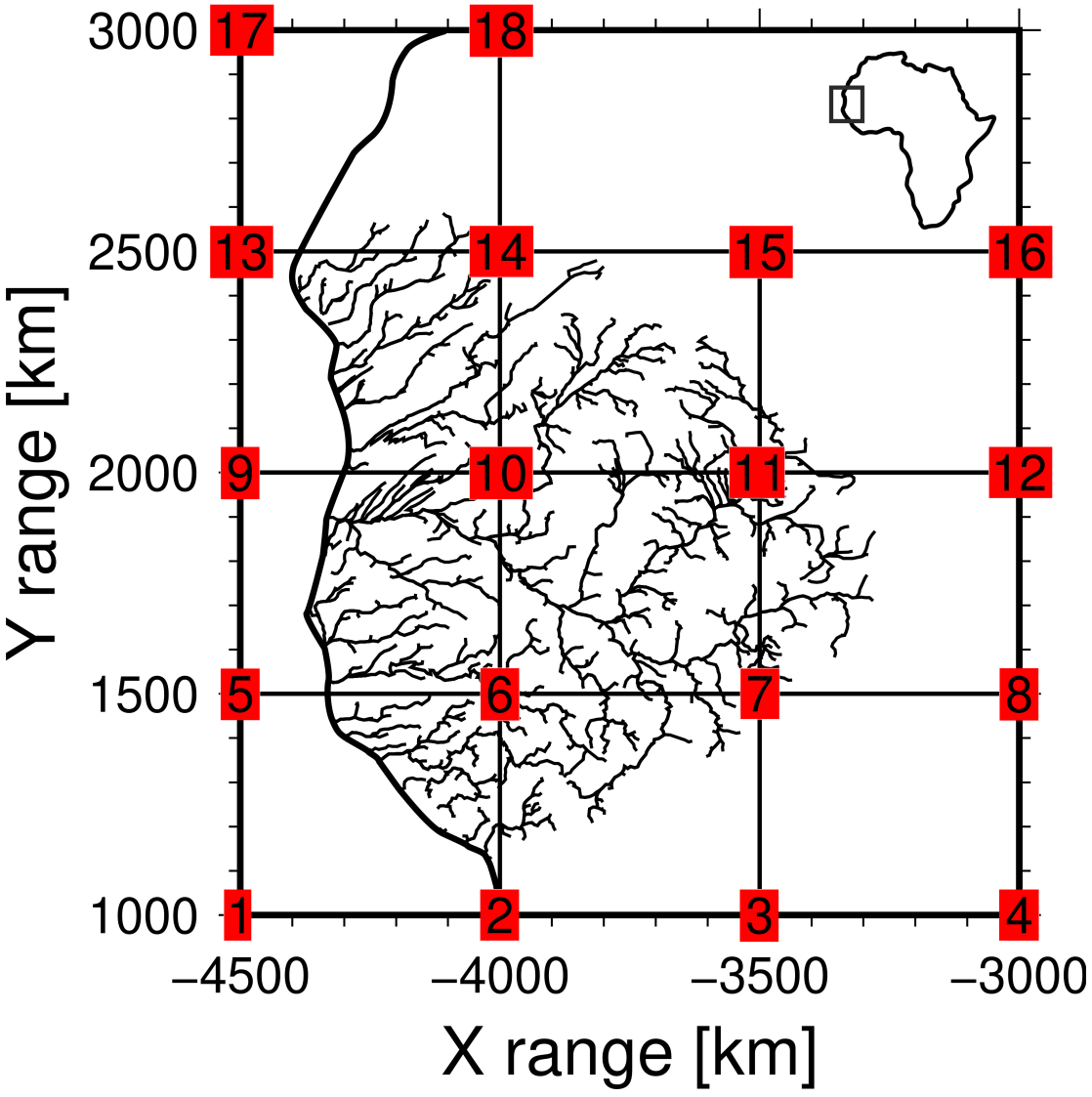


Figure 26: **Distribution of vertices in inverse model for Mauritania & Senegal**. Black lines = modelled rivers; red numbered circles = position of vertices where uplift is input into the model. X and Y are plotted in kilometres. Uplift rate at each point along a river is linearly interpolated from four surrounding vertices.

When the matrix M in Equation (4.26) has fewer rows than columns, the linear inverse problem becomes underdetermined. As a result, it is necessary to exploit a damped least squares approach. After Rudge et al. (2015), Equation (4.27) is minimised:

$$|M\mathbf{U} - \mathbf{z}|^2 + \lambda_S^2|S\mathbf{U}|^2 + \lambda_T^2|T\mathbf{U}|^2 \tag{4.27}$$

subject to $\mathbf{U} \geq 0$. This is a non-negative least squares problem. The smoothing parameters λ_S and λ_T control the regularisation of this problem. The matrix S represents spatial smoothing and is given by:

$$|S\mathbf{U}|^2 = \int_S \int_{t=0}^{t_{max}} |\Delta U|^2 dt dS \tag{4.28}$$

Matrix T represents temporal smoothing and is given by:

$$|T\mathbf{U}|^2 = \int_S \int_{t=0}^{t_{max}} \left|\frac{\partial U}{\partial t}\right|^2 dt dS \tag{4.29}$$

Whereby the parameters λ_S and λ_T are chosen by analysing the trade-off between smoothness and misfit (Parker, 1994; Rudge et al., 2015). Misfit, normalised by maximum misfit is calculated as a function of spatial smoothing, and normalised misfit is calculated as a function of temporal smoothing for 14700 African river profiles. Model regularisation is shown on Figure 27. The value of λ_S that produced the optimal inverse model is shown by the black arrow on Figure 27.

Prediction of solid sedimentary flux from drainage inversion

If it is assumed that erosion due to uplift is purely fluvial (i.e. hillslopes are not included) and produces both solid and solute sediment loads, the area of rock eroded from rivers within a drainage network due to uplift can be determined to calculate the sedimentary flux history of the drainage basin. The total area of rock eroded, $Q_s(t)$, is equated to the erosive term given by Equation (4.2), such that:

$$Q_s(t) = \int_0^L -vA(x)^m \left(\frac{\partial z}{\partial x}\right)^n + \kappa \left(\frac{\partial^2 z}{\partial x^2}\right) dx \tag{4.30}$$

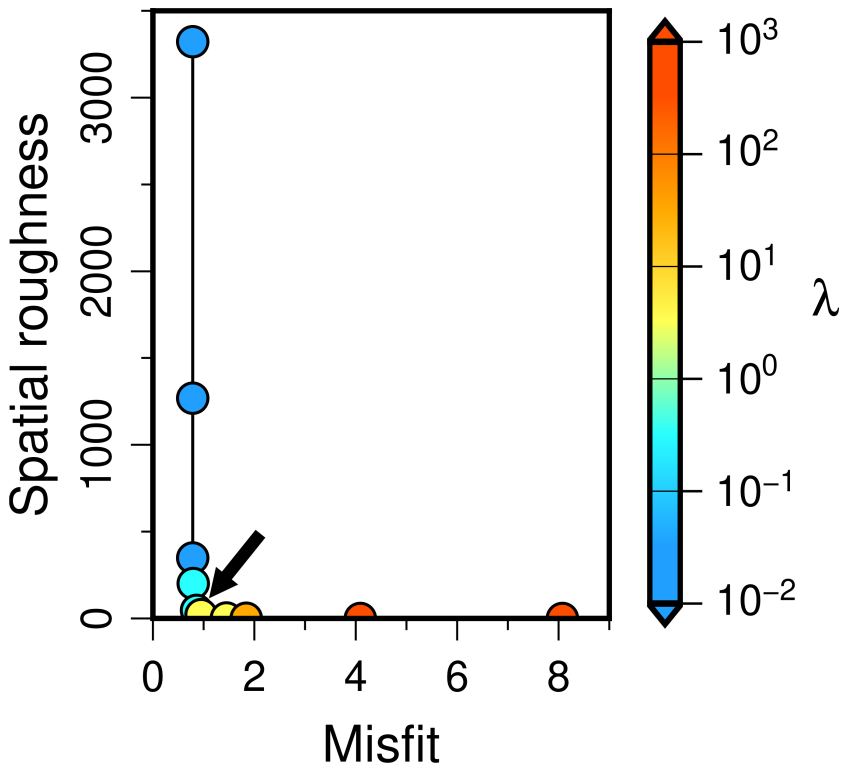


Figure 27: **Model regularisation**. Model misfit as function of spatial smoothing for series of inverse models. Coloured circles = residual misfit for a suite of inverse models run with different values of damping controlled by the value of λ (see e.g. Rudge et al., 2015). Black arrow = optimal (i.e. smoothest best-fitting) model. Residual rms misfit for optimal inverse model = 0.81.

where L is the total length of the river (e.g. Stephenson et al., 2014). Predicted patterns of sedimentary flux calculated using drainage inversion were compared to observations of solid sedimentary flux for the first time in this study for the Mauritanian basin in order to 'close the loop' between dynamic subsidence, continental uplift and sedimentary deposition to West Africa's passive margin.

4.3 Independent geological constraints for African uplift

Measurements of African continental uplift obtained form independent geological data must be used to calibrate the stream power erosional model and test the reliability of predictions of uplift calculated using the inverse numerical

method described in the previous section. In this section, independent geological data from across the African continent are reviewed. Observed continental uplift rates and methodologies are shown on Figure 28 and Table 4.

4.3.1 Southern Africa

South Africa

High elevations consequent upon the central position of Southern Africa in Gondwana prior to rifting in the Late Jurassic/Early Cretaceous possibly led to the survival of a major topographic feature known as the Great Escarpment (see Figure 11 in Partridge, 1998). Episodes of tectonically driven regional uplift across Southern Africa following the break-up of Gondwana has led to the preservation of escarpments that reflect three major erosional cycles. Partridge and Maud (1987); Partridge (1998); Partridge and Maud (2000) use a variety of methods to correlate the resultant erosional surfaces and pleneplains warped by subsequent uplift across Southern Africa from Cretaceous–Recent times. Occurrences of features such as kaolinisation of soil underlying post-Mesozoic stratigraphy and the development of pedocretes underlying post-Miocene bedrock are used to identify and correlate erosional surfaces. The Late Cretaceous saw Southern Africa transected by a major planation cut at two levels above and below the Great Escarpment, which Partridge and Maud (1987) name as the 'African Surface'. This surface was generated by the multi-phase cycle of Cretaceous erosion and forms a readily identifiable datum across the high plains because of the widespread preservation of deep weathering and massive cappings of laterite and silcrete on remnants which have survived later dissection (Partridge and Maud, 1987; Partridge, 1998). Onshore erosion in the this cycle was responsible for the marine terrigenous sedimentation which occurred throughout much of the Cretaceous and the Palaeocene. The resulting surface can be projected from the coastal hinterland across the top of these marine sequences (Partridge and Maud, 1987). Bewteen 150–300 m of uplift during the Miocene tilted the continent slightly to the west and initiated a new landscape cycle, resulting in the formation of an erosional surface which Partridge and Maud (1987); Partridge (1998); Partridge and Maud (2000) name

as the 'Post African I' surface. Palaeontological evidence supports the conclusion that this period of uplift ceased in the latter part of the Early Miocene and had a duration of 15–16 Ma (Spies et al., 1963; Hendey, 1978; Dingle and Hendry, 1984; Partridge and Maud, 1987). Age constraints are provided by associated fluvial deposits in the Koa Valley, the lower Orange River, and in the coastal hinterland of Namibia contain terrestrial faunas which date to between 19 and 17 Ma (Corvinus and Hendey, 1978; De Wit, 1993; Pickford et al., 1995, 1996; Partridge, 1998). This was followed by a period of major regional uplift from Pliocene–Recent times that warped the Southern African landscape and the beginning of the present erosional cycle identified by Partridge and Maud (1987); Partridge (1998); Partridge and Maud (2000) as the 'Post African II' cycle. Data from this study supports Partridge (1998)'s assertion that evidence for the extent of this deformation is provided by the longitudinal drainage profiles of major rivers of the southeast African coast. These are convex upward (Figure 24), clearly and consistently reflecting the influence of recent uplift and warping in an area where similarly pervasive structural and lithological controls are absent. Age constraints are provided by fossils and artefacts recovered from alluvial terraces eroded into rivers in the region, with the best example being of the lower Vaal River, South Africa (Partridge, 1998). Present-day elevations of marine terrace deposits give Cenozoic uplift rates ranging from 0.003 to 0.016 mm a^{-1} (see Table 4). There is a near linear relationship between the current elevations of the localities Pato's Kop, Birbury, & Need's Camp and their distance from the present coast, whose gradient corresponds closely with the mean gradient of the 'African' surface in this area (see Figure 23 from Partridge and Maud, 1987). Partridge and Maud (1987); Partridge (1998); Partridge and Maud (2000)'s results add further support to a tectonic explanation for the uplift that raised them to their present altitudes.

Erlanger et al. (2012) use radiometric dating of cosmogenic isotopes to determine Late Neogene uplift rates of South Africa. Burial dating relies on the radioactive decay of ^{26}Al and ^{10}Be in a rock that was once exposed but is now buried. In this case, nuclide concentrations (N_i) can be expressed as the sum of a decayed inherited component ($N_{i,inh}$), and the integrated postburial production ($P_{i,postburial)}$), such that:

$$N_i = N_{i,inh} e^{-\frac{-t}{\tau}} + e^{-\frac{t}{\tau}} \int P_{i,post-burial}(t) e^{\frac{t}{\tau}} dt \tag{4.31}$$

where τ represents the radioactive mean life, and the subscript i represents either ^{26}Al or ^{10}Be. The integral in Equation 4.31 depends on many factors, including depth of burial, erosion rate or deposition rate after burial, density of the overburden, and any other changes in production rate over time. Equation 4.31 is therefore underconstrained and requires simplification to solve (Erlanger et al., 2012). Erlanger et al. (2012) address this problem by using the isochron method, which uses the variation in measured ^{26}Al and ^{10}Be in a group of samples to solve explicitly for the postburial component common among them (see their Equations $3 - 8$ for detailed methodology).

At Greenwood Park in Durban, South Africa (see Table 4), gravel collected from a marine terrace exposed during the construction of a railway station was sampled and used to calculate an uplift rate. This marine terrace is correlative to a prominent but previously undated marine terrace that extends across the southeastern coast at 65 ± 5 m above sea level (Davies, 1970, 1971). The age of gravel collected from the Greenwood Park marine terrace is 4.47 ± 0.87 Ma, giving an uplift rate of 0.016 ± 0.003 mm a^{-1} (Table 4).

Roberts and Brink (2002) used shallow marine deposits and associated aeolianites to calculate the ages of strandlines from Saldanha and Hondeklip Bays on Southern Africa's southwestern coastline in Namaqualand. A northward trending, fossil dune system (Prospect Hill Formation) extends for ~ 20 km parallel to the coast north of Saldanha. The fossil content, geological context and correlation with global eustatic sea level curves indicate ages ranging from Middle Miocene to Plio–Pleistocene.

Three strandlines are identified by Roberts and Brink (2002), ranging in age from 18–8 Ma, 5 Ma and 2.1 Ma. Uncertainty is due to conflicting biostratigraphic information recovered from the Miocene section of the Prospect Hill Formation. Fossil eggshell fragments of the giant struthious bird *Diamantornis wardi* recovered from three palaeosols in the Prospect Hill Formation give an absolute age of 11 ± 1 Ma, constrained by quantitative radiometric data (Senut and Pickford, 1995; Pickford, 1998). However, a Late Middle Miocene stillstand during terminal Supercycle TB2 of Haq et al. (1987) left a veneer of marine

sediments up to 40 m above mean sea level at Prospect Hill near Saldanha Bay. These marine deposits are equated with the latter interval of the Early to Middle Miocene (18 to 8 Ma) 90 m high sea level cycle of Namaqualand. The warm water molluscan species *Fissurella robusta*, *Nucella praecingulata* and *Triumphis dilemma* occur commonly in the Mio-Pliocene 50 m high sea level cycle of Namaqualand, while *Burnupena aestus* is unique to this unit thus giving an age of 5 Ma (Kensley, 1985; Kensley and Pether, 1985; Pether, 1994; Roberts and Brink, 2002). A 25 m strandline exposed in a 70 m sedimentary succession ~ 2 km southwest of Postpect Hill (named the Lower Quarry in Roberts and Brink, 2002) contains the bivalve *D. rogersi* and other molluscans that relate to the 30 m transgressive/regressive marine deposits of Namaqualand. The associated aeolianites are banked up unconformably against the Prospect Hill Formation and contain a fragmentary mammalian fauna that suggest a Plio-Pleistocene age of 2.1 Ma. The global eustatic sea level curve of Haq et al. (1987) shows highstands at ~ 2 Ma, with which the 25 m high sea level cycle is correlated (Roberts and Brink, 2002). The ages of strandlines correlated across Namaqualand provide constraints on uplift at Saldanha Bay and Hondeklip Bay in South Africa. Late Neogene uplift rates at Saldanha Bay vary between $0.014 - 0.02$ mm a^{-1} and at Hondeklip Bay vary between $0.008 - 0.014$ mm a^{-1} (see Table 4).

Namibia

Van der Wateren and Dunai (2001) present evidence from in-situ cosmogenic ^{21}Ne dating of pediment surfaces, river surfaces and bedrock benches to constrain the ages of erosional surfaces and the incision rate of the Kuiseb River, Namibia, between 2.8–0.4 Ma. Van der Wateren and Dunai (2001)'s sampling procedure and method of measuring amalgamated paired samples (Repka et al., 1997) allowed the calculation of meaningful exposure ages for depositional terraces. Their results indicate that major late Neogene incision occurred at ~ 2.8 Ma in the central Namib west of the Escarpment, slowing down or stopping in the early to mid Pleistocene, after or before ~ 1.3 Ma at a distance of ~ 100 km from the river mouth, and at or before ~ 0.4 Ma 100 km further upstream. Since canyon downcutting to depths of 100–250 m below the highest

terrace surface started at 2.8 Ma and terminated between 1.3 Ma at 100 km from the coast and 0.4 Ma at 200 km from the coast assuming minimal erosion of the river-cut surfaces, Van der Wateren and Dunai (2001) estimate that the Kuiseb River incised at a rate of 40–160 m Ma^{-1} during the early to mid Pleistocene. These values provide uplift rates of 0.01 ± 0.06 mm a^{-1} for the erosional surface produced between 2.8–0.4 Ma (Table 4).

4.3.2 Western Africa

Angola

Pleistocene interglacial palaeoshorelines of the Lobito-Benguela & Mossarnedes region of Southern Angola were radiometrically dated by Giresse et al. (1984) using ^{14}C, ^{230}Th/^{234}U and ^{231}Pa/^{231}U ratios obtained from fossils. Because of its geomorphological characteristics, the Benguela coast is interpreted to be a typical coastal-terrace shoreline as defined by Bloom et al. (1974) & Guiraud et al. (2010). Radiometric dating of the molluscs *Arca senilis* (samples AN32, AN57-1 and AN47), *Spisula nivea* (sample AN40-2) and *Conus pulcher* (sample AN27) are used to constrain the ages of interglacial palaeoshorelines (Table 4). The majority of the samples analysed were composed of several fragments or individuals of the same species of mollusc, except samples AN 27 and AN 57-1 which consisted of single shells. Giresse et al. (1984) largely followed the radiochemical procedure described by Ku (1966). Each sample was completely dissolved, and radioactive tracers ^{232}U–^{228}Th in radioactive equilibrium, and ^{233}Pa were used to determine the concentration of each isotope. U, Th and Pa were purified and separated and their activities measured by alpha spectrometry. The abundance of calcite in each sample was determined by X-ray diffractometry. Except for sample AN27 which had a calcite concentration of 40%, the samples analysed displayed very little evidence of recrystallisation (calcite concentration $<$5%) (Giresse et al., 1984). The radiometric ages of these Pleistocene palaeoshorelines and their present elevation indicate that the Upper Pleistocene marine terraces match up with the different Late Pleistocene interglacial high sea-levels (Giresse et al., 1984; Guiraud et al., 2010). Guiraud et al. (2010) document Upper Pleistocene tectonic uplift rates in mm ka^{-1} of the

coastal plain of the Benguela Basin on the basis of the graphical method from Merritts and Bull (1989). This method allows tectonic uplift and eustasy to be decoupled. Upper Pleistocene uplift rates of Southern Angola vary between 0.11–0.39 mm a^{-1} (Table 4).

Mauritania and Senegal

U/Th dating of exposed marine carbonate terraces on the Mauritanian and Senegalese coast by Giresse et al. (2000) provides a constraint for Quaternary uplift rates in West Africa. Outcrops located at Tin Oiech, south of the Boutilimit road, approximately 15 km east of Nouakchott ($18°03'10''$ N $15°49'35''$W) and Tafoli, north of Nouakchott were sampled by Giresse et al. (2000) and fossils were used for absolute dating. At Tin Oiech, Holocene and Pleistocene lithofacies are fairly well exposed in closed depressions between aeolian dunes, and correspond either to marine flooding or to sabkhas. At Tafoli, successive outcrops of marine deposits from the Early Pleistocene to the Late Pleistocene were recognised along the SW–NE road from Nouakchott to Akjout, Mauritania (Giresse et al., 2000). Molluscs recovered from the Inchirian formation at Tin Oiech include *Gryphea gasar* and at Tafoli and *Anadara senilis* at Tafoli. The molluscs recovered from the Aïoujian formation include *Anadara senilis* at Tin Oiech and *Cardium cymbium* at Tafoli. The mollusc shells collected were analysed in several steps. First, bioclasts and cements in thin sections were observed. This was followed by detailed observations with scanning electronic microscope. Each point was linked to chemical analyses by dispersion of energy. Particles were isolated by a dental drill and analysed by X-ray diffraction. A detailed petrographic and mineralogical study was undertaken to identify the most suitable 'shelly' material for radiometric dating (^{14}C and U/Th). Th/U disequilibrium was measured by alpha spectrometry. Classical separations and purifications of U and Th isotopes, as summarised by Lally (1992), were followed. A triple spike solution containing ^{232}U, ^{228}Th and ^{234}Th (Causse and Hillaire-Marcel, 1989) was used, in order to check the generally assumed equilibrium between ^{232}Th and ^{228}Th (Giresse et al., 2000). Giresse et al. (2000)'s results distinguish four successive transgressions separated by three regressions. The transgressive deposits show progressive basinwards-

stepping of shorelines, implying a progressive uplift of the continent and a decrease in the extent of the widespread marine gulfs from the Early Pleistocene to Holocene (Giresse et al., 2000). At Tin Oiech, *Anadara senilis* gives an age of 241 ± 15 ka for an elevation of $6 - 10$ m and and *Gryphea gasar* gives and age of 122 ± 5 ka for an elevation of $4 - 6$ m. At Tafoli, *Anadara senilis* gives and age of 258 ± 24 ka for an elevation of $6 - 10$ m and *Cardium cymbium* gives an age of 99 ± 16 ka for an elevation of $4 - 6$ m (Giresse et al., 2000). These results give uplift rates of 0.037–0.041 mm a^{-1} at Tin Oiech and 0.032–0.057 mm a^{-1} at Tafoli (Table 4).

4.3.3 North Africa

Morocco

Meghraoui et al. (1998) use the U/Th method to date 37 mollusc samples recovered from from Quaternary marine terraces of the South Atlas Thrust Front near the Agadir seismogenic region of Morocco. They argue that although the dating of molluscs by U-series is problematic (Stearns and Thurber, 1965; Kaufman et al., 1971), the assumption of reliable ages is supported by consistent results after several chemical analyses of the same sample, no evidence of recrystallisation indicated by X-ray analysis, and the fact that the ages are consistent with the conventional succession of Quaternary marine deposits (Meghraoui et al., 1998). Their results yield two main groups of ages for marine terraces and can be correlated with oxygen-isotope stages 5 and 7. According to the geological succession of Quaternary marine deposits and U-Th dating, the two groups of marine terraces are correlated with sea-level altitudes at $+6$ m and -10 m that correspond to eustatic highstands 5.3 and 7.3 (Chappell and Shackleton, 1986). At Arhesdis, located on the Kasbah anticline, a U/Th age of 115 ± 7.5 ka at an elevation of 18 ± 0.5 m is observed. This gives a quaternary uplift rate of 0.16 ± 0.1 mm a^{-1} (Table 4) and is representative of the average uplift rate of 0.1–0.2 mm a^{-1} calculated by Meghraoui et al. (1998) for the region.

Tunisia

Elmejdoub and Jedoui (2009) identified a series of Middle–Late Pleistocene marine terraces along the coast of the Cap Bon peninsula, Tunisia, near Somaa. Radiometric dating (U/Th) and biostratigraphic data are used to constrain the ages of the marine platforms and calculate values for Quaternary coastal uplift rates. Three marine terraces are identified, PfI, PfII and PfIII whereby PfI is the oldest and highest platform and PfIII is the youngest and lowest platform.

The youngest unit, PfIII, is located closest to the present-day coastline between an elevation of 40–6 m. The first and older lithostratigraphic unit within the platform PfIII is characterised by siliciclastic fine-to-medium grained sands rich in the marine fossil *Cardium*. Marine quartzose sands and lagoonal silts are separated from the overlaying sequences by reddish continental deposits including shells of *Helix*. The second unit within PfIII consists of bioclastic and siliciclastic, fine–medium grained sands devoid of *S. bubonius*. The third unit within the platform PfIII is a conglomerate which contains an abundance of marine shells that grade into aeolian deposits characterised by fine grains, cross-bedded stratifications and fauna of continental gastropods, *Helix*. This unit is rich in *Cardium*, *Glycymeris*, *Cerithium* and *S. bubonius*. Elsewhere in Tunisia, U/Th dating on *Ostea* shells from carbonate-rich deposits found in the same stratigraphic position by Jedoui et al. (2003) give an average age of 120 ka. Hearty (1986) and Mauz et al. (2009) record radiometric ages of 127 ± 7 and 121 ± 10 ka from stratigraphically equivalent carbonate deposits located in central and northeastern Tunisia. These ages suggest that this platform dates from marine isotope stage MIS5e, thus providing an age constraint of 123 ka. The Pleistocene uplift rate for this locality is 0.19 ± 0.14 mm a^{-1} (Table 4).

Platform II is identified as a typical mixed association of an infratidal-to-intertidal stage and has an elevation of 58–50 m. Microfaunal analysis identified the presence of ostrachods and *A. beccarii*, *E. macellum*, *C. lobatulus*, *Rosalina globularis*, *S. depressa*, *Elphidium crispum* and *Quinqueloculina sp*. Optically-Stimulated Luminescence (OSL) dating of marine deposits located in the same stratigraphic position in central-eastern Tunisia attribute platform PfII to marine isotope stage MIS 7, providing an age constraint of 270 ± 29 ka (Mauz et al.,

2009). The Pleistocene uplift rate for this locality is 0.20 ± 0.04 mm a^{-1} (Table 4).

PfI is characterised by its surface being morphologically covered by a hard and thick calcrete horizon, and has an elevation of 118–73 m. Field investigations showed that the basal part of the Pleistocene sedimentary sequence consists of a conglomeratic layer unconformably overlying Miocene–Pliocene deposits and Early Quaternary continental red soils. The marine units associated with platforms PfI have no similar system elsewhere neither in northern, eastern or southern Tunisia. Their stratigraphic situation points to an age older than MIS 7. Elmejdoub and Jedoui (2009) tentatively suggest that this marine platform may be related to sea-level highstands of marine isotope stages MIS 9/11 and MIS 11/13, providing an age constraint of 450 ± 113 ka. The Pleistocene uplift rate for this locality is therefore estimated to be 0.24 ± 0.11 mm a^{-1} (Table 4).

4.3.4 East Africa

Odada (1996) identifies the Uhuru marine terrace, which is a narrow surface in the coral reef at Uhuru Farm and the low ground in the Malindi Bay, frininging the Mida Creek, Kenya, between an elevation of 2–6 m. Hori (1970) reports a minimum age of $26.5 + 1.3/-1.5$ ka for a coral head from Similani, located on the Uhuru marine terrace. The Pleistocene uplift rate for this locality is 0.16 ± 0.09 mm a^{-1}.

4.4 Results

Calculated uplift history of Africa

African uplift grows considerably over the last 30 Ma. There is significant growth of the Fouta-Djallon swell (West Africa), East African Rift system and of domal swells across central and southern Africa at rates of ~ 0.067, ~ 0.083 and ~ 0.07 mm a^{-1}, respectively, over the last 30 Ma. Since Neogene times, Southern Africa has been uplifted by between 1–2 km. The residual misfit between observed and theoretical African longitudinal river profiles is very

Locality	Map reference	Longitude	Latitude	Age [Ma]	Elevation [m]	Uplift rate [mm a^{-1}]	Methodology	Reference
Patos Kop	A	27.37	-33.34	44.85±10.95	130±0	0.003±0.001	1	Partridge and Maud (1987)
Birbury	B	27.62	-33.19	44.85±10.95	200±0	0.005±0.001	1	Partridge and Maud (1987)
Needs Camp	C	27.73	-33.09	44.85±10.95	400±0	0.096±0.002	1	Partridge and Maud (1987)
Bathurst	D	26.46	-33.74	4.47±0.87	400±0	0.093±0.018	1	Partridge and Maud (1987)
SW of Maputo	E	31.17	-27.35	15.5±5.5	900±0	0.057±0.018	2	Partridge (1998); Partridge and Maud (1987)
SW of Maputo	E	31.17	-27.35	3.57±1.76	600±0	0.222±0.109	2	Partridge (1998); Partridge and Maud (1987)
Durban	F	29.52	-30.02	15.5±5.5	1150±0	0.073±0.023	2	Partridge (1998); Partridge and Maud (1987)
Durban	F	29.52	-30.02	3.57±1.76	900±0	0.334±0.165	2	Partridge (1998); Partridge and Maud (1987)
Greenwood Park	G	31.02	-29.79	4.26±0.68	65±5	0.016±0.003	3	Erlanger et al. (2012)
East London	H	28.28	-32.05	15.5±5.5	1100±0	0.070±0.022	2	Partridge (1998); Partridge and Maud (1987)
East London	H	28.28	-32.05	3.57±1.76	850±0	0.314±0.156	2	Partridge (1998); Partridge and Maud (1987)
E. of George	I	22.48	-33.76	15.5±5.5	400±0	0.025±0.008	2	Partridge (1998); Partridge and Maud (1987)
E. of George	I	22.48	-33.76	3.57±1.76	200±0	0.074±0.036	2	Partridge (1998); Partridge and Maud (1987)
S. of P. Nolloth	J	18.48	-30.40	15.5±5.5	250±0	0.016±0.005	2	Partridge (1998); Partridge and Maud (2000)
S. of P. Nolloth	J	18.48	-30.40	3.57±1.76	100±0	0.037±0.018	2	**?**) & Partridge and Maud (2000)
Saldanha Bay	K	17.96	-32.99	13±5	150±0	0.02±0.01	4	Roberts and Brink (2002)
Saldanha Bay	K	17.96	-32.99	5±0	100±0	0.02±0	4	Roberts and Brink (2002)
Saldanha Bay	K	17.96	-32.99	2.1±0	30±0	0.014±0	4	Roberts and Brink (2002)
Hondeklip Bay	L	17.27	-30.31	13±5	90±0	0.008±0.003	4	Roberts and Brink (2002)
Hondeklip Bay	L	17.27	-30.31	5±0	50±0	0.01±0	4	Roberts and Brink (2002)
Hondeklip Bay	L	17.27	-30.31	2.1±0	30±0	0.014±0	4	Roberts and Brink (2002)
Kuiseb R.	M	15.74	-23.34	1.6±1.2	175±75	0.1±0.06	5	Van der Wateren and Dunai (2001)
AN32	N	12.13	-15.20	0.3±0	31±1	0.11±0	6	Giresse et al. (1984); Guiraud et al. (2010)
AN32	N	12.13	-15.20	0.17±0	31±1	0.19±0	6	Giresse et al. (1984); Guiraud et al. (2010)
AN40-2	N	12.13	-15.20	0.13±0.01	15±0	0.114±0.01	6	Giresse et al. (1984); Guiraud et al. (2010)
AN57-1	O	13.42	-12.56	0.091±0.006	11±1	0.12±0.02	6	Giresse et al. (1984); Guiraud et al. (2010)
AN27	O	13.42	-12.56	0.071±0.007	28±3	0.39±0.08	6	Giresse et al. (1984); Guiraud et al. (2010)
AN47	O	13.42	-12.56	0.036±0.003	9±1	0.25±0.05	6	Giresse et al. (1984); Guiraud et al. (2010)
Tafoli	P	-15.05	18.82	0.099±0.016	5±1	0.054±0.019	7	Giresse et al. (2000)
Tafoli	P	-15.05	18.82	0.258±0.024	8±2	0.032±0.011	7	Giresse et al. (2000)
Tin Oueich	Q	-15.83	18.05	0.122±0.005	5±1	0.041±0.099	7	Giresse et al. (2000)
Tin Oueich	Q	-15.83	18.05	0.241±0.015	8±2	0.034±0.010	7	Giresse et al. (2000)
Arhesdis	S	-9.69	30.52	0.115±0.075	18±0.5	0.16±0.01	7	Meghraoui et al. (1998)
Somaa	S	10.78	36.54	0.45±0.113	96±2	0.24±0.11	8	Elmejdoub and Jedoui (2009)
Somaa	S	10.78	36.54	0.27±0.029	54±4	0.20±0.04	8	Elmejdoub and Jedoui (2009)
Somaa	S	10.78	36.54	0.123±0	23±17	0.19±0.14	8	Elmejdoub and Jedoui (2009)
Similani	T	39.58	-4.29	0.0265±0.0015	4±2	0.16±0.09	9	Hori (1970); Odada (1996)

Table 4: **Observed African uplift used to calibrate stream power erosional model**. Map labels of localities correspond to Figure 28. Methodology used to determine uplift rates is as follows: 1 = Biostratigraphic dating of marine terraces and correlation with warped peneplains; 2 = Biostratigraphic dating of river incision and $^{40}Ar/^{39}Ar$ dating of pedogenic rock; 3 = ^{26}Al & ^{10}Be dating of marine terraces; 4 = Biostratigraphic dating of strandlines; 5 = ^{21}Ne dating of fluvial incision rate between 2.8–0.4 Ma; 6 = $^{230}Th/^{234}U$, $^{231}Pa/^{231}U$ & ^{14}C dating of marine terraces; 7 = U-Th dating of marine terraces; 8 = Oxygen isotope stage (OIS) correlation of marine terraces, with U-series calibration from Jedoui et al. (2003); 9 = ^{14}C dating of marine terraces.

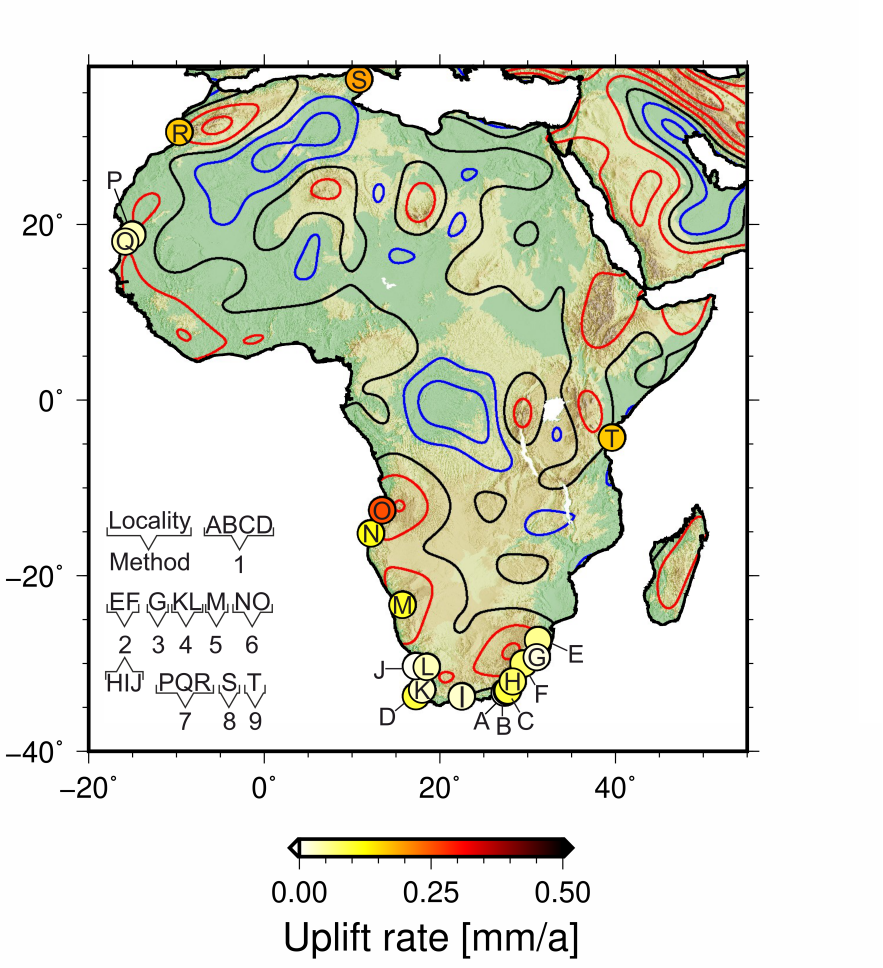


Figure 28: **Independent constraints of continental uplift.**. Values of uplift rates listed in Table 4 plotted on present-day African topography. Red/blue lines = positive and negative free air gravity anomaly contours at 20 mGal intervals, respectively. Black lines = contour of zero free air gravity anomalies. Methodology used for each locality is described in the caption of Table 4.

low (rms misfit = 0.81; Figures 29 & 30). Predicted and observed uplift rates calculated from independent geologic constraints match within error (Figure 32). Model coverage is greatest for the largest river systems and decreases with age.

Calculated uplift history of Mauritania & Senegal

Significant Neogene–Recent uplift is recorded in the hinterland of rivers draining the Mauritanides fold belt, eastern Mauritania, northern Mauritania and the Fouta-Djallon swell. The Mauritinides fold belt, northern Mauritania and Senegal have been uplifted by between 0.5–1 km since 30 Ma. Up to 2 km of uplift is recorded at the Fouta-Djallon swell (Figure 31). < 500 m of uplift is recorded in the Mauritinides fold belt and northern Senegal between 30–15 Ma. This is followed by significant and rapid uplift across northern Mauritania, the Mauritinides fold belt, Senegal and Fouta-Djallon from 15 Ma–Recent. Significant uplift of < 500 m across the region occurs from 5 Ma–Recent. Theoretical drainage profiles calculated from the cumulative uplift history shown on Figures 30 & 31 from the Senegal catchment closely match observed longitudinal river profiles (Figure 29).

Prediction of Neogene sedimentary flux from drainage inversion

Values of predicted sedimentary flux calculated using Equation (4.30) are an area flux, and do not correspond to the absolute values of observed sedimentary flux calculated from isopach volumes (Chapter 2). However, the temporal pattern of sedimentary flux to the Mauritanian basin can be determined by inverting Mauritanian/Senegalese rivers. The predicted Neogene–Recent sedimentary flux calculated using Equation (4.30) for rivers draining West Africa's passive continental margin into the Mauritanian basin increases during two distinct periods. The first increase in sedimentary flux occurs between $22 - 16$ Ma, whereby sedimentary flux increases from 38 to 43×10^3 m^2 Ma^{-1}. A significant increase in sedimentary flux occurs at ~ 8 Ma and continues to increase to Recent times.

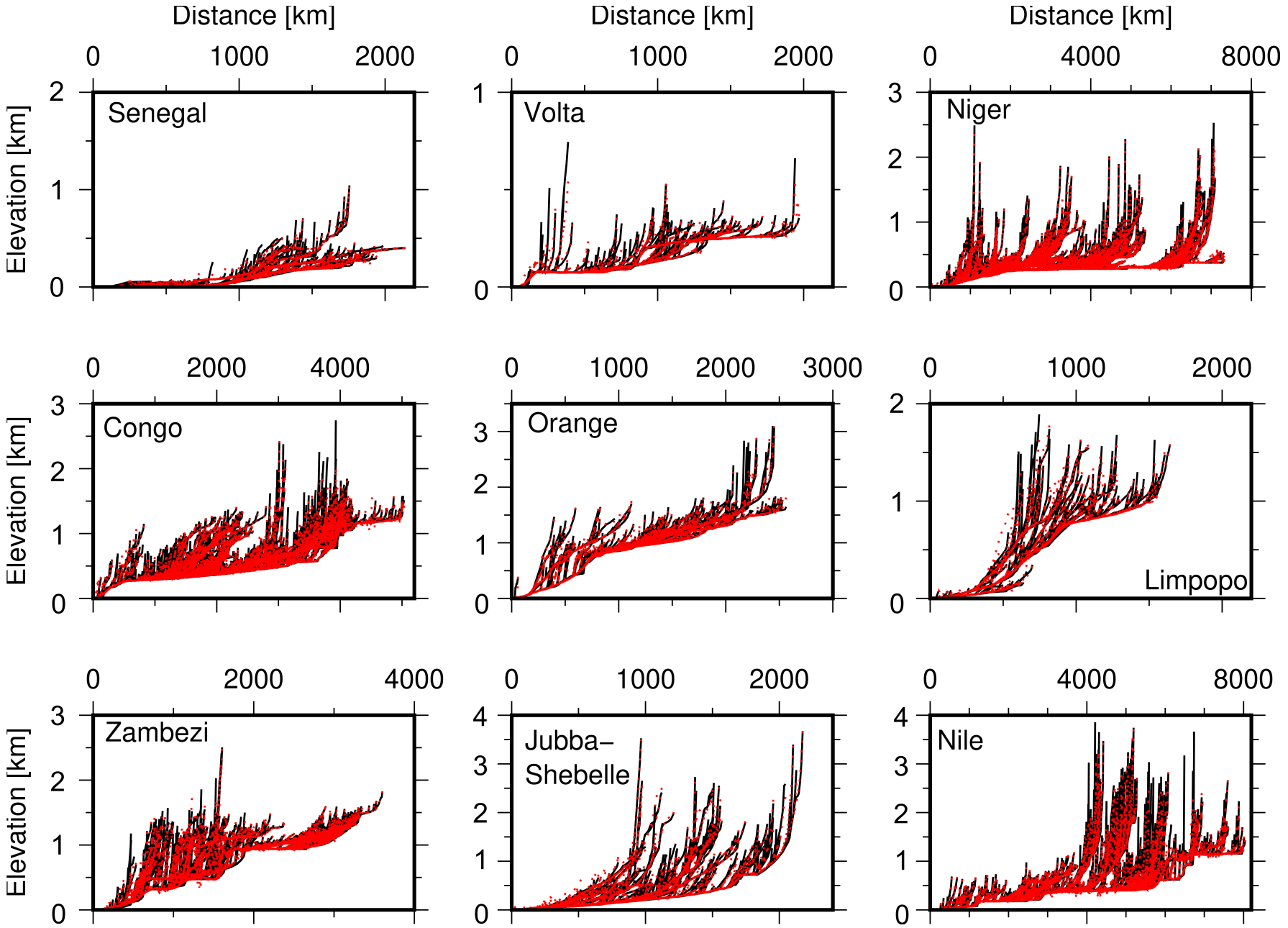


Figure 29: **Inverse modelling of African river profiles arranged by catchment**. Results yield spatial and temporal patterns of cumulative uplift shown in Figure 30. Black lines = longitudinal river profiles extracted from SRTM DEM; red-dotted lines = best-fitting theoretical river profiles generated using uplift history shown in Figure 30. Residual RMS misfit = 0.81.

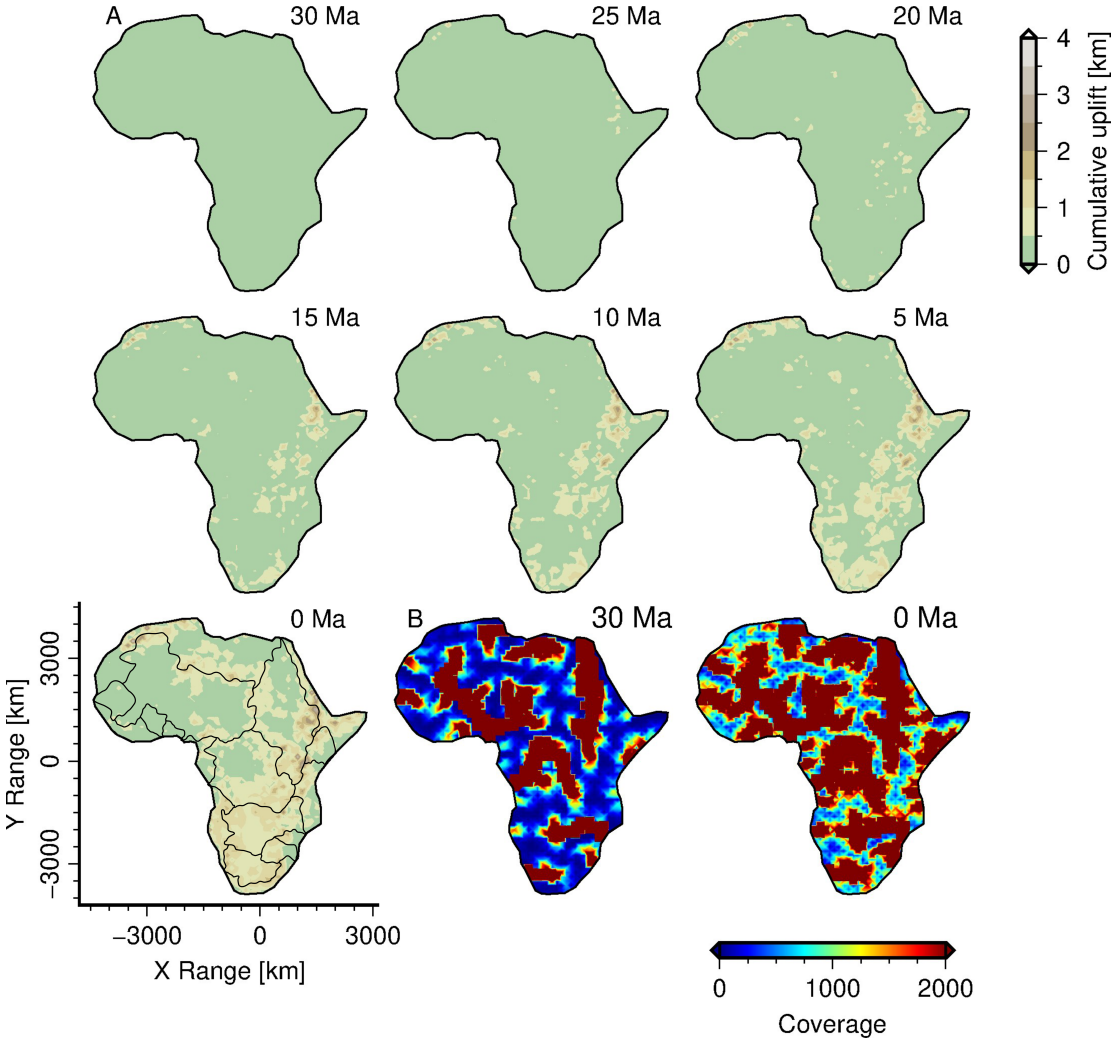


Figure 30: **Calculated Cumulative African uplift from** 30 **Ma to Present**. (A) Calculated spatial and temporal pattern of cumulative uplift from inversion of 14700 river profiles. Black polygons on bottom left panel = present-day African drainage divides. (B) Coverage in model matrix corresponding to a given uplift node at 30 Ma and 0 Ma.

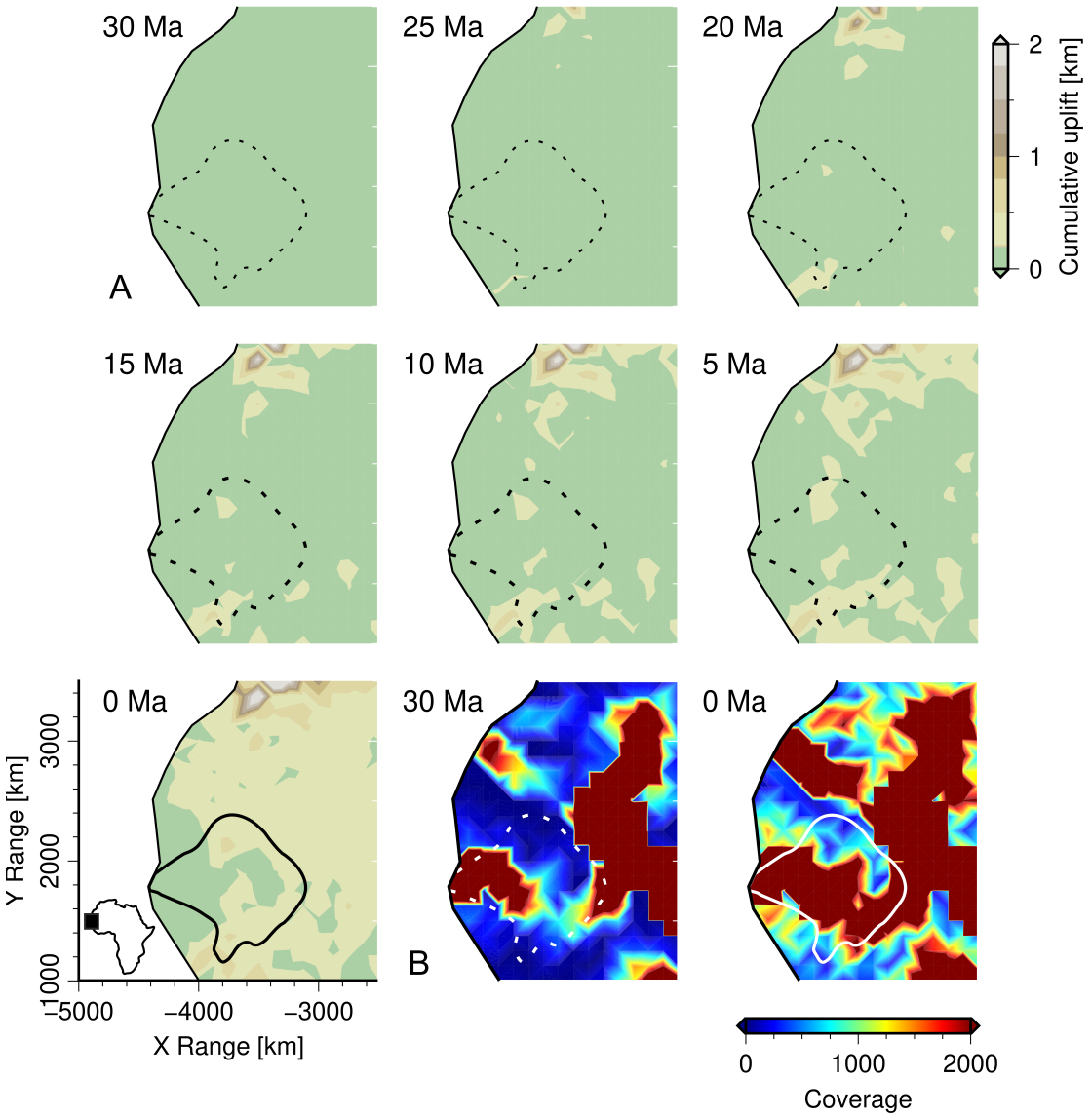


Figure 31: **Calculated uplift histories for Mauritania & Senegal**. (A) Calculated spatial and temporal pattern of cumulative uplift from inversion of river profiles from Mauritania & Senegal. Black/white polygons = position of Senegal drainage basin, solid line = present day and dashed lines = projected position of Senegal drainage basin. (B) Coverage in model matrix corresponding to a given uplift node at 30 Ma and 0 Ma.

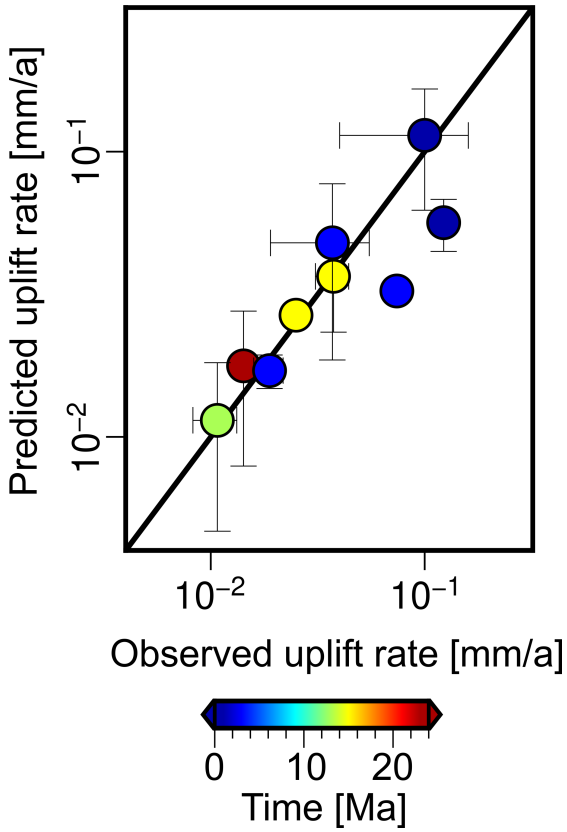


Figure 32: **Observed versus calculated uplift rates for Africa**. Comparison of independent and calculated uplift rates for Africa. Circles = weighted mean values of uplift rate where colour indicates age. Vertical/horizontal lines with bars = uncertainties.

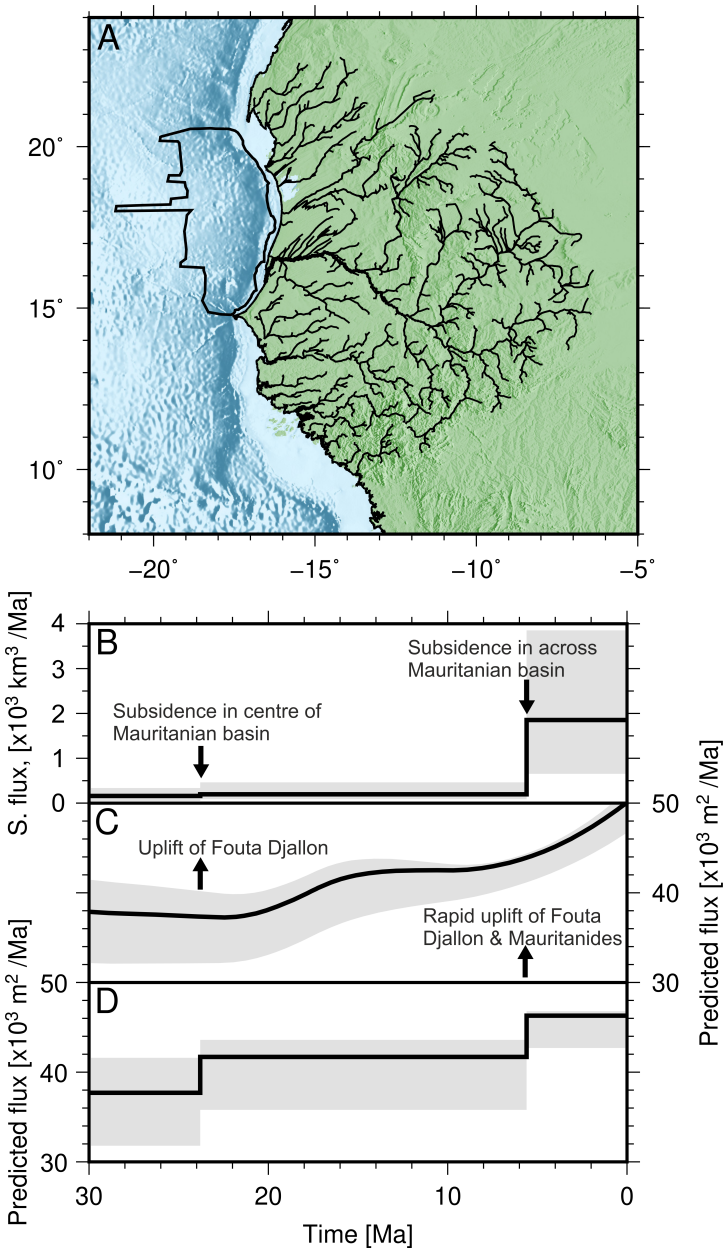


Figure 33: **Prediction of Neogene sedimentary flux from drainage inversion**. (A) Drainage extracted using SRTM DEM from Mauritania & Senegal. Black polygon = study area in Mauritanian basin (B) Observed solid sedimentary flux history of the Mauritanian basin (from Chapter 2) (C) Prediction of Neogene two-dimensional area flux of sediments eroded from Mauritania & Senegal calculated using Equation (4.30). (D) Predicted Neogene sedimentary flux values from (C) averaged between mapped stratigraphic horizons 23.8, 5.6 and 0 Ma. Grey band = uncertainty calculated by varying drainage area by $\pm 50\%$.

4.5 Discussion

Three central results are discussed here. Firstly, the punctuated history of sedimentary flux to northwest Africa's passive margin is reviewed. Secondly, the application of continental drainage inversion to calculate uplift rate histories and predict patterns of sedimentary flux to Africa's passive margin basins is examined. Finally, the implications of calculated uplift rate histories and predicted sedimentary flux for the evolution of African topographic support and mantle convection are examined.

Northwest Africa's passive margin stratigraphy

As Figures 6 & 7 show, Jurassic to Lower Cretaceous-aged carbonates are intersected by several wells along the northwest African margin, including over 700 m of Berriasian-aged lagoonal carbonates at Wells Loup De Mer-1, MBour-1, Ndiass-1 and Dakar Marin-2 in Senegal (Vear, 2005). In addition, several wells intersect thick carbonates of this age in the Tarfaya and Aaiun Basins to the north in Morocco and Western Sahara, respectively (e.g. Cap Juby-1). A Jurassic carbonate shelf has also been identified on the conjugate Atlantic Seaboard of the USA (Vear, 2005).

With the exception of the northeast continental margin, Africa was separated from surrounding continents by the beginning of the Late Cretaceous (e.g. Janssen et al., 1995). Cenomanian marine deposition is recorded onshore in northwest Morocco, northern and eastern Africa (e.g. Sahagian, 1988). High subsidence rates in the MSGBC and Gabon Basins during the Campanian–Maastrictian were probably generated by spreading between the central, equatorial and southern sectors of the Atlantic ocean (Fairhead, 1988b,a; Daly et al., 1989; Janssen et al., 1995). The lack of Upper Cretaceous prograding clinoforms and clastic sedimentation recorded at Wells A, B and H are probably partially related to rapid Cretaceous subsidence (Janssen et al., 1995). The pattern of decreasing solid sedimentary flux and increasing Paleogene carbonate production in the Mauritanian basin indicates that rates of continental clastic efflux were probably low. These observations are consistent with the distribution of indurated Paleoegene laterites and lateritic gravels onshore, which indicate that

Cretaceous–Paleogene topographic gradients and physical erosion rates were low (Nyagah, 1995; Salman and Abdula, 1995; Séranne and Nzé Abeigne, 1999; Burke and Gunnell, 2008; Rouby et al., 2009; Ismail et al., 2010; Grimaud et al., 2018). High sea-level, intense inland weathering and preferential deposition of phosphates and carbonates dominated the intercratonic and marginal basins of West Africa during the Paleocene-Eocene (Grimaud et al., 2018). Offshore deposition in the Mauritanian basin during this time is dominated by carbonates and erosion in the central part of the basin around Well D.

The base Miocene unconformity, 23.8 Ma, marks a significant change in sedimentation rate and facies in the Mauritanian basin. A major change from carbonate to clastic deposition is clearly seen across the entire basin from the Miocene until the present day. Results from Chapter 3 show that 0.4–0.8 km of Neogene water-loaded subsidence is observed in the centre of the Mauritanian basin. Subsidence histories, measured ocean-age depth residuals, magmatic histories and shear wave tomographic modelling suggest that the initiation and acceleration of mantle downwelling beneath the Mauritanian basin from Neogene–Recent times is responsible for the creation of accommodation. Continental drainage inversion results indicate that has this space been filled by sediments eroded from the adjacent uplifting West African passive margin.

Clastics versus carbonates, continental uplift & offshore sediment deposition

An important question is what caused the change from carbonate to clastic sedimentation that occurred in the Mauritanian basin at ~ 23 Ma? Small increases in the delivery of clastic material to continental margins can greatly reduce the efficacy of carbonate production (e.g. Walker et al., 1983). In general, efflux rates vary between different drainage basins and are controlled by drainage area and relief, and are moderated by other variables (e.g. climate, runoff; Milliman and Syvitski, 1992). The relatively high volumes of Miocene–Recent clastic rock mapped throughout the Mauritanian basin indicate that delivery of clastic material to the margin increased by an order of magnitude. An obvious source of this clastic material is uplift and erosion of the continental

hinterland. Grimaud et al. (2018)'s calculated clastic efflux to the Senegambia drainage basin follows the same trend which I observe in the Mauritanian basin further north, whereby solid sedimentary flux increases substantially from Eocene–Present times (Figure 11). This indicates that drainage north of the Senegambia catchment (i.e. that which drains into the Mauritanian basin) stabilised during Paleocene times, similar to the nearby Senegambia and Niger catchments (Grimaud et al., 2018).Significant increases in solid sedimentary flux to the Senegambia and Mauritanian basins occurred during the last $\sim$5 Ma. From a tectonic point of view, it is surprising that uplift and clastic flux should increase so dramatically long after continental break up has occurred. However, long wavelength free air gravity anomalies, positive residual ocean age-depth measurements, radial drainage patterns and calculated histories of uplift indicate that the Fouta Djallon swell also grew (and was denuded) in response to regional sub-plate support during the last $\sim$ 30 Ma. Inversion of drainage patterns from across Africa suggest that this phase of clastic flux was accompanied and probably controlled by the acceleration in the growth of the Mauritinides and Fouta Djallon topographic swell.

Importantly, the signal of increased clastic sedimentary flux received by the Mauritanian basin from $\sim$ 23–5.6 Ma is concomitant with 0.5–1 km of continental uplift in the hinterland of rivers draining into the centre of the basin. Calculated uplift histories indicate that at between $\sim$ 22–8 Ma, uplift in Mauritania/Sengal was largely restricted to the central Mauritinides and around the coast of northern Mauritania. The main Senegal river and rivers in northern Mauritania drain sediment from this region into the centre of the Mauritanian basin. Between 5.6–0 Ma, observed sedimentary flux across the Mauritanian basin increased by an order of magnitude (Figure 33). This is concomitant with 1–2.5 km of calculated uplift across Mauritania, Senegal and Fouta-Djallon (Figure 31). The signals of increased offshore sedimentary flux (Chapter 2), offshore dynamic subsidence to the Mauritanian basin (Chapter 3) and continental uplift in the sedimentary hinterland (this chapter) indicate that dynamic processes are responsible for controlling the sedimentary budget to the Mauritanian basin.

Are the changes in Neogene dynamic support and sedimentation observed in the Mauritanian basin observed elsewhere in Africa? It is widely accepted that Africa's domal swells have grown in response to mantle convective support during the last ~ 30 Ma (Holmes, 1944; Burke, 1996; Gurnis et al., 2000; Burke and Gunnell, 2008; Al-Hajri et al., 2009; Moucha and Forte, 2011; Paul et al., 2014; Rudge et al., 2015). Results from inverse modelling of continental drainage patterns suggests that most swells grew steadily from 30–5 Ma and accelerated during the last 5 Ma (Figure 30). This pattern is seen across eastern, central and southern Africa and is coeval with a significant increase in clastic sedimentation recorded at most major African deltas from Miocene times (e.g. Sestini, 1989; Nyagah, 1995; Salman and Abdula, 1995; Séranne and Nzé Abeigne, 1999; Anka and Séranne, 2004; Reijers, 2011; Paul et al., 2014). A significant increase in clastic flux at ∼23 Ma and at ∼5 Ma is documented at most of Africa's major deltas (e.g. Nile, Jubba-Shebelle, Zambezi, Limpopo; Walford et al., 2005; Said et al., 2015, Figure 34). These observations are consistent with the notion that uplift, subsidence and sedimentary flux to the Mauritanian margin are a manifestation of a continent-wide history of punctuated Cenozoic dynamic support.

Process governing sedimentation & denudation through time

The fact that large inventories of drainage can be successfully inverted at the continental scale to yield apparently meaningful uplift rate histories is surprising given the complexity of processes that are ultimately responsible for governing the evolution of longitudinal river profiles. Results indicate that the spatial and temporal pattern of regional uplift moderates long wavelength convexities along river profiles. The quality of fit between observed and calculated river profiles suggests that these convexities are systematically organised in accordance with a nonlinear stream power law. Furthermore, results from this study show that patterns of solid sedimentary flux to the Mauritanian basin can be accurately determined by inverse modelling of continental drainage and indicates that in this case, the dominant control on sedimentation to West Africa's passive margin is the evolution of its hinterland topography. However, it is important to note that inverse modelling makes several key assumptions.

Firstly, it is assumed that the drainage planform does not migrate significantly over time and therefore implies that the advective retreat of knickzones is the dominant physical process by which channels evolve since erosional diffusivity can range over seven orders of magnitude without adversely affecting the solutions obtained (e.g. Rosenbloom and Anderson, 1994; Roberts and White, 2010). Secondly, inverse modelling algorithms assume that values of v and m are more or less constant and that optimal fits between suites of observed and calculated river profiles are obtainable for $n = 1$ (Rudge et al., 2015; Roberts et al., 2019). In the case of West Africa, which has remained tectonically stable for a significant amount of geological time and where continental drainage has remained relatively stable for the last 30 Ma (see earlier discussion), it is reasonable to make such assumptions. However, this may not be the case in other regions of the world and at length and time scales where variations in factors such as climate and relative sea level become significant in determining the nature of 'source' to 'sink' sedimentary routing systems.

In the case of the Ganges delta, where $\sim 80\%$ of the Ganges system discharges and 95% of its annual sediment load is delivered during a period of only 4 months, seasonal forcing exerts a dominant control on the sedimentary budget to the continental margin (e.g. Goodbred, 2003). Results from Goodbred (2003) show that overall, discharge and sediment supply are roughly in balance during the Holocene and support general stability or slight aggradation along the Ganges dispersal system. The main conclusions emerging from these responses are that sedimentary signals in the Ganges are transferred rapidly from source to sink with little apparent attenuation and that this very large dispersal system responds to climate change at millennial timescales of 10^3 a, in a system-wide and contemporaneous manner. It is suggested that these responses are a function of the summer monsoon and its overarching control of the systems hydrology and, hence, sediment production and transport (Goodbred, 2003).

Armitage et al. (2011) assess the evolution of a tectonically active landscape undergoing erosional and depositional processes, using a numerical model that incorporates variations in grain size and the volumetric sediment budget. They parametrise the erosional system using a non linear diffusional model that de-

scribes the gross characteristics of topographic evolution and sediment release and include a grain size fining down-system using a field-verified, similarity-based approach (Smith and Bretherton, 1972; Simpson and Schlunegger, 2003; Densmore et al., 2007; Fedele and Paola, 2007; Duller et al., 2010). Their simulations of changes in precipitation or fault slip rate within a catchment–fan system indicate that catchment precipitation directly affects the grain size of exported sediments at timescales of < 1 Ma, before returning to steady-state. Abrupt increases in catchment precipitation result in increases in sedimentary flux that return to steady state with response times of 0.5 Ma. Abrupt decreases catchment precipitation result in a marked decrease sedimentary flux that return to steady-state with longer response times of 1 Ma. Armitage et al. (2011)'s results indicate that changes in precipitation and tectonic uplift both generate characteristic patterns of grain size and stratigraphic geometry, and exert an important control on the short-term sedimentary flux of fluvial systems to depositional basins.

The effects of relative sea level change and its fluvial responses are matter of significant scientific interest and play an important role in controlling sedimentary 'source' to 'sink' systems on timescales of $10^3 - 10^4$ a. Lowstand shorelines below the shelf edge trigger headward erosion and the development of cross-shelf valleys that provide a direct connection between the hinterland and the deep marine realm. However, lowstand shorelines that remain on the shelf limit fluvial incision and valley formation to the highstand coastal prism and traps the majority of terrigenous sediment updip of the shelf edge (Posamentier and Allen, 1999; Törnqvist et al., 2006). Törnqvist et al. (2006) use a geophysical model corrected for isostatic crustal movements to compute shoreline positions and quantify the position of the continental shelf edge by means of curvature for the Gulf of Mexico and Bay of Biscay since the Last Glacial Maximum (LGM, 21 ka). Their results show that whilst LGM sea level dropped ~ 40 m below the shelf edge at the Gulf of Mexico, LGM sea level remained landward off of the shelf edge by hundreds of kilometres in the Bay of Biscay. Their results show that the position of the lowstand shoreline at the Bay of Biscay caused the continental and deep marine segments to remain physically disconnected even during the last lowstand. This finding is particularly significant when it

is considered that conditions with sea level close to lowstand values lasted no more than some 10 ka, i.e., $< 10\%$ of the last glacial-interglacial cycle (Lambeck et al., 2002). Their findings at odds with conventional sequence stratigraphic models and challenges conventional ideas about the timing of sedimentation on continental margins and the ocean floor.

It is clear that different processes affect the timing and nature of sediment deposition in 'source' to 'sink' sedimentary routing systems. Changes in climate, lithology and sea level will undoubtedly have an effect on the evolution of drainage, surface topography and resultant sedimentary flux to offshore basins over the timescales relative to the changes that occur. However, long wavelength surface process that occur on timescales of > 10 Ma will be responsible for forcing the long term evolution of landscapes and their sedimentary budgets. Results from this study and others show that in the case of Africa, mantle-driven surface uplift since 30 Ma provides the dominant control drainage evolution and the long-term sedimentary flux to West Africa's passive continental margin and possibly others around the continent. The success of inverse modelling of longitudinal river profiles by obtaining best-fitting smooth spatio temporal uplift rate histories across continental scales also implies that on appropriately chosen time and length scales, a relatively small number of constant erosional parameters can describe this system

Roberts et al. (2019) spectrally analyse a subset of African longitudinal river profiles from this study that traverse different climatic zones, lithologic boundaries and biotic distributions by using a wavelet transform approach to investigate their scaling relationship with different types of noise. They find that $> 90\%$ of spectral power resides at long wavelengths of > 100 km, where spectra exhibit self-similar behavior consistent with red noise. A crossover transition from red to pink noise appears at wavelengths of ~ 100 km. This observation suggests that at shorter wavelengths, the effects of different noise (such as climate and lithology) become evident. These scaling observations are consistent with physically based landscape models in which the channelisation process is driven by white, or conceivably blue, noise but externally forced by large-scale regional uplift (Roberts et al., 2019).

The short-term sedimentary budget of fluvial landscapes to depositional basins is undoubtedly complex and sensitive to localised variations in factors such as climate, lithology and changes relative sea level on timescales of $10^3 - 10^4$ a. However, results from this study indicate that long term sedimentary budgets to offshore depositional basins at timescales of > 10 Ma are determined by the large-scale and long term regional forcing of fluvial landscapes.

4.6 Conclusion

I examine how stratigraphy offshore can be correlated with uplift rate histories onshore by inverting drainage networks, which are an important conduit for clastic efflux at continental margins, to predict patterns of offshore sedimentary flux in the Mauritanian basin, West Africa. A correlation between carbonate deposition offshore northwest Africa and periods of topographic quiescence onshore (i.e. low uplift rates) is observed (e.g. Sahagian, 1988). Significant increases in clastic solid sedimentary flux to the centre of the Mauritanian basin appear to be a response to post-Miocene uplift of the Mauritinides and Fouta-Djallon topographic swell. The deposition of post-Miocene clastic sedimentary rock in the Mauritanian basin has led to the formation of important Neogene clastic hydrocarbon reservoirs (e.g. Tiof, Pelican and Chinguetti fields). Periods of low continental uplift correspond with carbonate deposition at most deltas on Africa's passive margins and reduced clastic solid sedimentary flux to the continent's passive margin basins. Widespread uplift of the African continent is concomitant with increased clastic sedimentary flux to most of it's passive margins from Miocene-Recent times. Gravity anomalies, ocean age-depth residuals, tomography and the history of magamtism indicate that uplift was driven by sub-plate support. These observations indicate that mantle convection plays an important role in determining stratigraphy and the distribution of clastic hyrdocarbon reservoirs around passive continental margins.

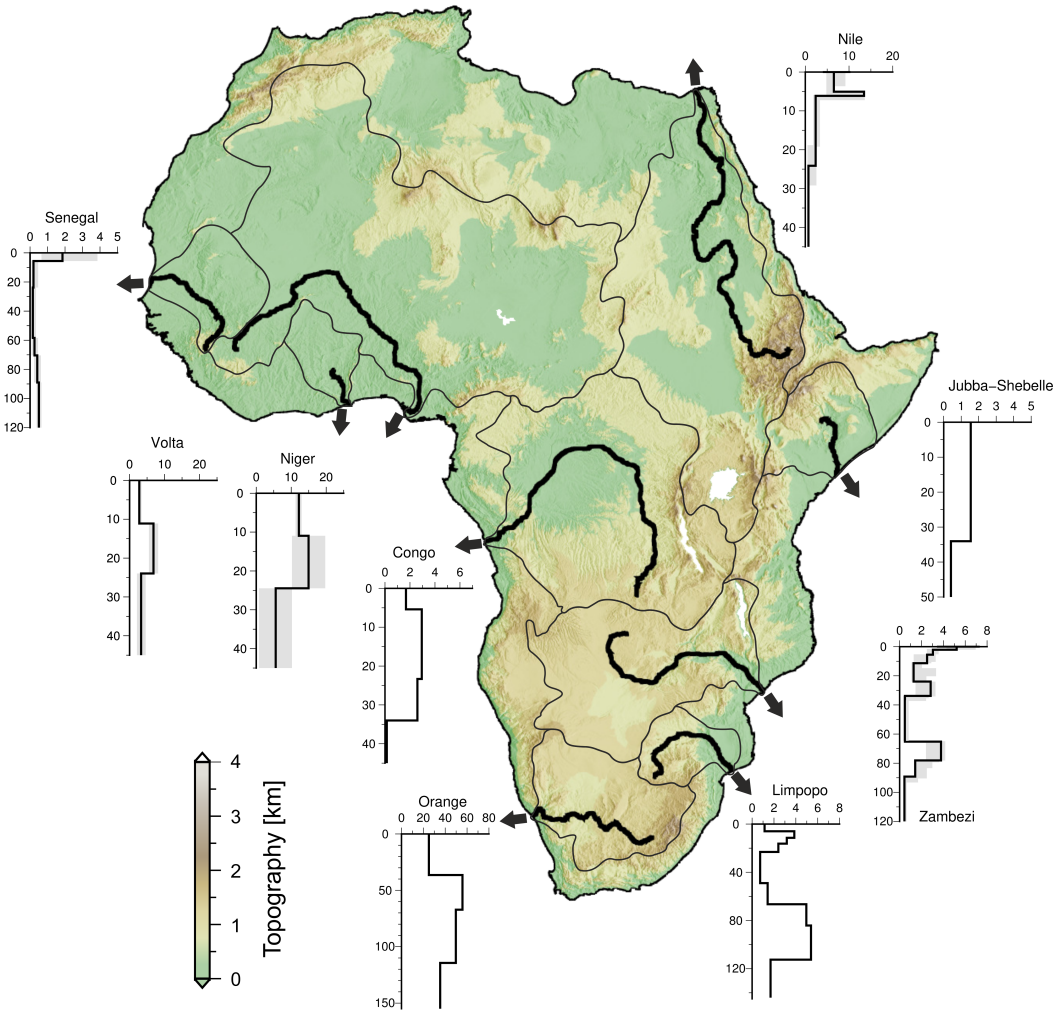


Figure 34: **Sedimentary flux to Africa's passive continental margins**. Map = present-day topography, major drainage divides and observed sedimentary flux of major African catchments. Sedimentary flux for Senegal is from this study; Volta: Paul et al. (2014); Niger: Grimaud et al. (2018); Congo: Paul et al. (2014); Nile: Aal et al. (2000); Hall et al. (2005); Jubba-Shebelle: DuToit et al. (1997); Zambezi: Walford et al. (2005); Limpopo: Dingle (1983); Orange: Rust and Summerfield (1990); Rouby et al. (2009). Age on y-axis has units of Ma; sedimentary flux on x-axis has units of $\times 10^3$ km^3 Ma^{-1}. Please note the colour scale used in this figure is for topography and not cumulative uplift.

Chapter 5

Future work & conclusions

5.1 Summary

The motivation of this study was to determine whether sediment 'sources' and 'sinks' can be linked by synthesising dynamic subsidence, continental uplift and sedimentary deposition to West Africa's passive margin. The following sections summarise the results of Chapters 2, 3 and 4.

Stratigraphy and sedimentary flux history of the Mauritanian basin

The sedimentary flux history of the Mauritanian basin is calculated by mapping seven stratigraphic horizons that are constrained using an inventory of 38 two-dimensional seismic reflection lines, eight commercial exploration wells and biostratigraphy. Check-shot data from wells are used to determine the best-fitting numerical parameters (initial porosity, ϕ_0 and compaction wavelength, λ) in order to convert stratigraphic horizons mapped in two-way time into depth. The effects of sediment loading and compaction are removed and volumes of sedimentary rock present between dated stratigraphic horizons are calculated. Up to 8 km of sedimentary rock is present between the acoustic basement (~ 225 Ma) and the oldest dated stratigraphic horizon, 89 Ma. Cretaceous solid sedimentary flux in the Mauritanian basin decreases steadily from

$0.41^{+0.21}_{-0.18}$ to $0.25^{+0.21}_{-0.17}$ during the Paleocene and to $0.16^{+0.18}_{-0.11}$ $\times 10^3$ km^3 Ma^{-1} during the Oligocene. Periods of low offshore sedimentary flux correspond with the deposition of carbonate and carbonate/clastic facies across the Mauritanian basin. In the centre of the basin, salt movement occurs from Cretaceous to Oligocene times. A significant change in the nature and magnitude of sedimentation to the Mauritanian basin occurs at ~ 23 Ma, whereby salt movement in the centre of the basin ceases and < 1.5 km of clastic sedimentary rock is deposited within a 500×500 km region in the centre of the basin at a rate of $0.20^{+0.20}_{-0.10} \times 10^3$ km^3 Ma^{-1}. A second major increase in clastic sedimentation is recorded at ~ 5.6 Ma, whereby < 2 km of sedimentary rock is deposited across the Mauritanian basin at a rate of $1.9^{+2.00}_{-1.40} \times 10^3$ km^3 Ma^{-1}. This period of increased clastic sedimentation to the Mauritanian basin and West African continental margin continues to the present day.

Shallow mantle convection beneath the Mauritanian basin

The tectonic subsidence history of the Mauritanian basin is calculated by back-stripping the eight wells presented in this study, corrected for water-loading and palaeo-water depths. During the period of salt movement, wide-spread Cenomanian–Campanian subsidence is recorded across the basin. This is followed by a period of tectonic quiescence and post-rift thermal sag. During Campanian–Oligocene times, observed subsidence profiles of all wells match theoretical thermal relaxation curves indicating that no anomalous subsidence occurred during this period. A significant phase of subsidence is recorded from Neogene–Recent times at wells in the centre of the basin, whereby 0.4–0.8 km of tectonic subsidence is observed. Modest subsidence in the centre of the basin begins at ~ 23 Ma, and accelerates at ~ 5.6 Ma to the present day. Flexural calculations show that the emplacement of the Cape Verde volcanic load cannot be responsible for the magnitudes of Neogene–Recent subsidence observed in the centre of the Mauritanian basin. The amplitude of subsidence indicates that glacio-eustasy is not responsible for generating the regional increase in accommodation observed. Stratal geometries in seismic data intersecting wells contain little/no evidence of growth in the shallow section, which indicate that Neogene salt withdrawal or thin-skinned tectonics did not generate the

observed subsidence patterns. Measured ocean-age depth residuals, calculated subsidence histories, magmatic histories, shear wave tomography and asthenospheric temperature calculations suggest that upper mantle convection has generated an east-west bathymetric gradient of $\sim 1/300$ during the last ~ 23 Ma. These observations are consistent with mantle downwelling below the Mauritanian part of the West African margin that formed in response to the flow of hot asthenosphere away from the upwelling mantle beneath Cape Verde.

African uplift and sedimentary flux from continental drainage inversion

African drainage is inverted to calculate a history of continental uplift and to predict the pattern of sedimentary flux to the West African passive margin from 30 Ma–Recent. The Fouta-Djallon swell, East African Rift system, domal swells (e.g. Hoggar, Angola, Tibesti, Bié) and southern Africa are uplifted by 1–3 km during the last 30 Ma. Continental uplift rates across Africa accelerate during the last $\sim$ 10–5 Ma. The residual misfit between observed and theoretical African longitudinal river profiles produced from calculated uplift histories is very low, such that rms misfit = 0.81. Predicted and observed uplift rates calculated from independent geologic constraints match within error. Model coverage is greatest for the largest river systems and decreases with age. The pattern of sedimentary flux to the Mauritanian basin from 30 Ma–Recent is consistent with predictions calculated from onshore drainage inversion. A stepped increase in sedimentary flux occurred at ~ 24 Ma and ~ 8 Ma onshore and this is followed by an increase of the same order of magnitude in offshore sedimentation at ~ 23 Ma and ~ 5.6 Ma in the Mauritanian basin following the onset of dynamic subsidence. The offshore study area is only a fraction of the total area to which sediment draining from West African rivers is delivered to along the continental margin. Sediment deposited elsewhere along the margin, dissolved into solution, transported elsewhere by coast parallel currents (i.e. contourites) and that which is deposited onshore is not received by the Mauritanian basin. For this reason, it is not possible to balance the mass of sediment

produced due to erosion onshore with measurements of sedimentary thickness offshore in the study area. However, the timing of increased sedimentary flux produced from onshore erosion and offshore deposition in the Mauritanian basin closely match. Increases in clastic sedimentary flux to most of Africa's offshore passive margin basins following continental uplift are observed by many authors at ~ 30 Ma and ~ 10–5 Ma, and are probably a result of changes in mantle convection beneath the African continent during these times.

5.2 Implications of results & future work

5.2.1 How far back can we go?

Palaeogeographic reconstructions made by mapping widely and densely distributed dated and regionally correlated lateritic paleolandscape remnants across West Africa indicate that the main river courses of the subregion stabilised around $\sim$ 29–34 Ma. Offshore sedimentation since this time is linked to the inland morphoclimatic record, particularly in the case of the Niger catchment–delta system (Chardon et al., 2016; Grimaud et al., 2018). In the Niger Delta, comparisons of denuded and clastic sediment volumes accumulated offshore show a fairly balanced sediment budget between the Niger catchment and its delta since 45 Ma. It is reasonable to assume that the modern Niger catchment was established prior to 29 Ma, which provided clastic material to the Niger delta from the erosion products of the dynamically-supported Hoggar hotspot swell (Grimaud et al., 2018). In the Senegambia catchment, south of the Senegal River, Mid-Eocene paleogeography reveals the antiquity back to at least 45 Ma (Chardon et al., 2016). Hence for the purposes of this study, it was reasonable to choose a timescale of 30–0 Ma to conduct a 'source to sink' study for the West African passive margin on the basis of drainage inversion. However, it is clear that the main limitation with the method of inverting rivers for spatio-temporal histories of uplift is the evolution and changing pattern of drainage itself. For example, the establishment the Orange river network during the Early Cenozoic was a result of the capture of the upper part of the Karoo River by the the lower Kalahari River (De Wit, 1999). In many parts of the

world, it cannot be assumed that present-day drainage patterns have remained stable for the time timescales used in this study. This raises another interesting question: can inverting rivers for uplift rate histories be taken further back in time than present-day drainage profiles allow, by using reconstructions of palaeo-drainage and palaeo-river profiles?

Reconstructions of palaeo-drainage networks have been a subject of interest to the geomorphological community for a substantially long time. However, studies which focus on reconstructing longitudinal profiles of palaeo-rivers buried deep in the geological record are scarce. Longitudinal profiles of palaeo-rivers extracted from landscapes reconstructed using seismic and well data from the North Sea show that a terrestrial landscape formed at 58–55 Ma buried ~ 1.5 km beneath the seabed, formed in a < 3 Ma period and was rapidly drowned. The uplift history calculated by palaeo-river inversion is similar to that of a slightly older buried landscape in the Faeroe-Shetland basin ~ 400 km to the west, and the record of vertical motions are consistent with pulses of anomalously hot asthenosphere spreading out from the incipient Icelandic plume (Stucky de Quay et al., 2017). Stucky de Quay et al. (2017)'s observations suggest that a thermal anomaly departed the Icelandic plume around 57.4 ± 2.2 Ma at the latest and travelled with a velocity $>\sim 150$ km Ma^{-1}. This is an important example into how (on a basin-scale) the information held by palaeo-river profiles can be used to constrain geological and geophysical processes which are no longer visible using present-day drainage patterns or surface observations.

The implications of being able to constrain thermal processes in the upper mantle are important for assessing the thermal history of many of the world's sedimentary basins and would form a useful tool in a geochemist's appraisal toolbox when prospecting for petroleum systems. This raises another interesting question: can predictions of sedimentary flux from drainage inversion be used as an appraisal tool by industry?

5.2.2 Implications for industry

A method to identify possible hydrocarbon reservoirs that relies solely on freely available (or relatively cheap) DEM data and independent geologic constraints

of uplift published in literature would be of immense value to industry. Recent advancements in literature search software (such as Elsevier's new Geofacets search tool) allow comprehensive searches for geological data to be conducted for customised regions of the Earth. The results from this study have far-reaching implications as I show that the pattern of clastic input from regions of high dynamic topography overlain by radial drainage networks (i.e. 'source' regions) adjacent to regions of low free air gravity anomalies (i.e. 'sink' regions) can be tested relatively easily. Predictions of sedimentary flux calculated from drainage inversion calibrated using published independent geological constraints in this study are consistent with the pattern of sedimentary flux observed offshore in the Mauritanian basin. The results of this study show that in the absence of offshore data, it would have been possible to deduce the pattern of sedimentary flux to the Mauritanian basin from Neogene–Recent times from drainage inversion alone and thus predict reservoir deposition, burial/uplift history and regional seal development. The development of software which automates the drainage extraction process and sedimentary flux calculation for regions defined by the consumer, using either publicly available DEM data (e.g. SRTM DEM data as used in this study) or that which is input manually would provide industry with a tool to make quick first-order estimates of sedimentary input to regions of potential exploration interest.

5.2.3 Localised studies & environmental applications

For the purposes of this study, the choice of a DEM of the African continent generated using the 3-arc second SRTM dataset, which has a resolution of $\sim 90 \times 90$ m, was appropriate for evaluating continental-scale histories of uplift. However, localised studies using the inverse method will be dependent on the resolution of the DEM data used and availability of independent geologic constraints used to calibrate the erosional model. Stucky de Quay et al. (2019) combine high-resolution drone photogrammetry and cosmogenic ^{3}He dating of fluvial terraces to measure the erosional history of one of Icelands largest knickzones, Jökulsárglúfur, in the northeast part of the island. Their results suggest that regional uplift and fluvial erosion can rapidly generate hundreds of metres of relief in post-glacial landscapes over much shorter time and length-

scales than that considered in this study. Since the commencement of this study in 2014, a new freely available database of SRTM global elevation data offers worldwide coverage of void filled data at a resolution of 1 arc-second (i.e. 30×30 metres, USGS, 2016). Such resources can be utilised for regional studies or when conducting preliminary investigations prior to obtaining drone photogrammetry from field studies to obtain higher-resolution DEM's.

Pechlivanidou et al. (2018) show that for very recent geological history (< 10 ka), it is possible use the stream-power model to balance the mass of sedimentary rock calculated from onshore denudation with that deposited offshore. This raises another interesting question: can drainage inversion be used to constrain the mass and distribution of sediment transported to basins within recent geological history? Given the success of matching patterns of sedimentary flux to open systems using drainage inversion to the West African passive margin in this study, it is highly possible that for small regions this method may be taken much further.

There is a growing interest in using near-surface geophysical methods as a tool for mapping the distribution of marine benthic habitats in the environmental protection community. Currently, studies focus on using high resolution multi-beam bathymetry, seismic backscatter and seismic waveform-inversion to calculate a suite of geophysical derivatives that can be used to constrain sediment bottom type and characterise marine benthic habitats (e.g. Stevenson et al., 2002; Schock, 2004; Rattray et al., 2009; Wang and Stewart, 2015; Ierodiaconou et al., 2018). However, such methods are of limited scope as geophysical data must be physically acquired thus restricting benthic habitat analysis to the survey area. If the provenance and sedimentary flux of rivers which drain sediments into shallow coastal environments can be quantified, it may be possible to make predictions of bottom type and benthic environments. One possible region of dynamically-uplifting topography where this could be explored is along the southern coastline of Australia's Victoria state. In this region, bedrock of the Murray river is predominantly Neogene–Recent in age and youngs towards to coast (Langford et al., 1995). Results from Rudge et al. (2015) show that this region has been uplifted by ~ 1 km during the last 40 Ma. Post-glacial uplift of Iceland during the last 9 ka has had important

consequences to the island's drainage evolution within a relatively short time period (Stucky de Quay et al., 2019). Hence, small changes in uplift along the Murray River and surrounding region within time-scales of < 10 ka may have important repercussions for the sediment flux delivered to the coast by rivers in this region. On the scale of interest to the marine benthic community, combining the inverse method used in this study to constrain sediment mass fluxes with analyses of the provenance of sediments delivered to regions within several kilometres of the coastline would be of significant value. Success could drastically improve the spatial coverage of marine benthic habitat mapping efforts currently restricted to survey areas of only a few square kilometres (e.g. Rattray et al., 2009; Ierodiaconou et al., 2018).

5.3 Conclusions

The results of this study show that combining geological and geophysical observations of dynamic subsidence, continental uplift and sedimentary deposition to West Africas passive margin provides a methodology to quantitatively link the 'sources' and 'sinks' of sedimentary flux to the Mauritanian basin with uplift of the continental hinterland.

In the case of the Mauritanian basin, the initiation and acceleration of shallow mantle convection from Neogene–Recent times is the most likely cause of basin subsidence. Basin subsidence was accompanied by a concomitant increase in dynamic support beneath West Africa's passive continental margin which caused uplift of the Fouta-Djallon topographic swell and Mauritanide fold belt. The results from this study suggest that the Neogene clastic flux to the Mauritanian margin was generated by erosion of the uplifting Mauritinides and Fouta-Djallon topographic swell from ~ 22 Ma, which appears to have accelerated during the last ~ 8 Ma. Calculated uplift rates for the African continent are corroborated by an independent inventory of uplift constraints from around Africa's coastline. The pattern and timings of increases in sedimentary flux to West Africa's passive margin predicted from drainage inversion match those made using offshore data from the Mauritanian basin from 30 Ma to Recent times. An increase in clastic sedimentary flux and change from carbonate

to clastic offshore sedimentation at ~ 30 Ma is recorded at nearly every major African river delta, which I suggest was generated by increased Neogene uplift rates at many of Africa's domal swells. The Uplift rate history for the African continent calculated by drainage inversion supports the notion that African topography has grown considerably during the last ~ 30 Ma and is most likely a result of changing patterns of mantle convection beneath the continent.

Finally, the results of this study suggest that inverse modelling of drainage patterns for uplift rate histories provides a methodology to quantitatively link 'sources' and 'sinks' of sedimentary rock deposited to passive continental margins, which may help to predict the presence of offshore clastic reservoirs and regional seals generated as a response to variations in hinterland uplift and erosion.

Chapter 6

Appendices

6.1 Appendix 1

This section describes the intermediary steps in calculating the solid sedimentary flux and distribution of sedimentary rock in the Mauritanian basin. Depths to seismic marker horizons were picked along seismic lines and mapped in two-way time. Raw picks of seismic data were interpolated across the study area by using an adapted version of the minimum-curvature method from Smith and Wessel (1990).

6.1.1 Generating continuous surfaces

The minimum-curvature method interpolates randomly spaced input data to be gridded with a surface having continuous second derivatives and minimal total squared curvature. The minimum-curvature surface has an analogy in elastic plate flexure and approximates the shape adopted by a thin plate flexed to pass through the data points (Smith and Wessel, 1990). However, minimum-curvature surfaces may have large oscillations and extraneous inflection points which make them unsuitable for gridding in many applications. Smith and Wessel (1990) modify the minimum-curvature method by adding a tension factor to the elastic-plate flexure equation, such that randomly spaced (x, y, z) triples from a standard input file or table are read and used to produce a binary grid file of gridded values, $z(x, y)$, by solving:

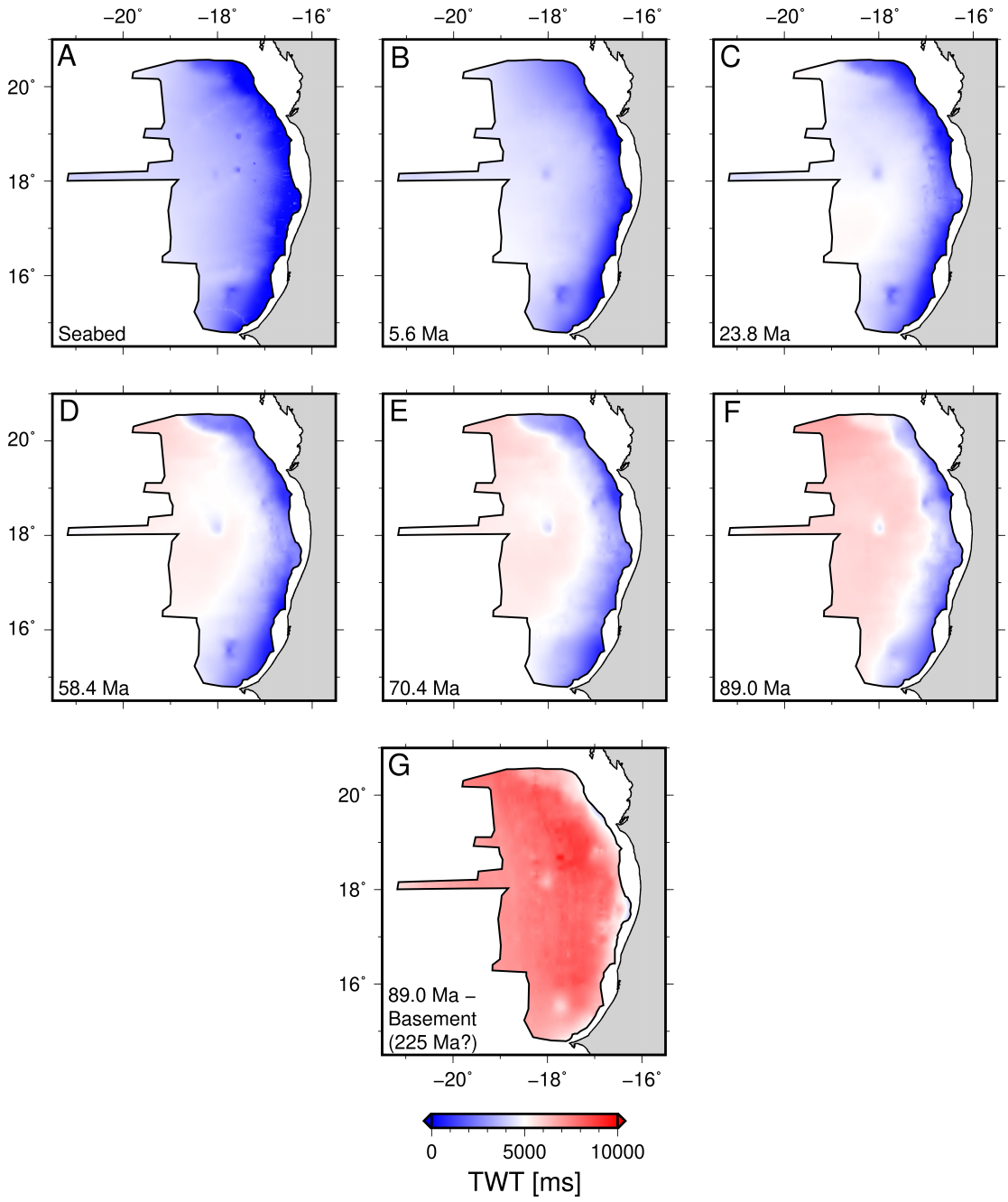


Figure 35: **Seismic horizons mapped in two-way time**. (A–G) Seismic horizons mapped and extrapolated across the study area as surfaces. Coordinates and locations of seismic data is not shown due to data confidentiality.

6.1.2 Depth conversion and sediment thickness calculation

Extrapolated seismic marker surfaces mapped in two-way time were converted to depth using the mean time-depth relationship calculated from check-shot and well data (Chapter 2). This relationship is $z(t) = 0.0017t^2 + 0.9t - 34$, where t = two-way travel time in ms. Depth converted seismic marker horizons are shown on Figure 36. The thickness of sedimentary rock in the Mauritanian basin was determined by calculating the volume between depth converted seismic marker horizons. The distribution and thickness of sedimentary rock (not corrected for the effects of porosity and compaction) is shown on Figure 37.

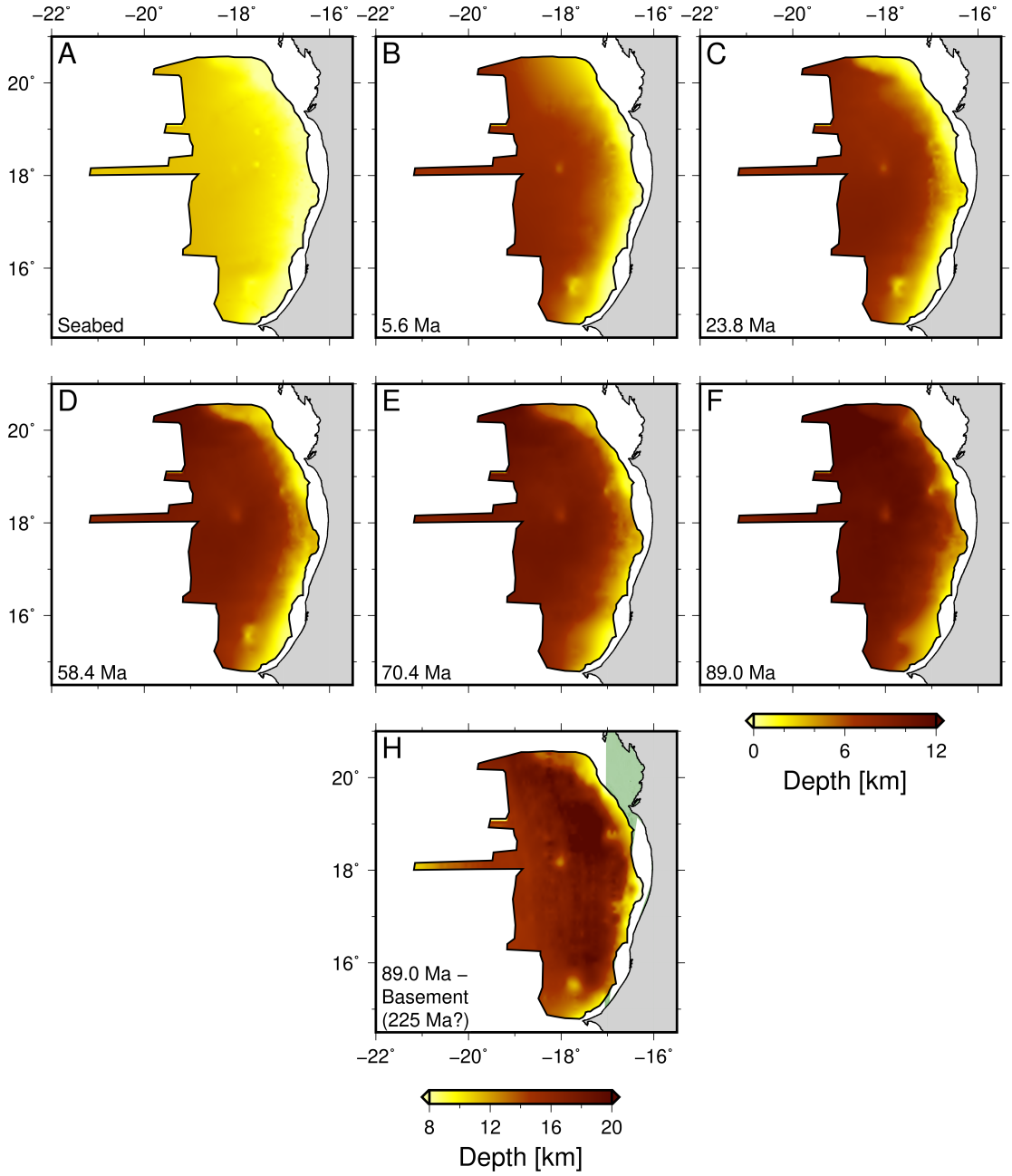


Figure 36: **Depth converted seismic horizons**. (A–H) Seismic horizons converted from two-way time (Figure 35) to depth using the mean time-depth relationship, $z(t) = 0.0017t^2 + 0.9t - 34$ (Chapter 2). Note the difference in scale of panels (A–F) and (H).

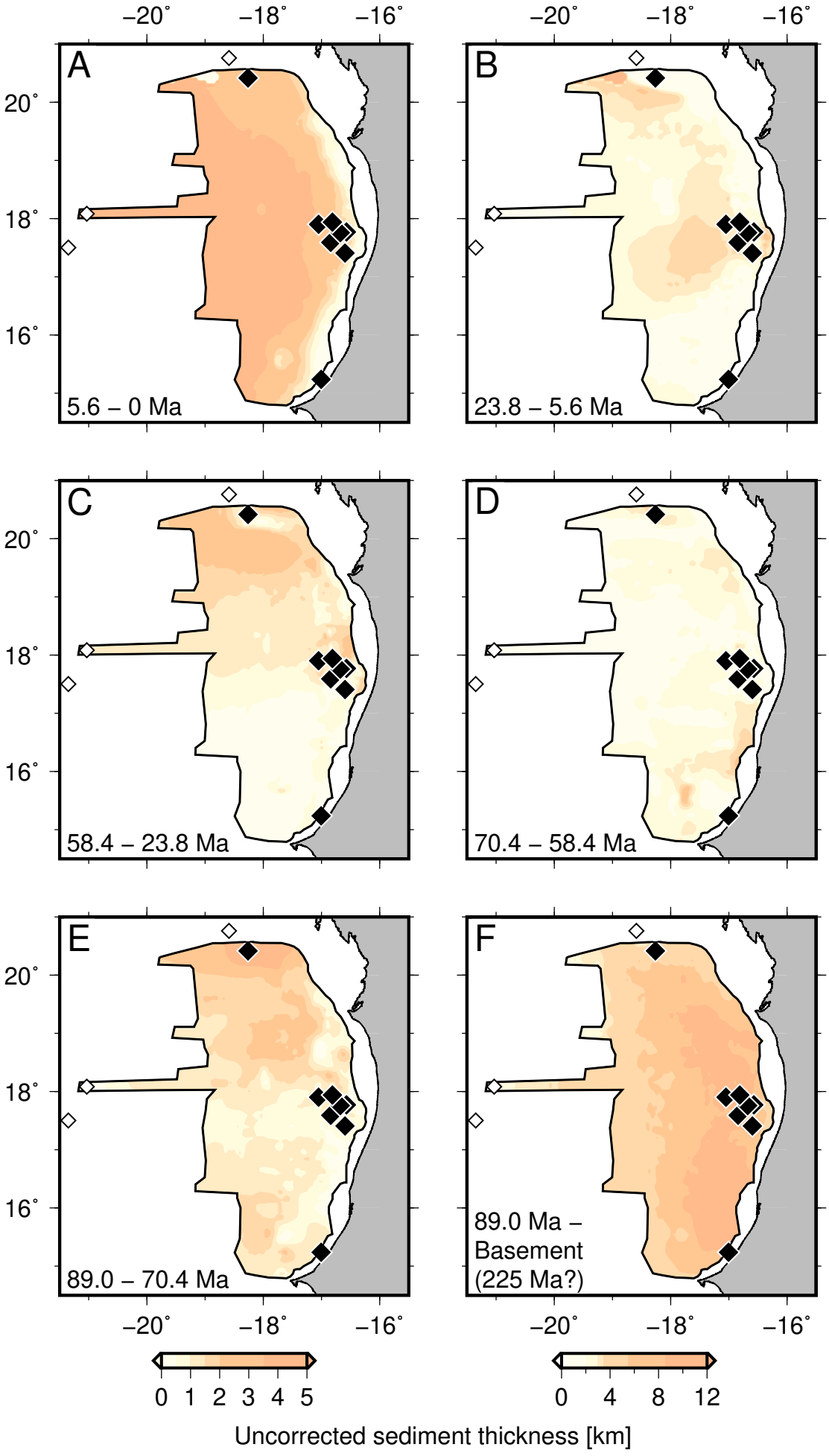

A
5.6 – 0 Ma
B
23.8 – 5.6 Ma
C
58.4 – 23.8 Ma
D
70.4 – 58.4 Ma
E
89.0 – 70.4 Ma
F
89.0 Ma –
Basement
(225 Ma?)
−20˚
−18˚
−16˚
20˚
18˚
16˚
0 1 2 3 4 5
0 4 8 12
Uncorrected sediment thickness [km]

Figure 37: **Uncorrected sediment thickness**. (A–F) Thickness of sedimentary rock present between stratigraphic horizons (Figure 36). Solid sedimentary fluxes were calculated by correcting these values for the effects of porosity and compaction using the mean values of parameters that best-fit the mean time-depth pairs of all check-shot data for the wells in my database ($\phi_\circ = 0.75 \pm 0.1$, $\lambda = 2.66 \pm 1.2$ km, Chapter 2).

References

Aal, A. A., El Barkooky, A., Gerrits, M., Meyer, H., Schwander, M., Zaki, H., 2000. Tectonic evolution of the Eastern Mediterranean Basin and its significance for hydrocarbon prospectivity in the ultradeepwater of the Nile Delta. The Leading Edge 19 (10), 1086–1102.

Al-Hajri, Y., White, N., Fishwick, S., 2009. Scales of transient convective support beneath Africa. Geology 37 (10), 883–886.

Allen, A., 1997. Earth Surface Processes.

Allen, P. A., 2008. Time scales of tectonic landscapes and their sediment routing systems. Geological Society, London, Special Publications 296 (1), 7–28.

Amante, C., B.W., E., 2009. ETOPO1 1 Arc-Minute Global Relief Model: Procedures, Data Sources and Analysis. NOAA Technical Memorandum NESDIS NGDC-24 National G.

Anka, Z., Séranne, M., 2004. Reconnaissance study of the ancient Zaire (Congo) deep-sea fan (ZaiAngo Project). Marine Geology 209 (1-4), 223–244.

Armitage, J. J., Duller, R. A., Whittaker, A. C., Allen, P. A., 2011. Transformation of tectonic and climatic signals from source to sedimentary archive. Nature Geoscience 4 (4), 231–235.

Athy, L. F., 1930. Density, Porosity, and Compaction of Sedimentary Rocks. AAPG Bulletin 14 (1), 194–200.

Barnett-Moore, N., Hassan, R., Müller, R. D., Williams, S. E., Flament, N., 2017. Dynamic topography and eustasy controlled the paleogeographic evolution of northern Africa since the mid-Cretaceous. Tectonics 36 (5), 929–944.

Benkhelil, J., 1989. The origin and evolution of the Cretaceous Benue Trough (Nigeria). Journal of African Earth Sciences 8, 251–282.

Berggren, W. A., Kent, D. V., Swisher, C. C., Aubry, M.-P., 1995. A Revised Cenozoic Geochronology and Chronostratigraphy. Geochronology, Time Scales, and Global Stratigraphic Correlation (54).

Bishop, P., 2007. Longterm landscape evolution: linking tectonics and surface processes. Earth Surface Processes and Landforms: The Journal of the British Geomorphological Research Group 32 (3), 329–365.

Black, R., Latouche, L., Liegeois, J. P., Caby, R., Bertrand, J. M., 1994. Pan-African displaced terranes in the Tuareg Shield (central Sahara). Geology 22 (7), 641–644.

Bloom, A., Broecker, W., Chappell, J., Matthews, R., Mesolella, K., 1974. Quaternary sea level fluctuations on a tectonic coast: New 230 Th/234 U dates from the Huon Peninsula, New Guinea. Quaternary research 4 (2), 185–205.

Blow, W., 1969. Late middle Eocene to Recent planktonic foraminiferal biostratigraphy. In: Proceedings of the First International Conference on Planktonic Microfossils. In: Proceedings of the First International Conference on Planktonic Microfossils, Geneva 1967. pp. 199–422.

Bolli, H., 1957a. Planktonic foraminifera from the Oligocene-Miocene Cipero and Lengua formation, Trinidad. Bull. US Nat. Mus. 215, 97–124.

Bolli, H., 1957b. The genera Globigerina and Globorotaria in Paleocene-Lower Eocene Lizard Spring Formation of Trinidad, BWI. Bulletin of the United States National Museum 215, 61–81.

Bolli, H. M., Saunders, J. B., Perch-Nielsen, K., 1989. Plankton stratigraphy. Volume 1, Planktic foraminifera, calcareous nannofossils and calpionellids. Cambridge earth science series.

Bralower, T. J., Monechi, S., Thierstein, H. R., 1989. Calcareous nannofossil zonation of the Jurassic-Cretaceous boundary interval and correlation with the geomagnetic polarity timescale. Marine Micropaleontology 14 (1-3), 153–235.

Brown, P., Rutledge, D., Crux, J., Gallagher, L., 1998. Early Cretaceous. In: Brown, P. (Ed.), Calcareous nannofossil biostratigraphy, british mi Edition. Chapman & Hall, London, pp. 86–131.

Brownfield, M. E., Charpentier, R. R., 2003. Assessment of the Undiscovered Oil and Gas of the Senegal Province, Mauritania, Senegal, The Gambia, and Guinea-Bissau, Northwest Africa. U.S. Geological Survey Bulletin 2207-A, 1–29.

Bumby, A. J., Guiraud, R., 2005. The geodynamic setting of the Phanerozoic basins of Africa. Journal of African Earth Sciences 43 (1-3), 1–12.

Burke, K., 1996. The African Plate. South African Journal of Geology.

Burke, K., Gunnell, Y., 2008. The African Erosion Surface: A Continental-Scale Synthesis of Geomorphology, Tectonics, and Environmental Change over the Past 180 Million Years. In: Memoir 201: The African Erosion Surface: A Continental-Scale Synthesis of Geomorphology, Tectonics, and Environmental Change over the Past 180 Million Years.

Burke, K., MacGregor, D. S., Cameron, N. R., 2003. Africa's petroleum systems: four tectonic Aces' in the past 600 million years. Geological Society, London, Special Publications 207 (1), 21–60.

Burnett, J., 1998. Upper Cretaceous. In: Brown, P. (Ed.), Calcareous Nannofossil Biostratigraphy, british mi Edition. Chapman & Hall, London, pp. 132–199.

Cammarano, F., Goes, S., Vacher, P., Giardini, D., 2003. Inferring upper-mantle temperatures from seismic velocities. Physics of the Earth and Planetary Interiors 138 (3-4), 197–222.

Causse, C., Hillaire-Marcel, C., 1989. Th and U isotopes in Upper Pleistocene sediments of ODP Site 645 (Baffin Bay) and 646, 647 (Labrador Sea). Proc. ODP Sci. Res. 105, 551–560.

Chappell, J., Shackleton, N., 1986. Oxygen isotopes and sea level. Nature 324 (13), 137–140.

Chardon, D., Grimaud, J.-L., Rouby, D., Beauvais, A., Frederic, C., 2016. Stabilization of large drainage basins over geological time scales: Cenozoic West Africa, hot spot swell growth, and the Niger River. Geochemistry, Geophysics, Geosystems 17, 1164–1181.

Christensen, N., 1982. Seismic velocities. In: Carmichael, R.S. (Ed.), Handbook of physical properties of rocks. CRC Press, Boca Raton, Fla, pp. 57–74.

Clark, M. K., Royden, L. H., Whipple, K. X., Burchfiel, B. C., Zhang, X., Tang, W., 2006. Use of a regional, relict landscape to measure vertical deformation of the eastern Tibetan Plateau. Journal of Geophysical Research: Earth Surface 111 (3), 1–23.

Clift, P. D., Sun, Z., 2006. The sedimentary and tectonic evolution of the Yinggehai-Song Hong basin and the southern Hainan margin, South China Sea: Implications for Tibetan uplift and monsoon intensification. Journal of Geophysical Research: Solid Earth 111 (6), 1–28.

Connolly, J. A., 2005. Computation of phase equilibria by linear programming: A tool for geodynamic modeling and its application to subduction zone decarbonation. Earth and Planetary Science Letters 236 (1-2), 524–541.

Corvinus, G., Hendey, Q., 1978. A new Miocene vertebrate locality at Arrisdrif in South West Africa. Neues Jahrbuch für Geologie und Paläontologie, Monatsheft, 193–205.

Courtney, R. C., White, R. S., 1986. Anomalous heat flow and geoid across the Cape Verde Rise: evidence for dynamic support from a thermal plume in the mantle. Geophysical Journal of the Royal Astronomical Society 87 (3), 815–867.

Covault, J. A., Romans, B. W., Graham, S. A., Fildani, A., Hilley, G. E., 2011. Terrestrial source to deep-sea sink sediment budgets at high and low sea levels: Insights from tectonically active Southern California. Geology 39 (7), 619–622.

Cox, K., 1989. The role of mantle plumes in the development of continental drainage patterns. Nature 342, 873–876.

Croissant, T., Braun, J., 2014. Constraining the stream power law: A novel approach combining a landscape evolution model and an inversion method. Earth Surface Dynamics 2 (1), 155–166.

Crosby, A. G., Fishwick, S., White, N., 2010. Structure and evolution of the intracratonic Congo Basin. Geochemistry, Geophysics, Geosystems.

Crosby, B. T., Whipple, K. X., 2006. Knickpoint initiation and distribution within fluvial networks: 236 waterfalls in the Waipaoa River, North Island, New Zealand. Geomorphology.

Czarnota, K., Roberts, G. G., White, N. J., Fishwick, S., 2014. Spatial and temporal patterns of Australian dynamic topography from river profile modeling. Journal of Geophysical Research: Solid Earth 119 (2), 1384–1424.

Dalton, C., Langmuir, C., Gale, A., 2014. Geophysical and Geochemical Evidence for Deep Temperature Variations Beneath Mid-Ocean Ridges. Science 344 (April), 2–5.

Daly, M. C., Chorowicz, J., Fairhead, J. D., 1989. Rift basin evolution in Africa: the influence of reactivated steep basement shear zones. Geological Society, London, Special Publications.

Davies, D. R., Rawlinson, N., 2014. On the origin of recent intraplate volcanism in Australia. Geology 42 (12), 1031–1034.

Davies, O., 1970. Pleistocene beaches of Natal. Annals of the Natal Museum 20 (2), 403–442.

Davies, O., 1971. Pleistocene shorelines in the south- ern and south-eastern Cape Province (Part 1). Annals of the Natal Museum 21, 183–223.

Davison, I., 2005. Central Atlantic margin basins of North West Africa: Geology and hydrocarbon potential (Morocco to Guinea). Journal of African Earth Sciences.

De Klasz, I., 1978. The West African sedimentary basins. In: Moullade, A. M., and Nairn, A. E. M., eds., The Phanerozoic geology of the world: The Mesozoic. Elsevier, Amsterdam, Netherlands, pp. 371–399.

De Wit, M., 1993. Cainozoic evolution ofdrainage systems in the north- western Cape. Ph.D. thesis, Dept. Geo., Univ. Cape Town.

De Wit, M., 1999. Post-Gondwana Drainage and the Development of Diamond Placers in Western South Africa. Economic Geology 94 (5), 721–740.

Debayle, E., 1999. SV-wave azimuthal anisotropy in the Australian upper mantle: Preliminary results from automated Rayleigh waveform inversion. Geophysical Journal International 137 (3), 747–754.

Densmore, A. L., Allen, P. A., Simpson, G., 2007. Development and response of a coupled catchment fan system under changing tectonic and climatic forcing. Journal of Geophysical Research: Earth Surface 112 (1), 1–16.

Dercourt, J., Zonenshain, L. P., Ricou, L. E., Kazmin, V. G., Le Pichon, X., Knipper, A. L., Grandjacquet, C., Sbortshikov, I. M., Geyssant, J., Lepvrier, C., Pechersky, D. H., Boulin, J., Sibuet, J. C., Savostin, L. A., Sorokhtin, O., Westphal, M., Bazhenov, M. L., Lauer, J. P., Biju-Duval, B., 1986. Geological evolution of the tethys belt from the atlantic to the pamirs since the LIAS. Tectonophysics 123 (1-4), 241–315.

Dillon, W. P., Schlee, J. S., Klitgord, K. D., 1988. The development of the continental margin of eastern North America-conjugate continental margin to West Africa. Journal of African Earth Sciences 7 (2), 361–367.

Dingle, R. V., 1983. Continental Margin Subsidence: A Comparison Between East and West Coasts of Africa. Dynamics of passive margins 13.

Dingle, R. V., Hendry, Q. B., 1984. Late Mesozoic and Tertiary sediment supply to the eastern Cape Basin (SE Atlantic) and palaeo-drainage systems in Southwestern Africa. Marine Geology 56 (1-4), 13–26.

Divins, D., 2003. Total Sediment Thickness of the World's Oceans & Marginal Seas. NOAA National Geophysical Data Center, Boulder, CO.

Duller, R., Whittaker, A., Fedele, J., Whitchurch, A., Springett, J., Smithells, R., Fordyce, S., Allen, P., 2010. From grain size to tectonics. Journal of Geophysical Research, 115 115 (3).

DuToit, S., Kidston, A., Slind, O., 1997. The Hydrocarbon Potential of the East Africa Continental Margin. Alconsult International Ltd, Toronto, Canada.

Ebinger, C. J., Deino, A. L., Tesha, A. L., Becker, T., Ring, U., 1993. Tectonic controls on rift basin morphology: Evolution of the northern Malawi (Nyasa) Rift. Journal of Geophysical Research: Solid Earth 98 (B10), 17821–17836.

Ebinger, C. J., Sleep, N., 1998. Cenozoic magmatism throughout East Africa resulting from impact of a single plume. Nature 395, 788–791.

Elmejdoub, N., Jedoui, Y., 2009. Pleistocene raised marine deposits of the Cap Bon peninsula (N-E Tunisia): Records of sea-level highstands, climatic changes and coastal uplift. Geomorphology 112 (3-4), 179–189.

Emery, K., Uchupi, E., 1984. The Geology of the Atlantic Ocean.

Erlanger, E. D., Granger, D. E., Gibbon, R. J., 2012. Rock uplift rates in South Africa from isochron burial dating of fl uvial and marine terraces. Geology 40 (11), 1019–1022.

Fairhead, J. D., 1988a. Late Mesozoic rifting in Africa. Developments in Geotectonics.

Fairhead, J. D., 1988b. Mesozoic plate tectonic reconstructions of the central South Atlantic Ocean: The role of the West and Central African rift system. Eisevier Science Publishers B.V.. Amsterdam.

Farr, T., Rosen, P., Caro, E., Crippen, R., Duren, R., Hensley, S., Kobrick, M., Paller, M., Rodriguez, E., Roth, L., Seal, D., Shaffer, S., Shimada, J., Umland, J., Werner, M., Oskin, M., Burbank, D., Alsdorf, D., 2007. The shuttle radar topography mission. Reviews of Geophysics 45 (2005), 1–33.

Fedele, J. J., Paola, C., 2007. Similarity solutions for fluvial sediment fining by selective deposition. Journal of Geophysical Research: Earth Surface 112 (2), 1–13.

Fishwick, S., 2010. Surface wave tomography: Imaging of the lithosphere-asthenosphere boundary beneath central and southern Africa? Lithos 120 (1-2), 63–73.

Fishwick, S., Bastow, I. D., 2011. Towards a better understanding of African topography: a review of passive-source seismic studies of the African crust and upper mantle. Geological Society, London, Special Publications 357 (1), 343–371.

Fitton, J. G., James, D., Leeman, W. P., 1991. Basic magmatism associated with Late Cenozoic extension in the western United States: Compositional variations in space and time. Journal of Geophysical Research: Solid Earth 96 (B8), 13693–13711.

Flament, N., Gurnis, M., Muller, R. D., 2013. A review of observations and models of dynamic topography. Lithosphere 5 (2), 189–210.

Förste, C., Bruinsma, S., Abrikosov, O., Lemoine, J.-M., Marty, J. C., Flechtner, F., Balmino, G., Barthelmes, F., Biancale, R., 2014. EIGEN-6C4 The latest combined global gravity field model including GOCE data up to degree and order 2190 of GFZ Potsdam and GRGS Toulouse.

Fowler, C., 2006. The Solid Earth, 2nd Edition. Cambridge University Press.

Fox, M., Goren, L., May, D. A., Willett, S. D., 2014. Inversion of fluvial channels for paleorock uplift rates in Taiwan. Journal of Geophysical Research: Earth Surface 119 (9), 1853–1875.

French, S., Lekic, V., Romanowicz, B., 2013. Waveform Tomography Reveals Channeled Flow at the Base of the Oceanic Asthenosphere. Science 342 (2), 227–231.

Furman, T., Bryce, J., Rooney, T. O., Hanan, B., Yirgu, G., Ayalew, D., 2006. Heads and tails: 30 million years of the Afar plume. In: G. Yirgu, C.J. Ebinger, P. M. (Ed.), The Afar Volcanic Province Within the East African Rift System. Vol. 259. Geol. Soc. London Spec. Publ., pp. 95–119.

Gallagher, K., Brown, R., 1999. The Mesozoic denudation history of the Atlantic margins of southern Africa and southeast Brazil and the relationship to offshore sedimentation. Geological Society, London, Special Publications 153, 41–53.

Giresse, P., Barusseau, J. P., Causse, C., Diouf, B., 2000. Successions of sea-level changes during the Pleistocene in Mauritania and Senegal distinguished by sedimentary facies study and U/Th dating. Marine Geology 170 (1-2), 123–139.

Giresse, P., Hoang, C.-T., Kouyoumontzakis, G., 1984. Analysis of vertical movements deduced from a geochronological study of marine Pleistocene deposits, southern coast of Angola. Journal of African Earth Sciences (1983) 2 (2), 177–187.

Goes, S., 2002. Thermal structure of the North American uppermost mantle inferred from seismic tomography. Journal of Geophysical Research 107 (B3), 2050.

Goes, S., Armitage, J., Harmon, N., Smith, H., Huismans, R., 2012. Low seismic velocities below mid-ocean ridges: Attenuation versus melt retention. Journal of Geophysical Research B: Solid Earth 117 (12), 1–19.

Goes, S., Govers, R., Vacher, P., 2000. Shallow mantle temperatures under Europe from P and S wave tomography. Journal Of Geophysical Research-Solid Earth 105 (B5), 11153–11169.

Goodbred, S. L., 2003. Response of the Ganges dispersal system to climate change: A source-to-sink view since the last interstade. Sedimentary Geology 162 (1-2), 83–104.

Goren, L., Fox, M., Willett, S. D., 2014. Tectonics from fluvial topography using formal linear inversion: Theory and applications to the Inyo Mountains, California. Journal of Geophysical Research F: Earth Surface 119 (8), 1651–1681.

Grimaud, J. L., Rouby, D., Chardon, D., Beauvais, A., 2018. Cenozoic sediment budget of West Africa and the Niger delta. Basin Research 30 (2), 169–186.

Guiraud, M., 1993. Late Jurassic riftingEarly Cretaceous rifting and Late Cretaceous transpressional inversion in the Upper Benue Basin (NE Nigeria). Bulletin des Centres de Recherches Exploration-Production Elf-Aquitaine 17, 371–383.

Guiraud, M., Buta-Neto, A., Quesne, D., 2010. Segmentation and differential post-rift uplift at the Angola margin as recorded by the transform-rifted Benguela and oblique-to-orthogonal-rifted Kwanza basins. Marine and Petroleum Geology 27 (5), 1040–1068.

Guiraud, R., Bellion, Y., Benkhelil, J., Moreau, C., 1987. Post-Hercynian tectonics in Northern and Western Africa. Geological Journal 22, 443–466.

Gurnis, M., Mitrovica, J. X., Ritsema, J., Van Heijst, H. J., 2000. Constraining mantle density structure using geological evidence of surface uplift rates: The case of the African Superplume. Geochemistry, Geophysics, Geosystems.

Hack, J., 1957. Studies of longitudinal stream profiles in Virginia and Maryland. USGS Professional Paper 249.

Hafid, M., Salem, A. A., Bally, A. W., 2000. The western termination of the Jebilet-High Atlas system (Offshore Essaouira Basin, Morocco). Marine and Petroleum Geology 17 (3), 431–443.

Hall, J., Krasheninnikov, V., Hirsch, F., Benjamini, C., Flexer, A., Hall, J., 2005. Geological Framework of the Levant. Volume II: The Levantine ... II (April 2005), 836.

Hancock, G. R., Martinez, C., Evans, K. G., Moliere, D. R., 2006. A comparison of SRTM and high-resolution digital elevation models and their use in catchment geomorphology and hydrology: Australian examples. Earth Surface Processes and Landforms.

Haq, B. U., Hardenbol, J., Vail, P. R., 1987. Chronology opf fluctuating sea levels since the Triassic. Science 235 (4793), 1156–1167.

Hardy, S., Gawthorpe, R., 2002. Normal fault control on bedrock channel incision and sediment supply: Insights from numerical modeling. Journal of Geophysical Research: Solid Earth 107 (B10), EPM 9–1–EPM 9–15.

Harris, P., 1972. Geothermal environment and basalt magma type. Journal of Earth Science 8, 275–281.

Hartley, R., Allen, P., 1994. Interior cratonic basins of Africa: Relation to continental breakup and role of mantle convection. Basin Research 6 (2-3), 95–113.

Hay, W. W., 1998. Detrital sediment fluxes from continents to oceans. Chemical Geology 145 (3-4), 287–323.

Hay, W. W., Soeding, E., DeConto, R. M., Wold, C. N., 2002. The late cenozoic uplift - Climate change paradox. International Journal of Earth Sciences 91 (5), 746–774.

Hearty, P., 1986. An inventory of last interglazial (sensu lato) age deposits from the Mediterranean basin: a study of isoleucine epimerisation and U-Series dating. Zeitschrift fur Geomorphologie (62), 51–69.

Hefferan, K. P., Admou, H., Karson, J. A., Saquaque, A., 2000. Anti-Atlas (Morocco) role in Neoproterozoic Western Gondwana reconstruction. Precambrian Research 103 (1-2), 89–96.

Hendey, Q., 1978. Preliminary report on the Miocene vertebrates from Arrisdrift, South West Africa. Ann S. Afr. Mus. (76), 1–41.

Herzberg, C., Raterron, P., Zhang, J., 2000. New experimental observations on the anhydrous solidus for peridotique KLB-1. Geochemistry Geophysics Geosystems 1.

Hoggard, M. J., Winterbourne, J., Czarnota, K., White, N., 2017. Oceanic residual depth measurements, the plate cooling model, and global dynamic topography. Journal of Geophysical Research: Solid Earth.

Holeman, J. N., 1968. The Sediment Yield of Major Rivers of the World. Water Resour. Res. 4 (4), 737–747.

Holm, P. M., Grandvuinet, T., Friis, J., Wilson, J. R., Barker, A. K., Plesner, S., 2008. An 40Ar-39Ar study of the Cape Verde hot spot: Temporal evolution in a semistationary plate environment. Journal of Geophysical Research: Solid Earth 113 (8).

Holmes, A., 1944. Principles of Physical Geology. London and Edinburgh.

Holmes, A., 1965. The Principles pf Physical Geology. Nelson, Edinburgh.

Hori, N., 1970. Raised coral reefs along the southeastern coast of Kenya, East Africa.

Hovius, N., 1998. Controls on sediment supply by large rivers. In: Shanley, K., McCabe, P. (Eds.), Relative role of Eustasy, Climate and Tectonism in Continental Rocks, sepm spec. Edition. pp. 3–16.

Howard, A., 1971. Problems in interpretation of simulation models of geologic processes. In: M. Morisawa, P. (Ed.), Quantitative Geomorphology: Some Aspects and Applications. Publ. in Geomorphology, Binghamton, N.Y., pp. 61–82.

Howard, A. D., 1987. Modelling Fluvial Systems: Rock-, Gravel-, and Sand-bed Channels. In: River Channels: Environment and Process.

Howard, A. D., 1988. Equilibrium models in geomorphology. In: Anderson, M. (Ed.), Modelling Geomorphological Systems. No. 3. John Wiley & Sons Ltd., pp. 49–70.

Howard, A. D., Dietrich, W. E., Seidl, M. A., 1994. Modeling fluvial erosion on regional to continental scale. Journal of Geophysical Research 99.

Howard, A. D., Hemberger, A. T., 1991. Multivariate characterization of meandering. Geomorphology.

Howard, A. D., Kerby, G., 1983. Channel changes in badlands. Geological Society of America Bulletin.

Hwang, Y. K., Ritsema, J., Goes, S., 2009. Spatial variations of P wave attenuation in the mantle beneath North America. Journal of Geophysical Research: Solid Earth 114 (6), 1–11.

Ierodiaconou, D., Schimel, A. C., Kennedy, D., Monk, J., Gaylard, G., Young, M., Diesing, M., Rattray, A., 2018. Combining pixel and object based image analysis of ultra-high resolution multibeam bathymetry and backscatter for

habitat mapping in shallow marine waters. Marine Geophysical Research 39 (1-2), 271–288.

Immenhauser, A., 2009. Estimating palaeo-water depth from the physical rock record. Earth-Science Reviews 96 (1-2), 107–139.

Ismail, A. A., Boukhary, M., Naby, A. I. A., 2010. Subsurface stratigraphy & micropaleontology of the Neogene rocks, Nile Delta, Egypt. Geologia Croatica 63 (1), 1–26.

Janssen, M. E., Stephenson, R. A., Cloetingh, S., 1995. Temporal and spatial correlations between changes in plate motions and the evolution of rifted basins in Africa. Geological Society of America Bulletin.

Jardiné, S., Magloire, L., 1965. Palynologie et stratigraphie du Crétacé des basins du Sénégal et de Côte d'Ivoire. Mémoire du Bureau Rechereche Géologiques Minières.

Jedoui, Y., Reyss, J.-L., Kallel, N., Montacer, M., Ismail, H. B., Davaude, E., 2003. U-series evidence for two high Last Interglacial sea levels in southeastern Tunisia. Quaternary Science Reviews 22, 343–351.

Jones, S. M., Lovell, B., Crosby, A. G., 2012. Comparison of modern and geological observations of dynamic support from mantle convection. Journal of the Geological Society.

Kaufman, A., Broecker, W. S., Ku, T. L., Thurber, D. L., 1971. The status of U-series methods of mollusk dating. Geochimica et Cosmochimica Acta 35 (11), 1155–1183.

Kennett, J., Srinivasan, M., 1983. Neogene planktonic foraminifera. Hutchinson Ross Publ. Go., Stroudsburg, Pennsylvania.

Kensley, B., 1985. The faunal deposits of a raised beach at Milnerton, Cape Province, South Africa. Annals of the South African Museum 95, 111–122.

Kensley, B., Pether, J., 1985. Late Tertiary and Quaternary fossil Mollusca of the Hondeklip area, Cape Province, South Africa. Annals of the South African Museum 97, 141–225.

King, S. D., Ritsema, J., 2000. African hot spot volcanism: Small-scale convection in the upper mantle beneath cratons. Science 290 (5494), 1137–1140.

Klitgord, K., Schouten, H., 1986. Plate kinematics of the Central Atlantic. In: Vogt, P., Tucholke, B. (Eds.), The Geology of North America, the Western Atlantic region: Decade of North American Geology, dnag serie Edition. Geological Society of America.

Ku, T. L., 1966. Uranium series disiquilibrium in deep-sea sediments, Ph. D. thesis.

Lague, D., 2014. The stream power river incision model: Evidence, theory and beyond. Earth Surface Processes and Landforms.

Lally, A., 1992. Chemical procedures. In: Ivanovich, M., Harmon, R.S. (Eds.). Uranium-Series Disequilibrium: Applications to Earth, Marine and Environmental Sciences.

Lambeck, K., Yokoyama, Y., Purcell, T., 2002. Into and out of the last glacial maximum: Sea-level change during oxygen isotope stages 3 and 2. Quaternary Science Reviews 21 (1-3), 343–360.

Langford, R., Wilford, G., Truswell, E., Isern, A., 1995. Palaeogeographic Atlas of Australia-Cainozoic, Cretaceous. Aust. Geolog. Sur. Organ. Canberra, Aust. 10.

Laubscher, H., Bernoulli, D., 1977. Mediterranean and Tethys. In: Nairn A.E.M., Kanes W.H., Stehli F.G. (eds) The Ocean Basins and Margins, plenum pre Edition. Springer, New York, pp. 1–28.

Leckie, R., Farnham, C., Schmidt, M., 1993. Oligocene Planktonic Foraminifer Biostratigraphy of Hole 803D (Ontong Java Plateau) and Hole 628A (Little Bahama Bank), and Comparison with the Southern High Latitudes. Proceedings of the Ocean Drilling Program, 130 Scientific Results 130, 113–136.

Leeder, M. R., 1993. Tectonic controls upon drainage basin development, river channel migration and alluvial architecture: implications for hydrocarbon

reservoir development and characterization. Geological Society, London, Special Publications 73 (1), 7–22.

Lekie, R. M., Olson, H. C., 2003. Foraminifera As Proxies for Sea-Level Change on Siliciclastic Margins. Micropaleontologic Proxies for Sea-Level Change and Stratigraphic Discontinuities (75), 5–19.

Levander, A., Humphreys, G., Ryan, P., 2009. Program to Investigate Convective Alb-oran Sea System Overturn. nternational Federation of Digital Seismograph Net-works. Other/Seismic Network.

Lighthill, M. J., Whitham, G. B., 1955. On Kinematic Waves. I. Flood Movement in Long Rivers. Proceedings of the Royal Society A: Mathematical, Physical and Engineering Sciences 229 (1178), 281–316.

Lithgow-Bertelloni, C., Silver, P. G., 1998. Dynamic topography, plate driving forces and the African superswell. Nature 395 (6699), 269–272.

Lodge, A., Helffrich, G., 2006. Depleted swell root beneath the Cape Verde Islands. Geology 34 (6), 449–452.

Lodhia, B., Roberts, G., Fraser, A., Fishwick, S., Goes, S., Jarvis, J., 2018. Continental margin subsidence from shallow mantle convection: Example from West Africa. Earth and Planetary Science Letters 481, 350–361.

Luke, J. C., 1972. Mathematical models for landform evolution. Journal of Geophysical Research 77 (14), 2460–2464.

Macgregor, D., 2012. The development of the Nile drainage system: integration of onshore and offshore evidence. Petroleum Geoscience 18 (1981), 417–431.

Madeira, J., Mata, J., Mourão, C., Brum da Silveira, A., Martins, S., Ramalho, R., Hoffmann, D. L., 2010. Volcano-stratigraphic and structural evolution of Brava Island (Cape Verde) based on40Ar/39Ar, U-Th and field constraints. Journal of Volcanology and Geothermal Research 196 (3-4), 219–235.

Mauz, B., Elmejdoub, N., Nathan, R., Jedoui, Y., 2009. Late Pleistocene littoral deposits of Tunisia: new age data derived from optical dating. Paleogeography, Paleoclimatology, Paleoecology.

McCarthy, C., Takei, Y., Hiraga, T., 2011. Experimental study of attenuation and dispersion over a broad frequency range: 2. the universal scaling of polycrystalline materials. Journal of Geophysical Research: Solid Earth 116 (9), 1–18.

McKenzie, D., Fairhead, D., 1997. Estimates of the effective elastic thickness of the continental lithosphere from Bouguer and free air gravity anomalies. Journal of Geophysical Research: Solid Earth 102 (B12), 27523–27552.

McKenzie, D., Roberts, J., Weiss, N., 1974. Convection in the mantle: towards a numerical simulation. J. Fluid Mech. 62 (1974), 465–538.

Meghraoui, M., Outtani, F., Choukri, A., De Lamotte, D. F., 1998. Coastal Tectonics across the South Atlas Thrust Front and the Agadir Active Zone, Morocco. Geological Society London Special Publications 146 (1), 239–253.

Merritts, D., Bull, W. B., 1989. Interpreting Quaternary uplift rates at the Mendocino triple junction, northern California, from uplifted marine terraces. Geology 17 (11), 1020–1024.

Miller, K. G., Kominz, M. A., Browning, J. V., Wright, J. D., Mountain, G. S., Katz, M. E., Sugarman, P. J., Cramer, B. S., Christie-Blick, N., Pekar, S. F., 2005. The phanerozoic record of global sea-level change. Science 310 (5752), 1293–1298.

Milliman, J., Farnsworth, K., 2011. River discharge to the coastal ocean: a global synthesis. Cambridge University Press.

Milliman, J., Farnsworth, K., 2013. River discharge to the coastal ocean: a global synthesis. Cambridge University Press.

Milliman, J., Syvitski, J., 1992. Geomorphic/tectonic control of sediment discharge to the ocean: the importance of small mountainous rivers. The Journal of Geology 100 (5), 525–544.

Mitchell, J. G., Le Bas, M. J., Zielonka, J., Furnes, H., 1983. On dating the magmatism of Maio, Cape Verde Islands. Earth and Planetary Science Letters 64 (1), 61–76.

Monechi, S., Reale, V., Bernaola, G., Balestra, B., 2013. The Danian/Selandian boundary at Site 1262 (South Atlantic) and in the Tethyan region: Biomagnetostratigraphy, evolutionary trends in fasciculiths and environmental effects of the Latest Danian Event. Marine Micropaleontology 98, 28–40.

Moucha, R., Forte, A. M., 2011. Changes in African topography driven by mantle convection. Nature Geoscience 4 (10), 707–712.

Moucha, R., Forte, A. M., Mitrovica, J. X., Rowley, D. B., Quéré, S., Simmons, N. A., Grand, S. P., 2008. Dynamic topography and long-term sea-level variations: There is no such thing as a stable continental platform. Earth and Planetary Science Letters 271 (1-4), 101–108.

Mudd, S. M., Attal, M., Milodowski, D. T., Grieve, S. W., Valters, D. A., 2014. A statistical framework to quantify spatial variation in channel gradients using the integral method of channel profile analysis. Journal of Geophysical Research: Earth Surface.

Müller, R. D., Hassan, R., Gurnis, M., Flament, N., Williams, S. E., 2017. Dynamic topography of passive continental margins and their hinterlands since the Cretaceous. Gondwana Research 53, 225–251.

Nyagah, K., 1995. Stratigraphy, depositional history and environments of deposition of Cretaceous through Tertiary strata in the Lamu Basin, southeast Kenya and implications for reservoirs for hydrocarbon exploration. Sedimentary Geology 96 (1-2), 43–71.

Nyblade, A. A., Robinson, S. W., 1994. The African Superswell. Geophysical Research Letters 21 (9), 765–768.

Odada, E. O., 1996. Geological evolution of coastal Kenya as inferred from sedimentary sequences and marine terraces. Afr. Geosci. Rev. 3 (3), 1–18.

Olsson, R., Berggren, W., Hemleben, C., Huber, B., 1999. Atlas of Paleocene planktonic foraminifera.

Olsson, R., Pearson, P., Huber, B., 2006. Taxonomy, biostratigraphy, and phylogeny of Eocene Catapsydrax, Globorotaloides, Guembelitrioides, Paragloborotalia, Parasubbotina, and Pseudoglobigerinella n. gen. In: Pearson,

P. e. a. E. (Ed.), Atlas of Eocene Planktonic Foraminifera, cushman fo Edition. Allen Press, Lawrence, Kansas, pp. 67–110.

Parker, R. L., 1994. Geophysical Inverse Theory. Princeton Univ. Press, Princeton, N. J.

Partridge, T., Maud, R., 1987. Ceomorphic evolution of southern Africa since the Mesozoic. South African Journal of Geology 90 (2), 179–208.

Partridge, T. C., 1998. Of diamonds, dinosaura and diastrophism: 150 Million years of landscape evolution in southern Africa. South African Journal of Geology 101 (3), 167–184.

Partridge, T. C., Maud, R. R., 2000. Macro-scale geomorphic evolution of southern Africa, in The Cenozoic of Southern Africa. No. 40. Oxford University Press, New York.

Paul, J. D., Roberts, G. G., White, N., 2014. The African landscape through space and time. Tectonics 33 (6), 898–935.

Pechlivanidou, S., Cowie, P. A., Hannisdal, B., Whittaker, A. C., Gawthorpe, R. L., Pennos, C., Riiser, O. S., 2018. Source-to-sink analysis in an active extensional setting: Holocene erosion and deposition in the Sperchios rift, central Greece. Basin Research 30 (3), 522–543.

Pekeris, C., 1935. Thermal convection in the interior of the Earth. Geophysical Journal International 3 (8), 343–367.

Pelletier, J. D., 2007. Numerical modeling of the Cenozoic geomorphic evolution of the southern Sierra Nevada, California. Earth and Planetary Science Letters 259 (1-2), 85–96.

Perch-Nielsen, K., 1977. Albian to Pleistocene calcareous nannofossils from the Western South Atlantic, DSDP Leg 39. Initial Reports of the Deep Sea Drilling Project 39, 699–823.

Perch-Nielsen, K., Sadek, A., Barakat, M., Teleb, F., 1978. Late Cretaceous and Early Tertiary calcareous nannofossil and planktonic foraminifera zones

from Egypt. Actes du VIe Colloque Africain de Micropaléontologie, Tunis: Annales des Mines et de la géologie 28 (2), 337–403.

Pether, J., 1994. The sedimentology, palaeontology and stratigraphy of coastal-plain deposits at Hondeklip bay, Namaqualand, South Africa.

Pickford, M., 1998. Onland Tertiary marine strata in southwestern Africa: eustacy, local tectonics and epeirogenesis in a passive continental margin. South African Journal of Science 94, 5–8.

Pickford, M., Senut, B., Mein, P., Gommery, D., Morales, J., Soria, D., Nieto, M., Ward, J., 1996. Preliminary results of new excavations at Arrisdrift, middle Miocene of southern Namibia. Comptes rendus de l'Académie des sciences 322(11) (Série 2. Sciences de la terre et des planètes), 991–996.

Pickford, M., Senut, B., Mein, P., Morales, J., Solria, D., Nieto, M., Ward, J., Bamford, M., 1995. The discovery of lower and middle Miocene vertebrates at Auchas, southern Namibia.,. C.R. Acad. Sci. Paris (322), 901– 906.

Pim, J., Peirce, C., Watts, A. B., Grevemeyer, I., Krabbenhoeft, A., 2008. Crustal structure and origin of the Cape Verde Rise. Earth and Planetary Science Letters 272 (1-2), 422–428.

Plummer, H., 1931. Some Cretaceous foraminifera in Texas. Univ. Texas Bull. 3101, 109–203.

Posamentier, H. W., Allen, G. P., 1999. Siliciclastic Sequence Stratigraphy - Concepts and Applications. SEPM Concepts Sedimentol. Paleontol. Ser. 7, 210.

Priestley, K., McKenzie, D., 2006. The thermal structure of the lithosphere from shear wave velocities. Earth and Planetary Science Letters 244 (1-2), 285–301.

Priestley, K., McKenzie, D., 2013. The relationship between shear wave velocity, temperature, attenuation and viscosity in the shallow part of the mantle. Earth and Planetary Science Letters 381, 78–91.

Pritchard, D., Roberts, G. G., White, N. J., Richardson, C. N., 2009. Uplift histories from river profiles. Geophysical Research Letters 36 (24), 1–5.

Ramalho, R., Helffrich, G., Cosca, M., Vance, D., Hoffmann, D., Schmidt, D. N., 2010. Episodic swell growth inferred from variable uplift of the Cape Verde hotspot islands. Nature Geoscience 3 (11), 774–777.

Rattray, A., Ierodiaconou, D., Laurenson, L., Burq, S., Reston, M., 2009. Hydroacoustic remote sensing of benthic biological communities on the shallow South East Australian continental shelf. Estuarine, Coastal and Shelf Science 84 (2), 237–245.

Reijers, T. J. A., 2011. Stratigraphy and sedimentology of the Niger delta. Geologos 17 (3), 133–162.

Repka, J. L., Anderson, R. S., Finkel, R. C., 1997. Cosmogenic dating of fluvial terraces, Fremont River, Utah. Earth and Planetary Science Letters 152 (1-4), 59–73.

Richards, F. D., Hoggard, M. J., White, N., 2016. Cenozoic epeirogeny of the Indian peninsula. Geochem. Geophys. Geosyst 17, 4920– 4954.

Ritsema, J., Deuss, A., Van Heijst, H. J., Woodhouse, J. H., 2011. S40RTS: A degree-40 shear-velocity model for the mantle from new Rayleigh wave dispersion, teleseismic traveltime and normal-mode splitting function measurements. Geophysical Journal International 184 (3), 1223–1236.

Roberts, D. L., Brink, J. S., 2002. Dating and correlation of neogenecoastal deposits in the Western Cape (South Africa): implications for neotectonism. South African Journal of Geology 105 (October), 337–352.

Roberts, G., White, N., Lodhia, B., 2019. The Generation and scaling of fluvial landscapes. Geochem. Geophys. Geosyst 124, 1–17.

Roberts, G. G., Paul, J. D., White, N., Winterbourne, J., 2012a. Temporal and spatial evolution of dynamic support from river profiles: A framework for Madagascar. Geochemistry, Geophysics, Geosystems 13 (4), 1–23.

Roberts, G. G., White, N., 2010. Estimating uplift rate histories from river profiles using African examples. Journal of Geophysical Research: Solid Earth 115 (2).

Roberts, G. G., White, N. J., Martin-Brandis, G. L., Crosby, A. G., 2012b. An uplift history of the Colorado Plateau and its surroundings from inverse modeling of longitudinal river profiles. Tectonics 31 (4), 1–25.

Romans, B. W., Normark, W. R., McGann, M. M., Covault, J. A., Graham, S. A., 2009. Coarse-grained sediment delivery and distribution in the Holocene Santa Monica Basin, California: Implications for evaluating source-to-sink flux at millennial time scales. Bulletin of the Geological Society of America 121 (9-10), 1394–1408.

Romein, A., 1979. Lineages in early paleogene calcareous nannoplankton. Utrecht Micropaleontological Bulletins 22, 1–230.

Rosenbloom, N. A., Anderson, R. S., 1994. Hillslope and channel evolution in a marine terraced landscape , Santa Cruz , California. Journal of Geophysical Research 99 (B7), 14013–14029.

Rouby, D., Bonnet, S., Guillocheau, F., Gallagher, K., Robin, C., Biancotto, F., Dauteuil, O., Braun, J., 2009. Sediment supply to the Orange sedimentary system over the last 150 My: An evaluation from sedimentation/denudation balance. Marine and Petroleum Geology 26 (6), 782–794.

Royden, L., Clark, M., Whipple, K., 2000. Evolution of river elevation profiles by bedrock incision: Analytical solutions for transient river profiles related to changing uplift and precipitation rates. Eos Trans. AGU 81 (48).

Royden, L., Perron, J., 2013. Solutions of the stream power equation and application to the evolution of river longitudinal profiles. Journal of Geophysical Research: Earth Surface 118 (2), 497–518.

Rudge, J. F., Roberts, G. G., White, N. J., Richardson, C. N., 2015. Uplift histories of Africa and Australia from linear inverse modeling of drainage inventories. Journal of Geophysical Research F: Earth Surface 120 (5), 894–914.

Rudge, J. F., Shaw Champion, M. E., White, N., McKenzie, D., Lovell, B., 2008. A plume model of transient diachronous uplift at the Earth's surface. Earth and Planetary Science Letters 267 (1-2), 146–160.

Rust, D. J., Summerfield, M. A., 1990. Isopach and borehole data as indicators of rifted margin evolution in southwestern Africa. Marine and Petroleum Geology 7 (3), 277–287.

Sahagian, D., 1988. Epeirogenic motions of Africa as inferred from Cretaceous shoreline deposits. Tectonics 7 (1), 125–138.

Said, A., Moder, C., Clark, S., Ghorbal, B., 2015. Cretaceous-Cenozoic sedimentary budgets of the Southern Mozambique Basin: Implications for uplift history of the South African Plateau. Journal of African Earth Sciences 109, 1–10.

Salman, G., Abdula, I., 1995. Development of the Mozambique and Ruvuma sedimentary basins, offshore Mozambique. Sedimentary Geology 96 (1-2), 7–41.

Saquaque, A., Admou, H., Karson, J., Hefferan, K., Reuber, I., 1989. Precambrian accretionary tectonics in the Bou Azzer-El Graara region, Anti-Atlas, Morocco. Geology 17, 1107–1110.

Savostin, L., Sibuet, J.-C., Zonenshain, L., Le Pichon, X., Roulet, M.-J., 1986. Kinematic Evolution of the Thethys Belt from the Atlantic Ocean to the Pamirs Since the Triassic. Tectonophysics 123, 1–35.

Schaeffer, A. J., Lebedev, S., 2013. Global shear speed structure of the upper mantle and transition zone. Geophysical Journal International 194 (1), 417–449.

Schock, S. G., 2004. A method for estimating the physical and acoustic properties of the sea bed using chirp sonar data. IEEE Journal of Oceanic Engineering 29 (4), 1200–1217.

Sclater, J. G., Christie, P. A. F., 1980. Continental Stretching: An Explanation of the Post-Mid-Creatceous Subsidence of the Central North Sea Basin. J. Geophys. Res. 85 (87), 3711–3739.

Seidl, M., Dietrich, W., 1992. The problem of channel erosion into bedrock. Catena Suppl. 23, 101–124.

Senut, B., Pickford, M., 1995. Fossil eggs and Cenozoic continental biostratigraphy of Namibia. Palaeontologia Africaner 32, 33–37.

Séranne, M., Nzé Abeigne, C. R., 1999. Oligocene to Holocene sediment drifts and bottom currents on the slope of Gabon continental margin (west Africa) consequences for sedimentation and southeast Atlantic upwelling. Sedimentary Geology 128 (3-4), 179–199.

Sestini, G., 1989. Nile Delta: a review of depositional environments and geological history. Geological Society, London, Special Publications 41 (1), 99–127.

Shahnas, M. H., Pysklywec, R. N., 2004. Anomalous topography in the western Atlantic caused by edge-driven convection. Geophysical Research Letters 31 (18), 2–6.

Sigal, J., 1948. Notes sur les genres de foraminiferes Rotalipora Brotzen, 1942 et Thalmanninella (Famille des Globorotaliidae). Revue de l'Institut Francais du Petrole et Annales des Combustible Liquides 3 (4), 95–103.

Simpson, G., Schlunegger, F., 2003. Topographic evolution and morphology of surfaces evolving in response to coupled fluvial and hillslope sediment transport. Journal of Geophysical Research: Solid Earth 108 (B6), 1–16.

Sklar, L., Dietrich, W. E., 1998. River longitudinal profiles and bedrock incision models: Stream power and the influence of sediment supply. In: Geophysical Monograph Series.

Sklar, L. S., Dietrich, W. E., 2001. Sediment and rock strength control on river incision into bedrock. Geology 29 (12), 1087–1090.

Smith, T., Bretherton, F., 1972. Stability and the Conservation Mass in Drainage Basin Evolution. Water Resources Research 8 (6), 1506–1529.

Smith, T. R., Merchant, G. E., Birnir, B., 2000. Transient attractors: Towards a theory of the graded stream for alluvial and bedrock channels. Computers and Geosciences 26 (5), 541–580.

Smith, W. H. F., Wessel, P., 1990. Gridding with continuous curvature splines in tension. Geophysics 55 (3), 293–305.

Somme, T. O., Piper, D. J. W., Deptuck, M. E., Helland-Hansen, W., 2011. Linking Onshore-Offshore Sediment Dispersal in the Golo Source-to-Sink System (Corsica, France) During the Late Quaternary. Journal of Sedimentary Research 81 (2), 118–137.

Spies, J., L.N.J, E., Malherbe, S., Viljoen, J., 1963. Die geologie van die gebied tussen Bredasdorp en Gansbaai., expln. she Edition. Geol. Surv. S. Afr.,.

Stearns, C. E., Thurber, D. L., 1965. Th230/U234 dates of late Pleistocene marine fossils from the Mediterranean and Moroccan littorals. Progress in Oceanography 4 (C), 293–305.

Stephenson, S., Roberts, G., Hoggard, M., Whittaker, A., 2014. From Longitudinal River Profiles. Geochemistry, Geophysics, Geosystems 15, 4734–4758.

Stern, R. J., 1994. ARC Assembly and Continental Collision in the Neoproterozoic East African Orogen: Implications for the Consolidation of Gondwanaland. Annual Review of Earth and Planetary Sciences 22 (1), 319–351.

Stevenson, I. R., Mccann, C., Runciman, P. B., Town, C., 2002. An attenuation-based sediment classification technique using Chirp sub-bottom profiler data and laboratory acoustic analysis. Marine Geophysical Researches 23, 277–298.

Stucky de Quay, G., Roberts, G., Watson, J., Jackson, C. A.-L., 2017. Incipient mantle plume evolution: Constraints from ancient landscapes buried beneath the North Sea. Geochem. Geophys. Geosyst. 18 (9), 73–993.

Stucky de Quay, G., Roberts, G. G., Rood, D. H., Fernandes, V. M., 2019. Holocene uplift and rapid fluvial erosion of Iceland: A record of post-glacial landscape evolution. Earth and Planetary Science Letters 505, 118–130.

Sykes, L. R., 1978. Intraplate seismicity, reactivation of preexisting zones of weakness, alkaline magmatism, and other tectonism postdating continental fragmentation. Reviews of Geophysics 16 (4), 621–688.

Syvitski, J. P., Peckham, S. D., Hilberman, R., Mulder, T., 2003. Predicting the terrestrial flux of sediment to the global ocean: A planetary perspective. Sedimentary Geology 162 (1-2), 5–24.

Tait, J., Schätz, M., Bachtadse, V., Soffel, H., 2000. Palaeomagnetism and Palaeozoic palaeogeography of Gondwana and European terranes. Geological Society, London, Special Publications 179 (1), 21–34.

Takei, Y., Karasawa, F., Yamauchi, H., 2014. Temperature, grain size, and chemical controls on polycrystal anelasticity over a broad frequency range extending into the seismic range. Journal of Geophysical Research: Solid Earth 119 (7), 5414–5443.

Tapley, B., Ries, J., Bettadpur, S., Chambers, D., Cheng, M., Condi, F., Gunter, B., Kang, Z., Nagel, P., Pastor, R., Pekker, T., Poole, S., Wang, F., 2005. GGM02 - An improved Earth gravity field model from GRACE. Journal of Geodesy 79 (8), 467–478.

Teisserenc, P., Villemin, J., 1989. Sedimentary Basin of Gabon–Geology and Oil Systems. Divergent/Passive Margin Basins 48, 117–199.

Thomas, C., 2010. Morocco-Muenster. International Federation of Digital Seismo-graph Networks. Other/Seismic Network.

Thomas, R. J., Fekkak, A., Ennih, N., Errami, E., Loughlin, S. C., Gresse, P. G., Chevallier, L. P., Liégeois, J. P., 2004. A new lithostratigraphic framework for the Anti-Atlas Orogen, Morocco. Journal of African Earth Sciences 39 (3-5), 217–226.

Tinker, J., de Wit, M., Brown, R., 2008. Mesozoic exhumation of the southern Cape, South Africa, quantified using apatite fission track thermochronology. Tectonophysics 455 (1-4), 77–93.

Tomkin, J. H., Brandon, M. T., Pazzaglia, F. J., Barbour, J. R., Willett, S. D., 2003. Quantitative testing of bedrock incision models for the Clearwater River, NW Washington State. Journal of Geophysical Research: Solid Earth 108 (B6).

Törnqvist, T. E., Wortman, S. R., Mateo, Z. R. P., Milne, G. A., Swenson, J. B., 2006. Did the last sea level lowstand always lead to cross-shelf valley formation and source-to-sink sediment flux? Journal of Geophysical Research: Earth Surface 111 (4), 1–13.

Turcotte, D., Schubert, G., 2002. Geodynamics. Cambridge University Press.

Uchupi, E., Emery, K., Bowin, C., Phillips, J., 1976. Continental margin off western Africa-Senegal to Portugal. American Association of Petroleum Geologists Bulletin 60 (5), 809–878.

Unrug, R., 1996. The assembly of Gondwanaland. Scientific results of IGCP Project 288: Gondwanaland sutures and mobile belts 9, 11–20.

Unrug, R., 1997. Rodinia to Gondwana: The geodynamic map of Gondwana supercontinent assembly. GSA Today 7 (1).

USGS, 2016. Shuttle Radar Topography Mission (SRTM) 1 Arc-Second Global.

van der Beek, P., Bishop, P., 2003. Cenozoic river profile development in the Upper Lachlan catchment (SE Australia) as a test of quantitative fluvial incision models. Journal of Geophysical Research: Solid Earth 108 (B6).

Van der voo, R., 1988. Paleozoic paleogeography of North America, Gondwana, and intervening displaced terranes: Comparisons of paleomagnetism with paleoclimatology and biogeographical patterns. Bulletin of the Geological Society of America 100 (3), 311–324.

Van der Wateren, F., Dunai, T. J., 2001. Late Neogene passive margin denudation historyâcosmogenic isotope measurements from the central Namib desert. Global and Planetary Change 30, 271–307.

Van Rompaey, A., Bazzoffi, P., Jones, R. J., Montanarella, L., 2005. Modeling sediment yields in Italian catchments. Geomorphology 65 (1-2), 157–169.

Varol, O., 1989. Palaeocene calcareous nannofossil biostratigraphy. In: Nannofossils and their applications. Ellis Horwood Ltd, Chichester, pp. 267–310.

Vear, A., 2005. Deep-water plays of the Mauritanian continental margin. Petroleum Geology, 1217–1232.

Villeneuve, M., 2005. Paleozoic basins in West Africa and the Mauritanide thrust belt. Journal of African Earth Sciences 43 (1-3), 166–195.

Vinnik, L., Silveira, G., Kiselev, S., Farra, V., Weber, M., Stutzmann, E., 2012. Cape Verde hotspot from the upper crust to the top of the lower mantle. Earth and Planetary Science Letters 319-320, 259–268.

Wade, B. S., Pearson, P. N., Berggren, W. A., Pälike, H., 2011. Review and revision of Cenozoic tropical planktonic foraminiferal biostratigraphy and calibration to the geomagnetic polarity and astronomical time scale. Earth-Science Reviews 104 (1-3), 111–142.

Walford, H. L., White, N. J., Sydow, J. C., 2005. Solid sediment load history of the Zambezi Delta. Earth and Planetary Science Letters 238 (1-2), 49–63.

Walker, K. R., Shanmugam, G., Ruppel, S. C., 1983. A model for carbonate to terrigenous clastic sequences. Geological Society of America Bulletin 94 (6), 700–712.

Wang, J., Stewart, R., 2015. Inferring marine sediment type using chirp sonar data: Atlantis field, Gulf of Mexico. SEG Technical Program Expanded Abstracts 2015, 2385–2390.

Watts, A. B., 1994. Crustal Structure, Gravity-Anomalies and Flexure of the Lithosphere in the Vicinity of the Canary-Islands. Geophysical Journal International 119 (2), 648–666.

Weissel, J. K., Seidl, M. A., 1998. Inland propagation of erosional escarpments and river profile evolution across the southeast Australian passive continental margin. In: Geophysical Monograph Series.

Westphal, M., Bazhenov, M., Lauer, J., Pechersky, D., Sibuet, J.-C., 1986. Paleomagnetic Implications on the Evolution of the Tethys Belt from the Atlantic Ocean to the Pamirs Since the Triassic. Tectonophysics 123, 37–82.

Whipple, K. X., 2002. Implications of sediment-flux-dependent river incision models for landscape evolution. Journal of Geophysical Research 107 (B2), 2039.

Whipple, K. X., Hancock, G. S., Anderson, R. S., 2000. River incision into bedrock: Mechanics and relative efficacy of plucking, abrasion, and cavitation. Bulletin of the Geological Society of America 112 (3), 490–503.

Whipple, K. X., Tucker, G. E., 1999. Dynamics of the stream-power river incision model: Implications for height limits of mountain ranges, landscape response timescales, and research needs. Journal of Geophysical Research: Solid Earth 104 (B8), 17661–17674.

Whittaker, A. C., Boulton, S. J., 2012. Tectonic and climatic controls on knickpoint retreat rates and landscape response times. Journal of Geophysical Research: Earth Surface 117 (2), 1–19.

Whittaker, A. C., Cowie, P. A., Attal, M., Tucker, G. E., Roberts, G. P., 2007. Bedrock channel adjustment to tectonic forcing: Implications for predicting river incision rates. Geology 35 (2), 103–106.

Whittaker, J. M., Goncharov, A., Williams, S. E., Müller, R. D., Leitchenkov, G., 2013. Global sediment thickness data set updated for the Australian-Antarctic Southern Ocean. Geochemistry, Geophysics, Geosystems 14 (8), 3297–3305.

Wilson, D. J., Peirce, C., Watts, A. B., Grevemeyer, I., 2013. Uplift at lithospheric swells-II: Is the Cape Verde mid-plate swell supported by a lithosphere of varying mechanical strength? Geophysical Journal International 193 (2), 798–819.

Wyllie, M., Gregory, A., Gardner, L., 1956. Elastic wave velocities in heterogeneous and porous media. Geophysics 21 (1), 41–70.

Xu, W., Lithgow-Bertelloni, C., Stixrude, L., Ritsema, J., 2008. The effect of bulk composition and temperature on mantle seismic structure. Earth and Planetary Science Letters 275 (1-2), 70–79.

Ye, J., Chardon, D., Rouby, D., Guillocheau, F., Dall'asta, M., Ferry, J. N., Broucke, O., 2017. Paleogeographic and structural evolution of northwestern Africa and its Atlantic margins since the early Mesozoic. Geosphere 13 (4), 1254–1284.

Young, J., Bown, P., Lees, J., jul 2018. Guembelitria sp. http://www.mikrotax.org/pforams/index.php?taxon=Guembelitria sp.&module=pf_cenozoic.

Ziegler, P. A., 1988. Evolution of the ArcticNorth Atlantic and the western Tethys. American Association of Petroleum Geologists Memoir 43, 198.